Preliminary Performance Characteristics of a Microfabricated Turbopump

by

Shana Diez

Submitted to the Department of Aeronautics and Astronautics
in partial fulfillment of the requirements for the degree of

Master of Science in Aeronautics and Astronautics

at the

MASSACHUSETTS INSTITUTE OF TECHNOLOGY

September 2003

© Shana Diez, MMIII. All rights reserved.

The author hereby grants to MIT permission to reproduce and distribute publicly paper and electronic copies of this thesis document in whole or in part.

MASSACHUSETTS INSTITUTE OF TECHNOLOGY
NOV 0 5 2003
LIBRARIES

Author .....
Department of Aeronautics and Astronautics
September 2003

Certified by .....
Professor Alan H. Epstein
R.C. Maclaurin Professor of Aeronautics and Astronautics
Thesis Supervisor

Accepted by .....
Edward Greitzer
Chairman, Department Committee on Graduate Students

AERO

Preliminary Performance Characteristics of a Microfabricated Turbopump

by

Shana Diez

Submitted to the Department of Aeronautics and Astronautics
on September 2003, in partial fulfillment of the
requirements for the degree of
Master of Science in Aeronautics and Astronautics

Abstract

The demonstration micro turbopump was designed to prove the feasibility of pumping a liquid using a turbopump on the micro scale. This thesis presents the first data indicating positive pumping from the demonstration micro turbopump.

Data pertaining to both the turbomachinery as well as the bearing systems for these preliminary tests is shown and discussed. The pressure rise through the pump, turbine pressure ratio, respective powers, and a system efficiency are presented. Bearing theory and static flow test data are discussed.

The pump design is detailed. Modelling data is presented to help describe the operational difficulties with the highly coupled aft bearing system. These operational difficulties lead to the redesign of the aft bearing system, which is described in detail. Other operational procedures developed and discussed include the pump start up procedure and the use of the inverted journal bearing.

Thesis Supervisor: Professor Alan H. Epstein
Title: R.C. Maclaurin Professor of Aeronautics and Astronautics

Acknowledgments

The work presented in this thesis would not have been possible without the help and support of many people from the MIT community. First I would like to thank my advisor Professor Alan Epstein for giving me the chance to work on a project I have found challenging, exasperating, and altogether quite a lot of fun. I would also like to thank Professor Zoltan Spakovszky for his guidance and insight into bearings systems.

Thanks to Dr. Stuart Jacobson, Dr. Fred Ehrich, Dr. Gerry Guenette, and Dr. Jack Kerrebrock for their help along the way. Thanks to Chiang-Juay Teo for countless hours in the GTL clean room trying to figure out why pumps wouldn't spin, Laurent Jamonet for giving me my first taste of micropump testing, and Dr. Nori Miki for his help both with fabrication as well as testing. My extreme respect to the micropump fabrication team: Dr. Nori Miki, Linhvu Ho, Gwen Donahue, and Dr. Li Wang; without you guys there would be no pumps. Thanks to Lixian Liu, whose bearing calculations helped to shed light onto the rotordynamics issues of the turbopump. Thanks to James Letendre, Jack Costa, and Viktor Dubrowski for their patience and expertise in working with the rig and packaging. Thanks also to the members of the micro rocket team: Chris Protz, Jin-wook Lee, Matthieu Bernier, and all the others who were here before my time. Huge thanks as well to Lori Martinez for basically holding the GTL together.

I would also like to acknowledge the friends I have made both inside the lab and out. To Nick, Chris P., Chris S., Mark, Dan, Jessica, and Ling, thanks for making the GTL such a great place to work. To the friends I've made in the department: Garrett, Mark, Alex, Todd, Mike, Nate, and the countless others who have shared in the experiences of undergraduate and graduate life with me, you have made the last 5 years amazing and I will always have fond memories of MIT because of you. Special thanks to Mark M. for always being available to listen to me rant about whatever was bothering me and to Garret for keeping me in good spirits. To the other people who support me here, Mark L., Lisa, Amanda, my roommates, and my family, where

would I be without you. Thank you and I wish you the best with all your future endeavors.

The microrocket project and all research presented here is sponsored by DARPA. Their support is gratefully acknowledged.

Contents

List of Figures

List of Tables

Chapter 1

Introduction

The MIT micro engine project was started by Epstein et al. in order to investigate the use of micromachining techniques to create a micro-scale gas turbine engine [4]. The project has since then grown to include projects such as a micro generator, micro bearing rig, and micro rocket engine. The micro turbopump is one piece of the micro rocket engine system.

1.1 Background

Scaling laws indicate that simply decreasing the size of a rocket engine can have significant effects on performance. As the size of the engine decreases, its weight will decrease as a function of its volume (length cubed) while its thrust will decrease as a function of the throat area (length squared). This factor allows for substantial increases in thrust to weight characteristics of rocket engines on a small scale.

Micromachining techniques can decrease the cost per unit thrust of a rocket. Current rocket engines are still, to a large extent, built and assembled by hand. Since so few are made per year, the cost per engine is large. Using well established process controls for microfabrication, it is conceivable that high quality engines could be produced in bulk at much lower cost per unit thrust.

In order for these tiny engines to replace their large-scale counterparts, they would need to be placed in a cluster. This configuration may be advantageous for many

reasons. One is the increased reliability. If one engine in a grid of 200 engines stops working, the remainder could be redirected to account for this, reducing the risk of system failure. It also allows a customer to purchase thrust or power in more precise amounts. In many cases one is forced to purchase more thrust or more generator power than is necessary due to product availability. With the micro engine systems the customer could specify a need and have that exact need met by adjusting the number of engines purchased. A final advantage is that of repair and turnaround time. If a micromachined engine were to stop working, it could be replaced quickly and with minimal impact on the system, decreasing costly system repair time.

Engines on this scale could also open up new markets and make new technologies possible, both as micro power plants as well as for micro air vehicles and small scale satellites.

1.2 The Micro Rocket Engine

The micro rocket project is engaged in the development of a micro scale bipropellant rocket engine to produce 15 Newtons of thrust [14]. This system consists of a thrust chamber, two turbopumps, and micro valves. The micro rocket engine runs on an expander cycle as shown in figure 1-1. The propellants are JP7 and Hydrogen peroxide. JP7 is a fuel designed to have very little coking. With the small channels in the micro rocket engine, coking is a critical issue. Hydrogen peroxide is a storable oxidizer that is readily available, making it an attractive choice for the micro rocket engine.

1.2.1 Thrust Chamber

The thrust chamber consists of an injection plate, a combustion chamber, and a regeneratively cooled converging-diverging nozzle. Figure 1-2 is a picture of a gaseous thrust chamber. The thrust chamber is designed to produce 15 Newtons of thrust, with a massflow of 5 g/s and a specific impulse of 300s. Past work on the thrust chamber has investigated the system feasibility using gaseous propellants. This work

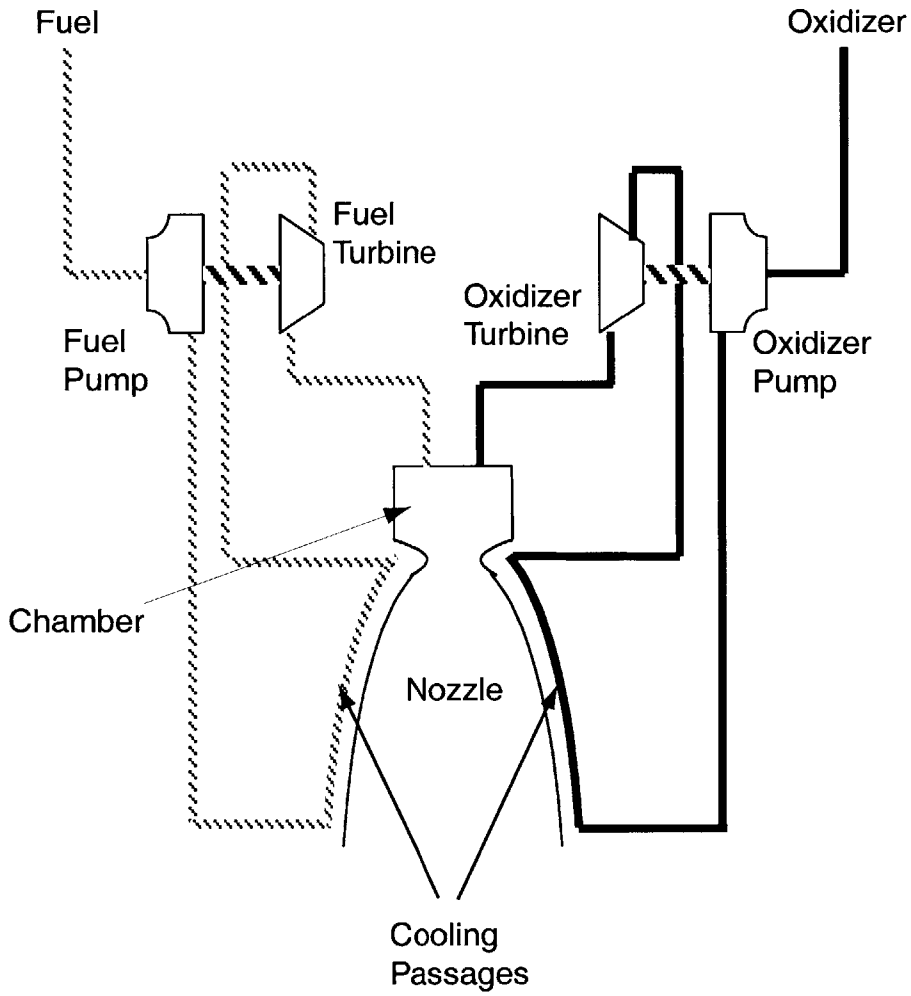

Figure 1-1: The expander cycle.

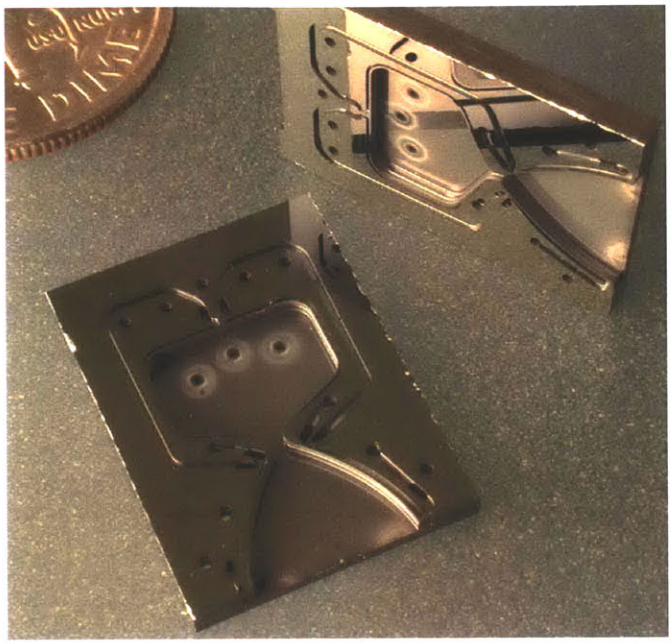

Figure 1-2: A micro rocket engine thrust chamber [7].

as well as liquid propellant tests are being conducted by Protz [14]. The original design and preliminary work on the microrocket thrust chamber was done by London [?].

1.2.2 Valves

There are currently two valves in development as part of the micro rocket engine, a servo valve and a pilot valve. Each valve set (one servo valve and one pilot valve) is designed for a massflow of 0.5 g/s. In order to meet the 5 g/s requirement of the rocket, 10 micro valve sets will be used in parallel. They will control the starting and stopping of the engine as well as throttling. Currently, manufacturing and testing of the valves is being conducted by Lee [9].

1.2.3 Turbopumps

The system requires two turbopumps, one for the hydrogen peroxide and one for the JP7. These are driven by turbines which run on the supercritical fluid flows from

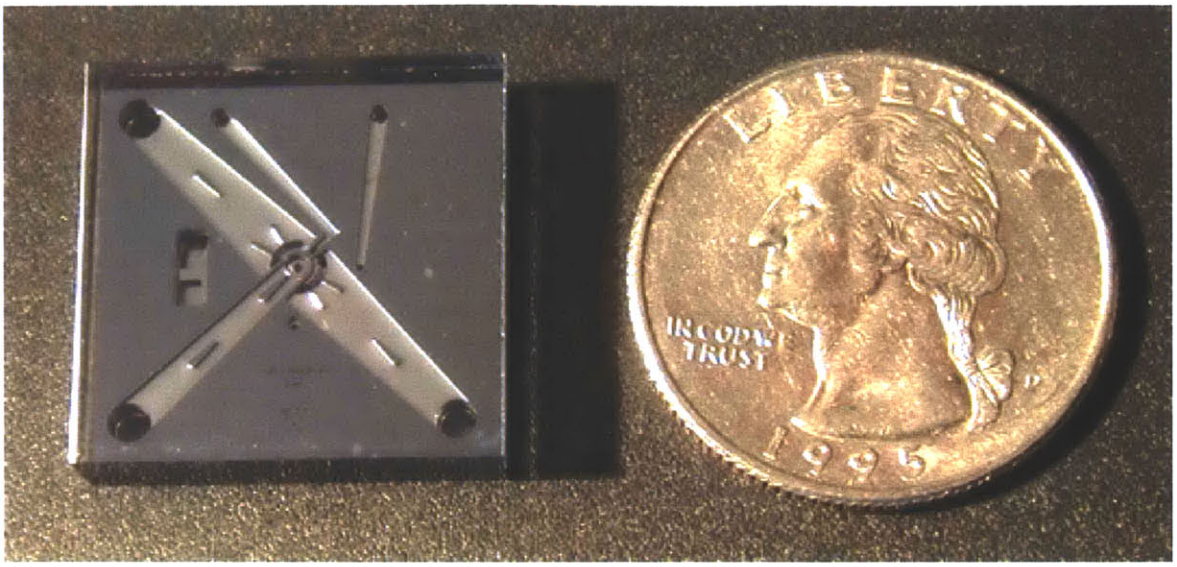

Figure 1-3: A demonstration micro turbopump.

the exit of the thrust chamber cooling channels. The high pressure propellants are injected directly into the combustion chamber. The current rocket design requires a pressure of 300 atm at the exit of the pump.

In order to prove that a microfabricated turbopump is feasible, a demonstration pump is currently being tested and developed. Figure 1-3 is a picture of a demonstration turbopump. This turbopump, detailed in Chapter 2, and its preliminary testing is the main topic of this thesis.

1.3 Previous Work on the Demonstration Microturbopump

As mentioned above, the demonstration pump is a proof of concept design. As such, its design pressure rise is less than that of the main pump. The micro turbopump is the first MIT micro engine to require a two phase operation (running both a liquid and a supercritical fluid in the same device).

Preliminary work done by Pennathur investigated cavitation in devices of this size [13]. Her work suggests that cavitation will not occur, but in the event that cavitation

becomes a problem, the demonstration pump could be used as a boost pump in the micro rocket engine system.

The first design of the demonstration turbopump was detailed by Deux [2]. This work discusses the first design and the analysis that went into this design. Further work in the fabrication and test set up was done by Jamonet [7]. The first spin tests of the pump were conducted by Jamonet, along with some design iterations and an in-depth analysis of the pump performance. There is also ongoing work done on micro scale gas bearings which has been used as a reference for the micro pump design as well as in understanding the operation of the pump.

1.4 Methodology

This chapter introduced the microrocket and demonstration micro turbopump. Chapter 2 discusses the pump design and the analysis that went into the recent redesign efforts. Chapter 3 gives the details of the test rig and discusses the procedures that were developed to operate the pump. Chapter 4 discusses the static testing and modelling which has been done to characterize and study the bearing systems implemented in the demonstration micro turbopump. Chapter 5 is an overview of the data collected on the pump and turbine as well as the corresponding efficiencies of the turbine, pump, and system. The final chapter will give suggestions as to the future work that should be done on the demonstration turbopump.

Chapter 2

The Demonstration Micro Turbopump

The demonstration micro turbopump has undergone substantial revisions since the beginning of the project. This chapter will review the general design of the pump and give the details of the current redesign efforts.

2.1 Pump Requirements

The demonstration micro turbopump took its requirements from the micro rocket thrust chamber. In order to operate in the expander cycle, the pump must match the mass flow of the thrust chamber as well as provide adequate pressure rise. In the case that a booster pump proves to be a necessity in the system, the demonstration turbopump should be able to operate as such. In order to meet this requirement, a massflow of 2.5 g/s and pressure rise of 30 atm was adopted in the original pump design [2]. Water was chosen as the pumped fluid for safety reasons.

As detailed by Deux [2], these requirements along with other programmatic and manufacturing constraints and an assumed efficiency of 30% for both the pump and the turbine led to a single wafer rotor design. Figure 2-1 shows a cross section of the pump as it currently exists. It also illustrates the flow paths of the pump and turbine. Table 2.1 is a summary of the required pressure differentials, flow rates, rotor speed,

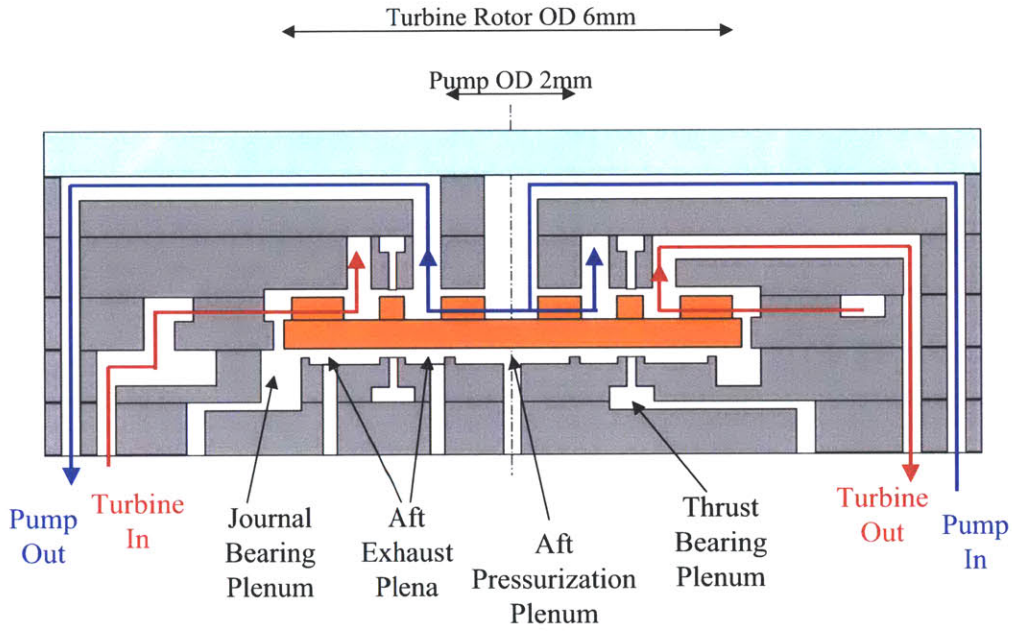

Figure 2-1: Demonstration micro turbopump cross section.

Table 2.1: Pump design data for 3 design points [2].

Rotor speed	750,000 RPM	190,000 RPM	50,000 RPM
Pump pressure rise for m =2.5g/s	30 atm	2 atm	0.137 atm
Pumping power required	36W	2.33W	0.16W
Turbine inlet pressure	24 atm	2.5 atm	1.15 atm
Turbine exit pressure	9 atm	1.5 atm	1 atm
Turbine mass flow rate	2.5 g/s	0.42 g/s	0.078 g/s
Turbine power delivered	50W	3.82W	0.24W
Pressure force on the forward side of the rotor	38N	5N	2.7N

and shaft powers which were originally suggested by Deux in order to achieve the 30 atm pressure rise through the pump [2].

Later work by Jamonet using a 3D CFD calculation suggests that due to fluid losses not originally taken into account, the maximum pressure rise the pump will achieve at the design point is 23 atm [7].

2.2 Design Overview

The general design of the demonstration turbopump takes advantage of a single-wafer rotor design to simplify the manufacturing process. Figure 2-2 is a view of the rotor from the top. This shows the liquid pump and nitrogen driven turbine, which are separated by an annulus that serves as a gas seal as well as a thrust bearing on the forward side. The bearings are nitrogen pressurized hydrostatic bearings. In addition to the forward thrust bearing, there is an aft thrust bearing, creating a bearing system to maintain axial stability. The journal bearing was designed to be operated by pressurizing a plenum on the aft side and allowing nitrogen to flow up through a small gap and then to mix with the turbine inlet flow. This journal bearing gap is labelled in Figure 2-2.

A lower plenum exists in order to provide external thrust balance. This plenum is externally pressurized to maintain a force balance on the two sides of the rotor. As detailed by Deux, with the single-wafer rotor, the pressure forces of the device are

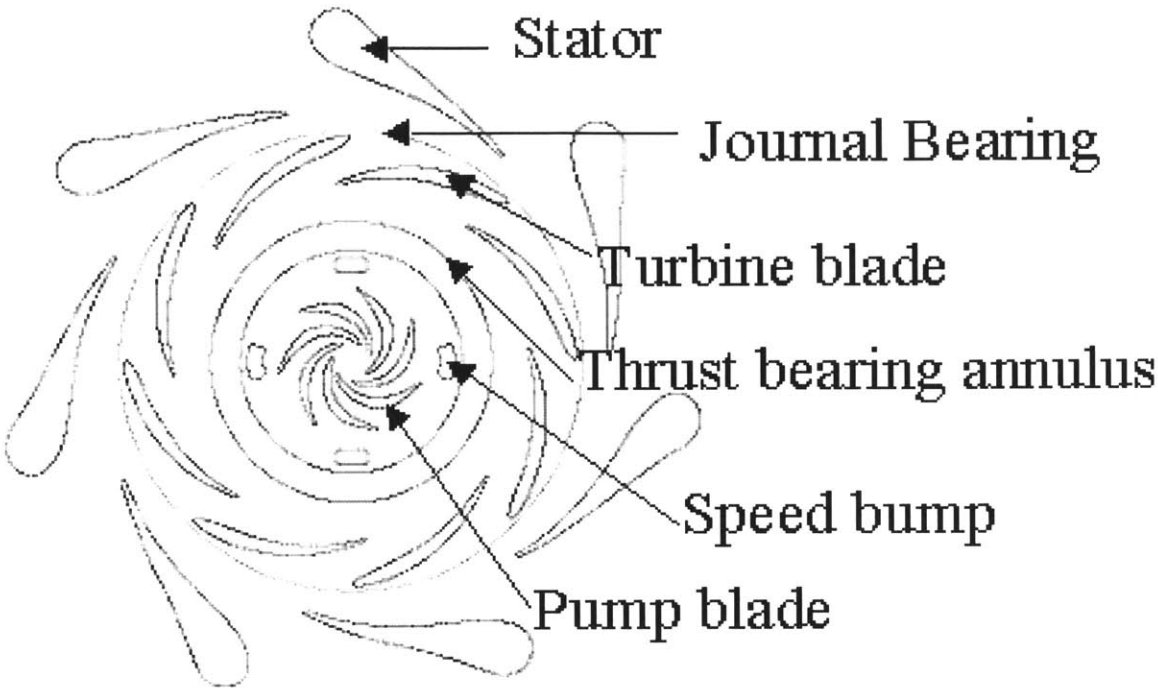

Figure 2-2: Rotor view from above.

concentrated on the forward face. Although the thrust bearings are designed to resist disturbances in axial location, they do not produce enough thrust to counteract the load on the top of the rotor [2].

A pyrex top layer is included in the pump design for a few reasons. As can be seen in Figure 2-2, the pump has 4 "speed bumps" etched into the rotor in the pump exhaust region. These are tracked in order to measure speed, as will be explained later, and a window needs to exist to give the instrumentation access to the speed bumps. It is also important to look for signs of possible cavitation in the pump, especially at high speeds. This window allows for visual inspection of the inlet and exit of the pump [13]. Besides the problems caused by cavitation, air bubbles in the pump can have rotordynamic implications. The large density difference between the gaseous nitrogen and the liquid water can cause a large imbalance, making visual inspection of the pump exit crucial.

There is another window revealing the stationary turbine vanes. This allows for

inspection of water leaks. If large amounts of water leak into the turbine, this can be seen through this window. Water leaks into the turbine can lead to water in the journal bearing, increasing the drag and dramatically changing the operating characteristics of the pump.

2.3 Fabrication Overview

The demonstration micro turbopump consists of five silicon layers which require 14 photomasks to create. Seven of these have been changed since Jamonet's work [7] and seven have not. The current photomasks can be found in Appendix A. The specific fabrication procedures were detailed by Jamonet [7]. Each layer is patterned separately. The layers are referred to by number, with 1 being the top, or forward most wafer and 5 being the bottom, or aft most wafer. When all layers are complete, layers 2 and 3 are bonded together, and the journal bearing is cut into layer 3 from the aft side. Oxide pads hold the rotor to the top of layer 2 allowing the journal bearing to be cut without causing the rotor to fall out. Once this is complete and the journal bearing is verified by inspection through four ports cut into the top of layer 2, the remainder of the silicon layers are bonded together.

At this point the wafers are cut into 5 separate devices or "dies," and are tested statically with the rotors bonded. This data is used to characterize the shape of the journal bearing, thrust bearings, and seals. Finally, the devices are cleaned and placed in HF acid to eat away the oxide holding the rotor in place. This releases the rotor. Once tested to verify that the rotor is free, the top pyrex layer is anodically bonded to the device and the devices are ready for pumping tests.

2.4 Previous Design Changes

Jamonet made several changes to the original design. The first changes involved decreasing the high viscous losses that were seen both experimentally as well as predicted by a model designed by Jamonet [7]. By increasing the cross sectional area of

the elbows of the large massflow passages, the losses were decreased by 50% in the turbine and 10% in the pump [7].

The second major redesign involved the structural design of the pump plena. Many of the larger plena in the pump were seen to exhibit structural failure at static pressures far below what was considered to be the limit. This was the result of overetching in the center of the plena. By adding features to decrease the local etch variation inside the plena, this problem has been corrected. These "posts" were placed inside the pump outlet and turbine inlet [7].

There have also been changes to further accommodate the fiberoptic speed measuring system. Once water was introduced into the pump, bubbles were seen inside the pump. The fiberoptic censor used to measure the speed is unable to distinguish between these bubbles and the speed bumps. These bubbles are believed to come from the forward thrust bearing and sealing system. Therefore, new viewing ports needed to be created to allow for alternate readings to be taken. Using the turbine blades, instead of the speed bumps, the fiberoptic sensor can take measurements from an area that is not in contact with water and thus does not have bubbles. There are four ports cut into layers 1 and 2 in order to allow for inspection of the journal bearing during fabrication. One of these was cut slightly larger to allow for reading the speed off of either the "speed bumps" or the turbine blades, depending on the operating requirements [7].

2.5 Current Pump Design

The current pump design, as shown in Figure 2-1, includes two exhaust ports on the aft side of the rotor as well as two new seals. One exhaust lies between the journal bearing plenum and the aft thrust bearing. Because it is on the periphery of the rotor, this will be referred to as the outer plenum and the seal separating this plenum from the journal bearing as the outer seal. The second exhaust lies between the aft thrust bearing and the lower plenum. Similarly, this will be referred to as the inner plenum and the seal separating the aft thrust bearing and the lower plenum will be

referred to as the inner seal. Both of the seals consist of multiple teeth, which are not shown in order to simplify this drawing.

2.5.1 Reasons for Aft Redesign

On the original design of the aft bearing system, there are three pressure inputs: the lower plenum, aft thrust bearing plenum, and the journal bearing plenum. The flow into all three of these plena must exit the device through the turbine outlet, thus through the journal bearing and rotating blades before exiting the device. This causes the three inlet flows to interact in ways that are difficult to predict. Coupled pressures and 3-D flow interactions make determining pressures at specific locations difficult. In addition to this, the aft side has a smaller running gap than the forward side allowing the entire aft side of the rotor to contribute to the stiffness of the system. These factors make the aft bearings difficult to model and difficult to understand. Chapter 4 will discuss the bearing performance in more detail.

The specific example of the inlet to the journal bearing is most important due to the fact that the pressure difference across the journal bearing determines the speeds at which the device experiences rotordynamic instabilities. Experimentally, it was seen that reversing the flow in the journal bearing was able to partially decouple the system, leading to more stable operation. By venting the journal bearing plenum to atmospheric pressure and controlling the leakage flow with a metering valve, the operator has a more accurate measure of the pressure difference across the bearing. This change also allows some of the flow injected into the aft system to exit through the journal bearing plenum, instead of through the bearing itself. This break in the coupling of the aft system has proven beneficial both in the modelling efforts of the aft system as well as the experimental performance. The success of the partial decoupling was a driver in the redesign of the aft bearing system discussed below.

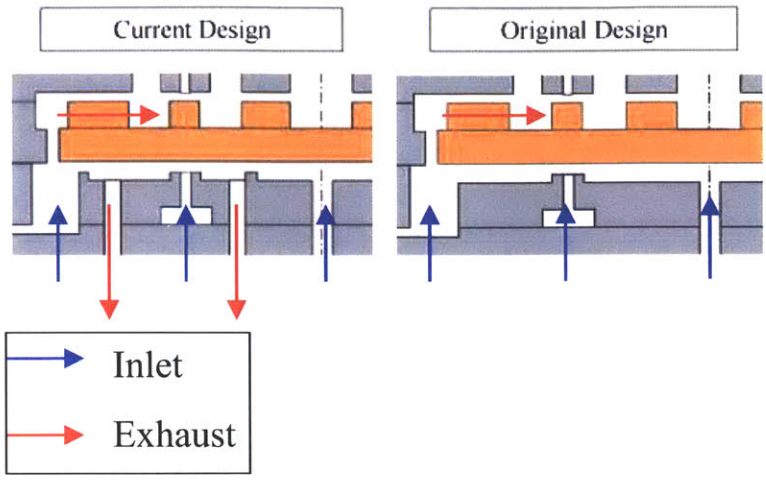

Figure 2-3: Comparison of original and current aft flow system.

2.5.2 Design Strategy

The original demonstration turbopump design contains three aft pressure inlets and no aft exhaust ports. This creates a coupled system, where it is difficult to measure the pressure at any given location. Because some of these pressures are critical to understanding the operating regime of the pump, it was determined that the addition of one or more aft exhaust ports would be beneficial to understanding the stability and operation of the system. Figure 2-3 compares the original aft flow system to the new design. In the original system the only exhaust for all three aft inlets is through the turbine blades, whereas in the current design there are two new aft exhaust ports. The exhaust ports will allow for more precise measurements in the bearing and pressurization plena. Since there will be less mixing of the flows on the aft side, the plena will isolate the bearings, making their pressures predictable at more locations.

The other major change is the utilization of an anisotropic journal bearing plenum. This design will be discussed in detail below. This change relaxes the strict fabrication tolerances imposed on the etching of the journal bearing by increasing the rotordynamic instability boundary of the journal bearing, which will be discussed in more detail in Chapter 4.

2.5.3 Analysis and Redesign

The main design challenge of the redesign of the aft side was the inclusion of two new seals. These seals are located at the edge of the journal bearing plenum and between the lower plenum entrance and the aft journal bearing land. They create the two aft exhaust ports discussed above. The parameters considered when designing the seals were the allowable leakage rates and the required pressure loss across the seal. A finite element analysis was then performed to ensure structural integrity. A CFD verification was also used.

Some restrictions were imposed on the aft redesign. First, in order to make the changes easy to implement, it was decided to change only layers 4 and 5. Therefore, the locations of all of the ports that connect to the forward side must not change. Also, the height of the seals was imposed to be the same as the height of the existing thrust bearing annulus. This allows for the new design to be created with the existing fabrication process. It avoids the need for another shallow etch on the aft side.

Preliminary Flow Loss Analysis

The first step in the seal design process was to do a preliminary analysis of the loss leakage through various seals. This model is a simple, incompressible model. It assumes Poiseuille channel flow across the length of the seal as well as an entrance loss into the seal. The Poiseuille loss can be defined as:

$$Q = \frac{-h^3}{12\mu}\frac{\Delta P}{\ell} \tag{2.1}$$

Where Q is the volumetric flow rate, h is the flow height, μ is the viscosity, ℓ is the land length and ΔP is the pressure change. The equation for the entrance loss is:

$$\Delta P = \frac{\gamma}{2}\rho V_{ent}^2 \tag{2.2}$$

Where Δ P is the change in pressure, γ is chosen to be 0.5, ρ is the density of the nitrogen flow, and V_{ent} is the velocity at the entrance to the seal. Figure 2-4 is the

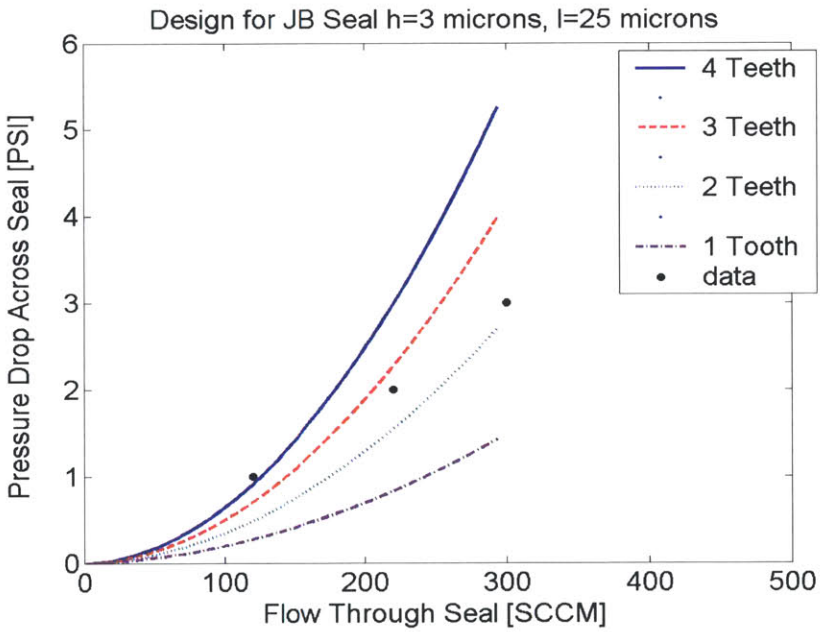

Figure 2-4: Results of simple seal design model.

result of this analysis performed on the outer seal geometry. Since the reading at the entrance to the journal bearing is critical, for rotordynamic reasons, the leakage at this seal is also critical. The four lines show varying numbers of teeth in the seals, assuming an entrance loss for each tooth. The data shown assumes a 20% leak path through the seal. This data was taken from experimental testing of the journal bearings of existing micro turbopumps. According to this approximation, a seal with four teeth should be adequate to seal the journal bearing plenum to 20%.

Based on the trend seen by the outer seal, the inner seal was designed to incorporate the most teeth in the available area. This will allow it to seal as well as possible within the current seal height, location width, and necessary pressure restrictions. Because the leakage rate is not critical for this seal, it was decided that high leaks were acceptable. A two tooth seal was implemented in this location. This new seal requires an increase in the lower plenum pressure. Previously, Deux suggested that at operational speed, a pressure of 10 atm would be required to offset the forces on the forward side of the rotor [2]. The new inner seal decreases the lower plenum radius from 1500 micrometers to 900 micrometers. Accounting for the decrease in area caused by the new seal, the new required lower plenum pressure is 27.8 atm. This will be taken into account in the seal structural analysis.

Structural Analysis

A finite element model was used to size the tooth width. Because the inner seal sees a higher pressure differential and thus a higher stress, the inner seal was analyzed to determine the correct seal width. The width was used for both seals. The 3D model consists of a single tooth in an annular construction. Figure 2-5 is a sketch of the model geometry. PATRAN was used to create the model and NASTRAN to do the analysis. Three cases were analyzed for the lower plenum seal. The cases were run at tooth widths of 25, 50, and 100 micrometers. The tooth height was assumed to be 60 micrometers, per the current design for the thrust bearing annulus height, and the radius was assumed to be 900 micrometers based on the available area in the device. The loads introduced were a displacement constraint on the base of the seal,

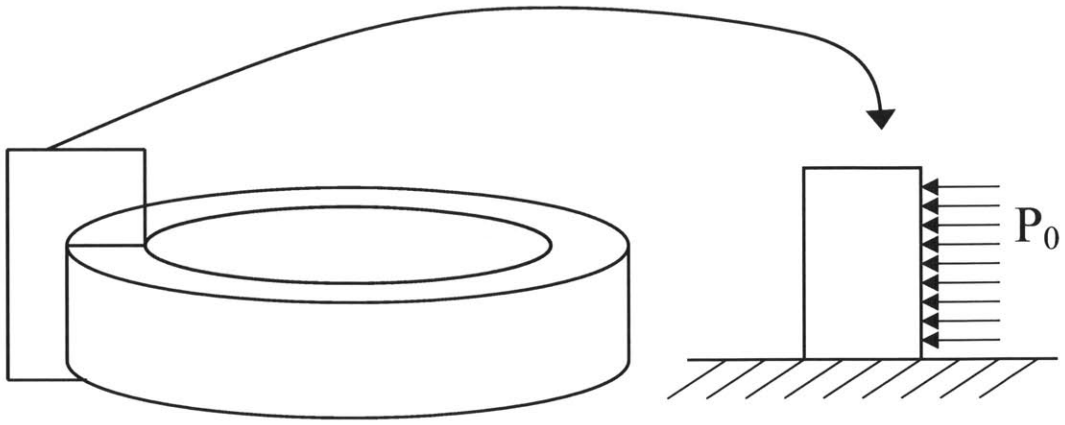

Figure 2-5: Sketch of the full PATRAN FEA model geometry and the cross section with the applied load.

indicating a clamped condition, and a pressure force along the inner wall of the seal. The pressure on the seal was determined by adding in a safety factor of 1.5 onto the new required lower plenum pressure discussed above. The resulting pressure is 40.5 atmospheres.

For each case, a convergence study was completed by looking at the change in the maximum stress for a varying number of elements. For this study, the Von Mises stresses are plotted, accounting for both the principal as well as the shear stresses. The convergence plots can be found in Appendix B. The results of the analysis are summarized in Figure 2-6. The graph shows the maximum principal and shear stresses as a function of the size of the seal. Figures 2-7 and 2-8 show the NASTRAN output illustrating the stress distributions for the 25 micrometer width seal. The yield stress for silicon is approximately 2000 MPa, so all of these seals should be structurally adequate. After discussion with the fabrication team and with consideration to the available geometry, 25 micrometer width teeth were chosen. These are large enough to manufacture easily, small enough to fit the necessary number of teeth into each seal, and strong enough to hold the required pressure.

The next design issue considered was the amount of space that should exist between each tooth. Due to diffusion during the etching process, features that are too

Figure 2-6: Results from finite element analysis.

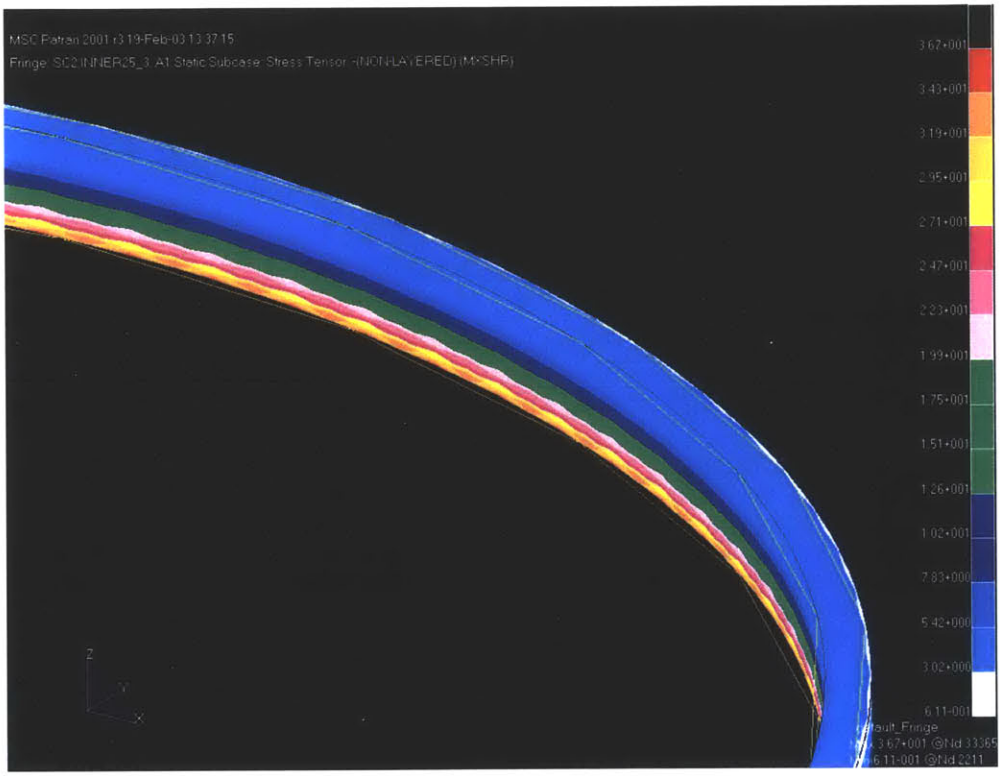

Figure 2-7: Shear stress distribution.

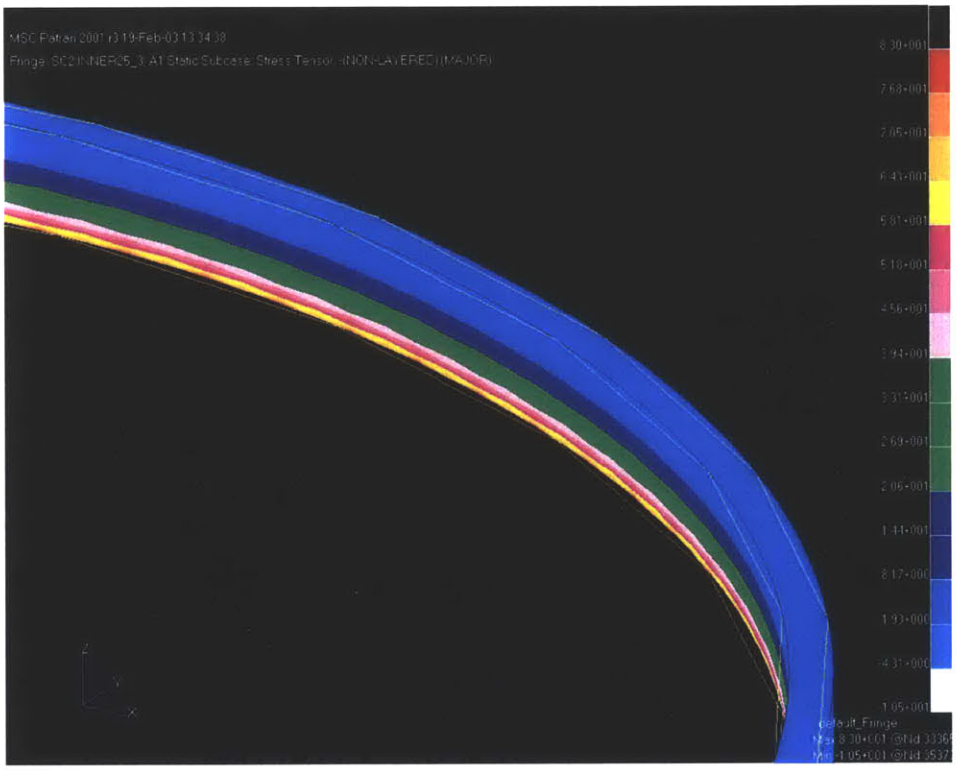

Figure 2-8: Principal stress distribution.

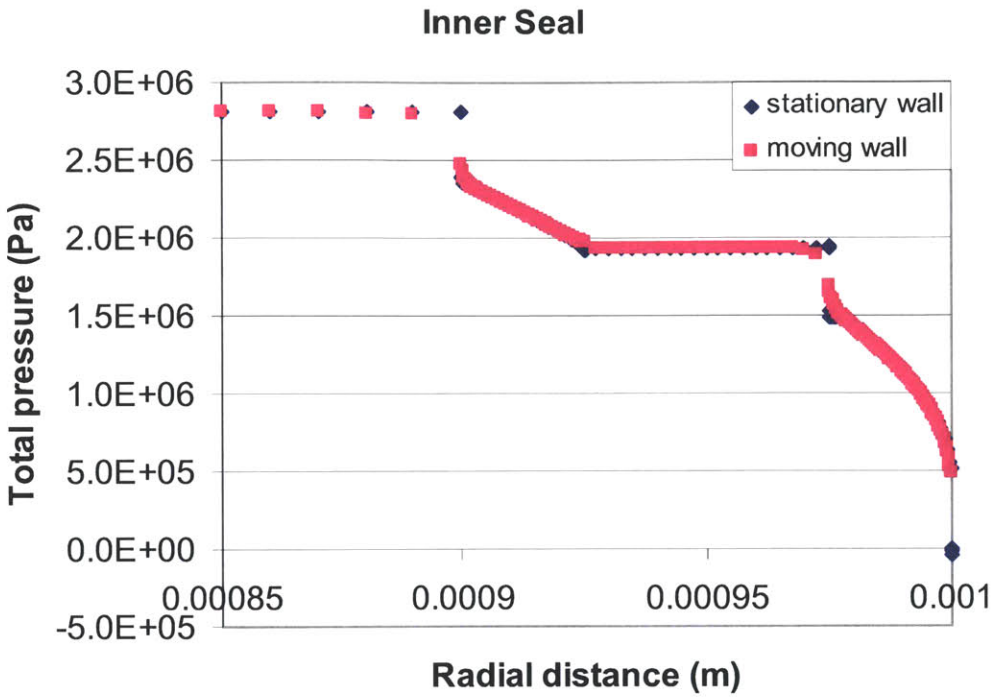

Figure 2-9: Inner seal radial pressure distribution [16].

close to each other can be difficult to manufacture. A larger gap between two teeth also leads to a larger recirculation zone between the two teeth and thus less leakages across the seal. For these reasons, it is desirable to have as much distance between two teeth as possible. Taking available geometry into consideration, 50 micrometers was chosen as the maximum available gap between each set of teeth.

CFD Verification

In order to verify this design, a CFD calculation was completed by Teo [16]. Fluent was used to model both the inner and outer seals. The model assumes an inlet pressure on one side of the seal venting to atmospheric pressure on the other side. The pressure analyzed for the inner seal was determined from the new required lower plenum pressure discussed above. For the outer seal, the pressure was taken from the turbine inlet pressure at design speed. Since the pressure difference across the journal bearing should be no more than 25 PSI, the turbine inlet pressure is a good approximation for the required journal bearing plenum pressure. Figure 2-9 shows

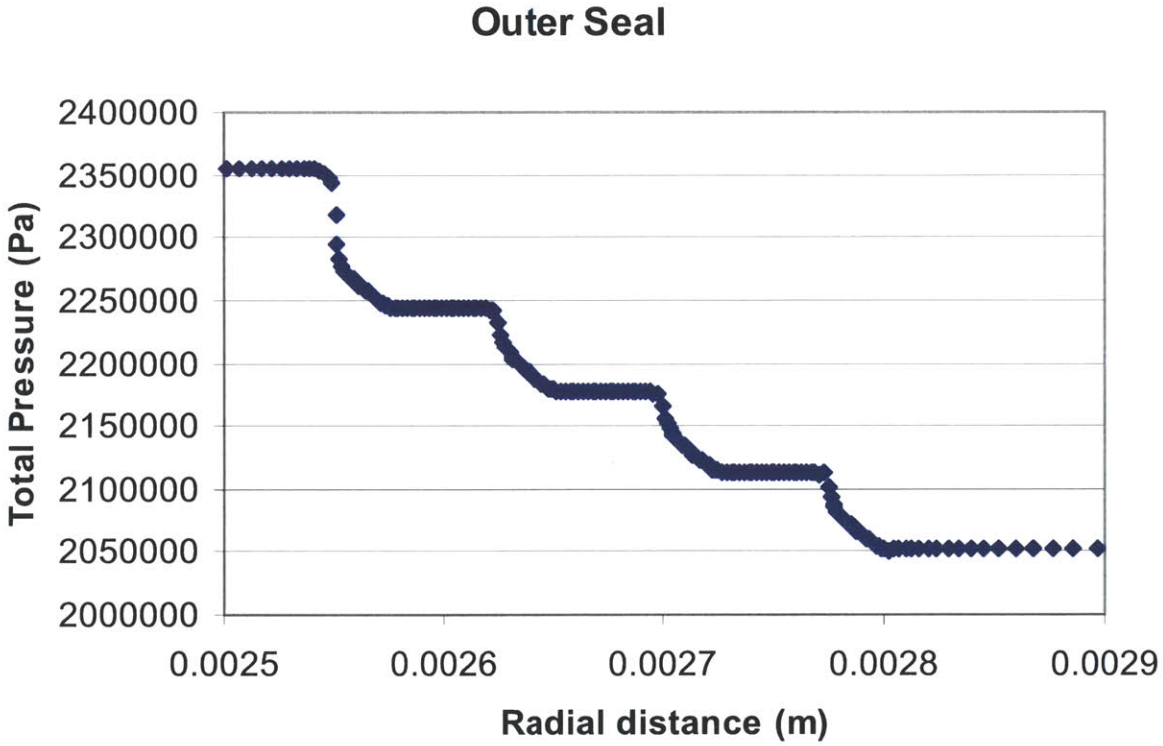

Figure 2-10: Outer seal radial pressure distribution [16].

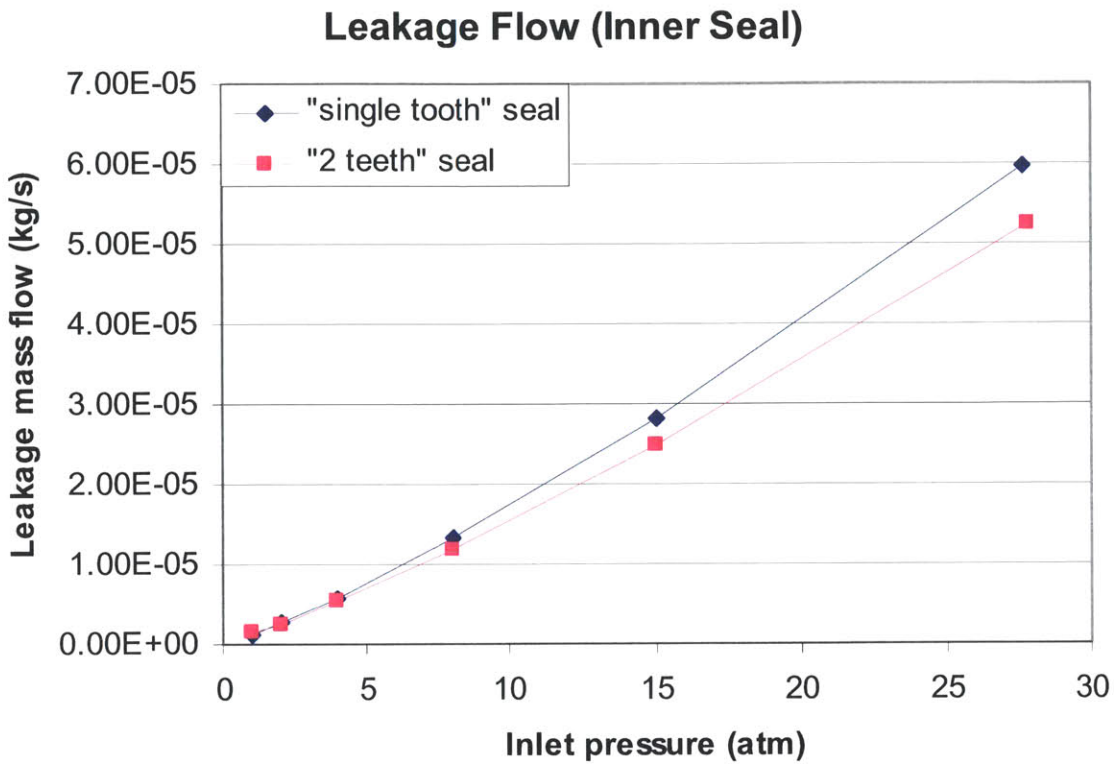

Figure 2-11: Leakage mass flow for inner seal as a function of applied pressure [16].

the total pressure as a function of the radial location for the inner seal, and Figure 2-10 shows the same information for the outer seal. The advantage to the multi-tooth seal can be seen by the high pressure drop at the inlet of each tooth. This also verifies that the distance between the teeth is large enough to achieve a recirculation zone. Figure 2-11 and figure 2-12 show the leak rates as a function of the applied pressure. As discussed above, leaks are acceptable across the inner seal. For the outer seal, preliminary static flow tests indicate that at a journal bearing pressure drop of 25 PSI, a flow rate of 0.13 g/s will be required. The CFD calculation indicates that approximately 0.075 g/s will leak through the seal. This gives a 58% leak at these higher pressures. As there is little room to work with in this area, the only way to further restrict this leak would be to increase the seal height. Increasing the height would create the need for a new fabrication process. It was determined that the higher leak rate was more desirable than designing a new process. Should the need arise, the outer exhaust plenum could be back-pressurized to control this leak. This

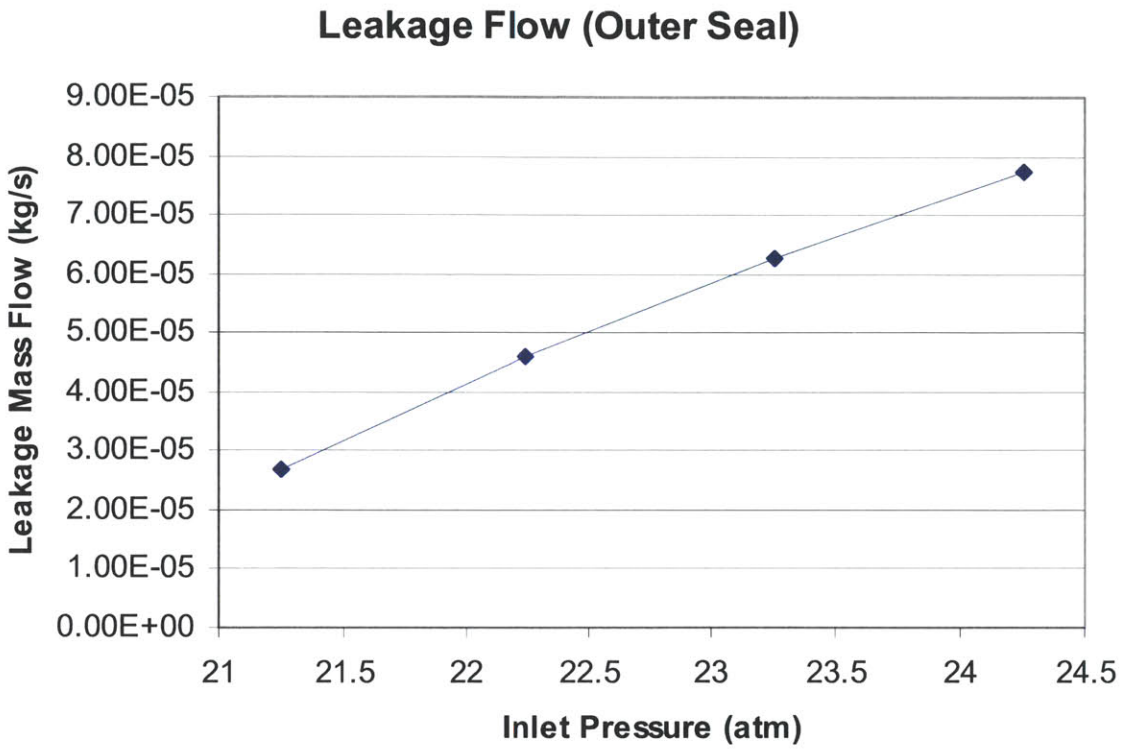

Figure 2-12: Leakage mass flow for outer seal as a function of applied pressure [16].

decision finalizes the seal designs. More detailed output from the CFD model can be found in Appendix C.

Anisotropic Journal bearing

The new design for the turbopump also includes an anisotropic journal bearing. Previous journal bearing plena were designed in such a way as to make the pressurization of the bearing uniform around the circumference of the plenum. Work by Liu suggests that adding anisotropy to the pressurization plenum increases the rotordynamic instability boundary of the device [11]. Figure 2-13 illustrates the difference between an isotropic and anisotropic bearing. The isotropic bearing has equal stiffness in the x and y directions, while the anisotropic has differing stiffnesses in the two directions. Details pertaining to the rotordynamics will be discussed in Chapter 3. By blocking off 25% of the circumference and only pressurizing the remaining 75%, the bearing can achieve a higher speed with a lower tolerance on the upper bound of the bearing

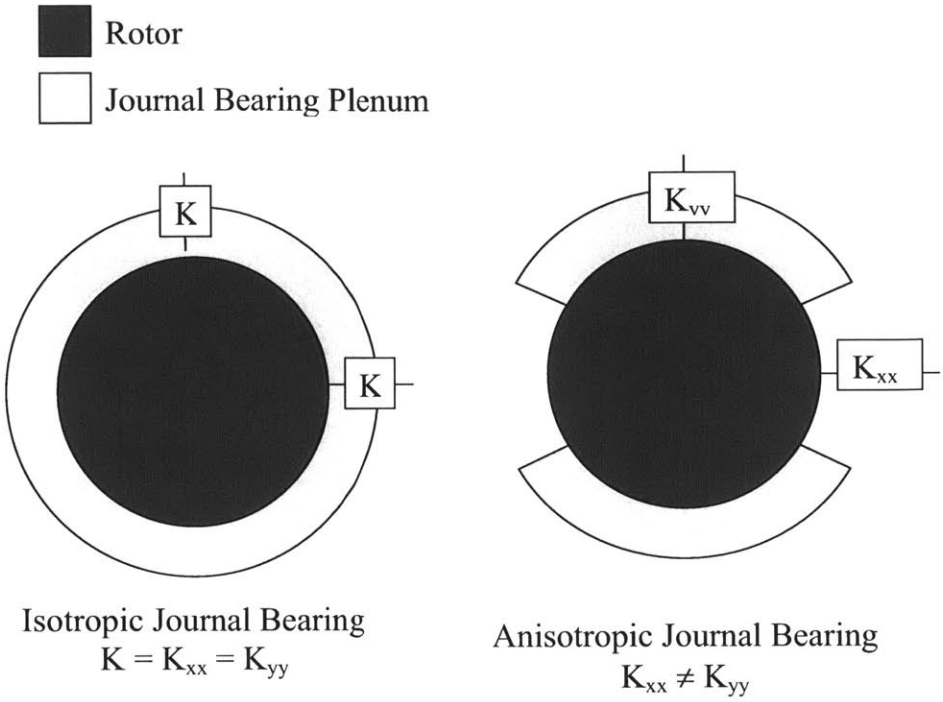

Figure 2-13: The effect of adding anisotropy to the journal bearing plenum.

width. The original specifications on the journal bearing call for a tolerance of plus or minus 1 micrometer. With the anisotropy, bearings that are too wide will still be acceptable for testing.

2.6 Summary

A demonstration micro turbopump is required to test the feasibility of such a device to provide high pressure fuel and oxidizer to the micro rocket engine system. The demonstration micro turbopump consists of 5 micromachined silicon wafers and one pyrex wafer bonded to form the necessary turbomachinery, bearings, plena, and flow passages to create a working device. The original design has been altered to account for experimental challenges and fabrication issues.

The most recent design of the turbopump creates two aft exhaust or aft plena. These will be used to aid in calibration of the axial location and decoupling the aft

pressure system. These new plena required the analysis and design of two new seals on the aft side of the device. This analysis led to the design of two labyrinth type seals, one with two teeth and the other with four. This design also incorporates an anisotropic journal bearing plenum. The next chapter will discuss the experimental test rig and procedures required for testing of the microturbopump.

Chapter 3

Experimental Set Up and Procedures

One of the primary challenges in testing the demonstration micro turbopump is determining successful operating procedures. Most of the previous calculations pertaining to the expected operating conditions of the turbopump [2, 7] focus on conditions at or near the design point. In order to reach this design point, a startup procedure is needed. Guidelines for low and medium speed operations are also critical, taking major instabilities and design constraints into consideration. This chapter will outline the progress made in the operating procedures that has allowed the pump to perform at its current level of operation. It will also discuss the test rig itself.

3.1 Experimental Setup

3.1.1 Pressure Fed Rig and Instrumentation

The rig consists of a water system, which is inherited from the cavitation experiments performed by Pennathur [13], and a nitrogen system that was developed by Jamonet [7] specifically for the turbopump. Both systems are pressure regulated, with mass flow meters on all lines going into the device. The nitrogen lines that feed the bearings have Brooks Instrument thermistor mass flow meters; the turbine and pump lines each

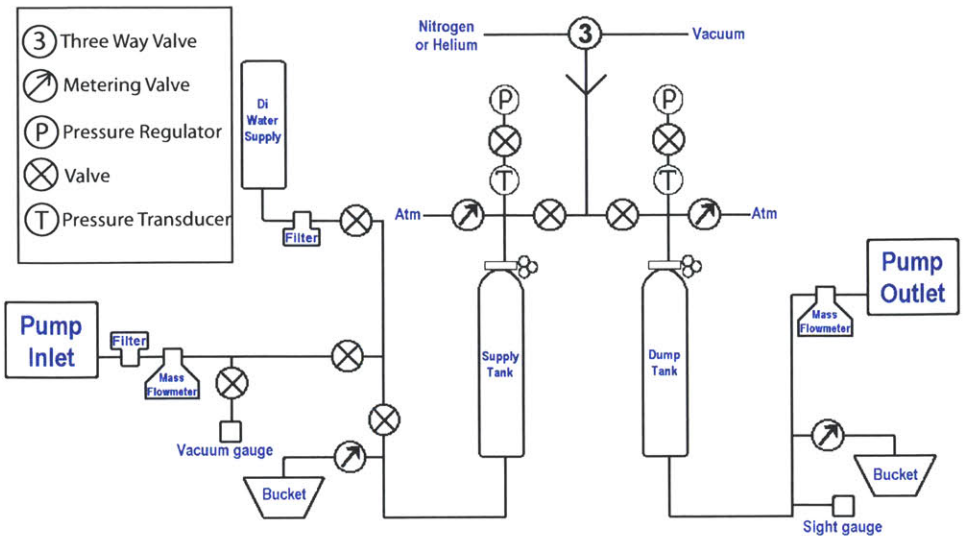

Figure 3-1: Schematic of the water system [13, 7].

have Micromotion Coreolis flow meters.

Some modifications have been made to both rigs allowing for further control or more accurate measurement. Figures 3-1 and 3-2 show schematics of the two systems as they currently exist. The water system, as designed, allows for either a nitrogen source or a vacuum source. This allows the operator to suck water into the tank in order to run a test. From the supply tank, the water goes through a flow meter and into the pump. A small pressure regulator has been added the supply tank to control the pump inlet pressure. The dump tank shown in Figure 3-1 is no longer used because the water from the pump outlet is monitored as it flows into a bucket.

As can be seen in Figure 3-2, there are five nitrogen lines that go into the die. As mentioned above, each nitrogen line is controlled with a pressure regulator in series with a metering valve. The metering valves allow for more precise control of sensitive inlets such as the journal bearing and the turbine inlet. The other lines are controlled directly with the regulators, leaving the metering valves fully open. Both the pump and the turbine are also throttled at the exit. The throttles allow for control of the mass flow through the pump and for control of the turbine exit pressure.

In addition to the mass flow and pressure readings taken on the rig, there are

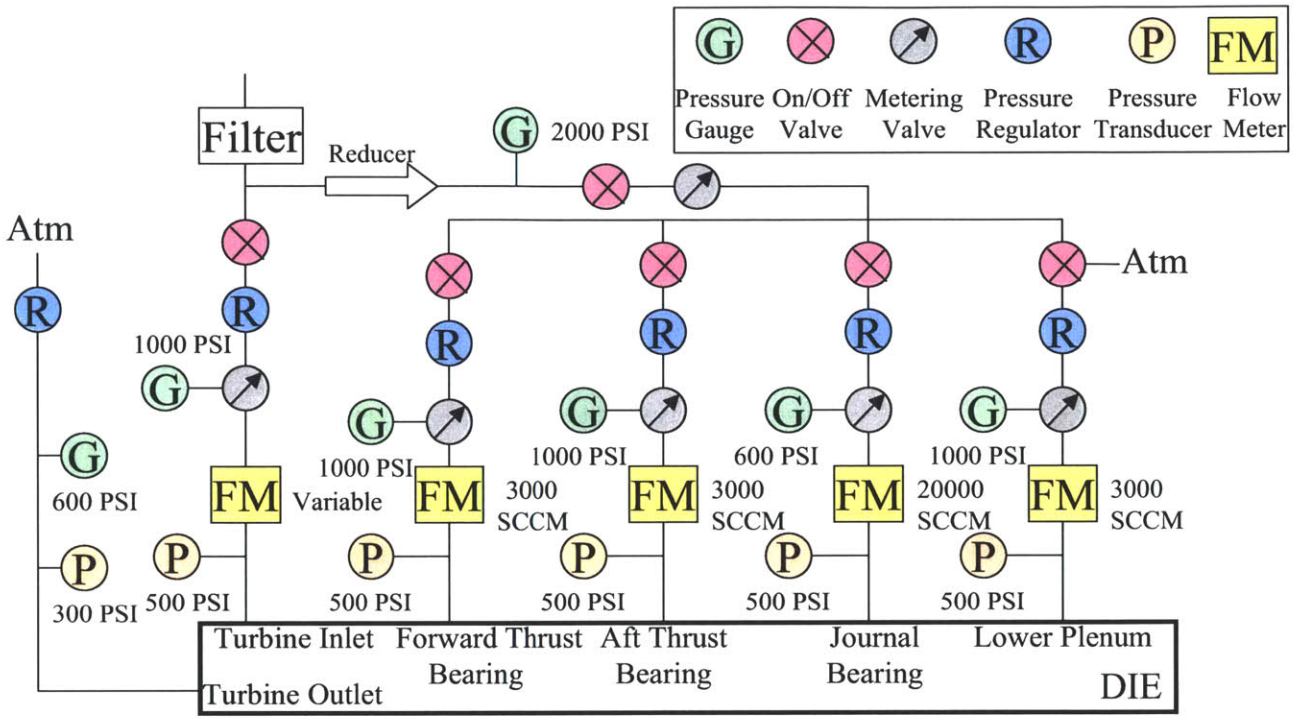

Figure 3-2: Schematic of the nitrogen system.

also pressure taps inside the die. The pressure taps exist at the turbine inlet, turbine outlet, pump outlet, journal bearing plenum, and turbine inter-row. The latter two of these are used to determine the pressure drop across the journal bearing, a critical value for controlling the journal bearing. On the current rig, this value is measured using a differential pressure transducer placed between these two pressure taps, however through build 5 this data was collected by taking the difference between two separate pressure readings. The pressures at the remaining taps are measured with Kulite pressure transducers. Table 3.1 gives an overview of pressure transducers and massflow meters on the rig. Information on the calibration of the pressure transducers as well as an assessment of the uncertainty of the measurements taken can be found in Appendix D.

As discussed in Deux [2] and Jamonet [7], a fiberoptic sensor is used to measure the speed of the device. The fiberoptic shines a laser into the die. The laser reflects off the rotor and the reflection is read by the sensor. The strength of the reflected signal provides a relative measure of the distance the sensor is placed from the rotor. As

Table 3.1: Rig Instrumentation Overview

Instrument	Location	Range
Kulite Pressure Transducer	Water Supply Tank	0-2000 PSI
Kulite Pressure Transducer	Water Dump Tank	0-1000 PSI
Kulite Pressure Transducer	Forward Thrust Bearing	0-1000 PSI
Kulite Pressure Transducer	Aft Thrust Bearing	0-1000 PSI
Kulite Pressure Transducer	Forward Thrust Bearing	0-1000 PSI
Kulite Pressure Transducer	Turbine In Pressure Tap	0-500 PSI
Kulite Pressure Transducer	Lower Plenum	0-300 PSI
Kulite Pressure Transducer	Turbine Out	0-300 PSI
Kulite Pressure Transducer	Turbine In Rig	0-300 PSI
Kulite Pressure Transducer	Pump Out Rig	0-100 PSI
Kulite Pressure Transducer	Pump In Rig	0-100 PSI
Kulite Pressure Transducer	Journal Bearing	0-100 PSI
Kulite Pressure Transducer	Pump Out Pressure Tap	0-100 PSI
Sensotec Differential Pressure Transducer	Journal Bearing Pressure Drop	0-150 PSI
Brooks 5860E Mass Flow Meter	Forward Thrust Bearing	0-2000 SCCM
Brooks 5860E Mass Flow Meter	Aft Thrust Bearing	0-4000 SCCM
Brooks 5860E Mass Flow Meter	Lower Plenum	0-4000 SCCM
Brooks 5860E Mass Flow Meter	Journal Bearing	0-30,000 SCCM
Micro Motion Mass Flow Meter	Pump	Variable
Micro Motion Mass Flow Meter	Turbine	Variable

seen in Figure 2-2, there are 4 "speed bumps" on the rotor. Because these are raised sections, as they pass underneath the sensor they reflect more of the signal back to the fiberoptic than the bottom of the rotor. By measuring the passing frequency of these bumps under the sensor, the rotational speed of the rotor can be determined. In the case of the turbopump, this sensor cannot be placed the required 1.7 millimeters away from the surface of the rotor, due to the thickness of the pyrex top layer. Therefore it is focused using a lens, enabling it to be kept 5 centimeters away instead of only a few millimeters [2].

All of the massflow meters and pressure transducers are read into a data acquisition card that displays the values to the operator through a Labview interface. The data acquisition is discussed in detail by Jamonet [7].

3.1.2 Packaging

In order to connect the test rig to the device, a package must be designed and built. For all demonstration micro turbopumps through and including build 5, packaging designed by Jamonet [7] was used. After the new design of the aft bearing system, a new packaging design was developed.

The general design for the packaging first used by Jamonet is to house all connections from the die to the rig in a single base block that the die sits on. The die is then clamped into position using 4 screws and a top plate. The connections between the micro turbopump and the base block are sealed with BUNA-N o-rings. There is also a spacer plate between the top clamping plate and the base connection block. This spacer plate helps to correctly align the turbopump with the o-rings as well as restricting the clamping to avoid over-tightening the screws and cracking the die. The spacer plate and top clamping plate are located to the base block by use of two 1/8 inch dowel pins. Figure 3-3 is a transparently rendered drawing of the packaging system, showing the fluid connections in the base piece as well as the overall configuration. Figure 3-4 is a picture of the packaged pump.

In order to accommodate the new design, many changes had to be made to the original packaging design by Jamonet. Due to the addition of the two new plena on

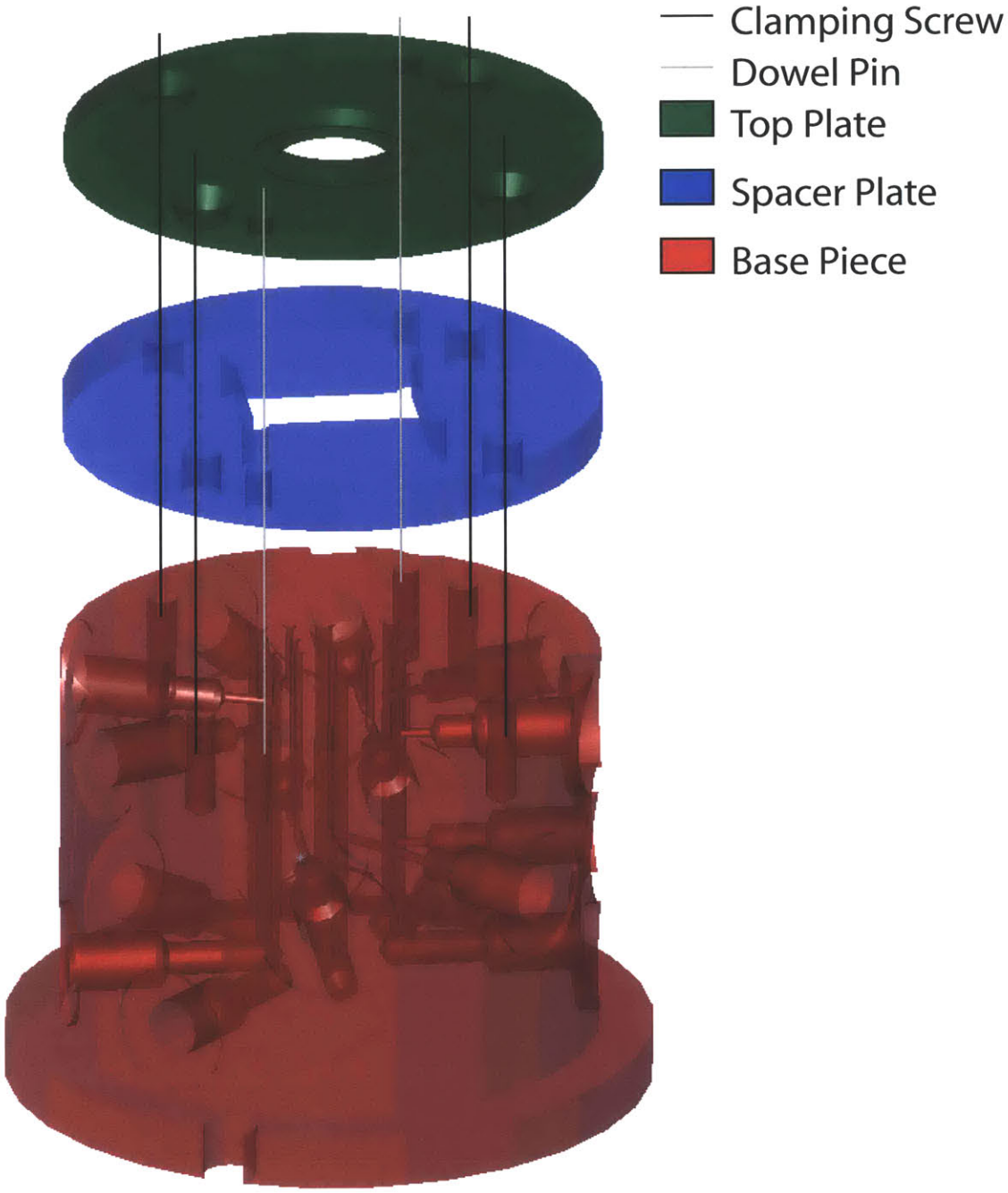

Figure 3-3: Rendered drawing of new packaging system.

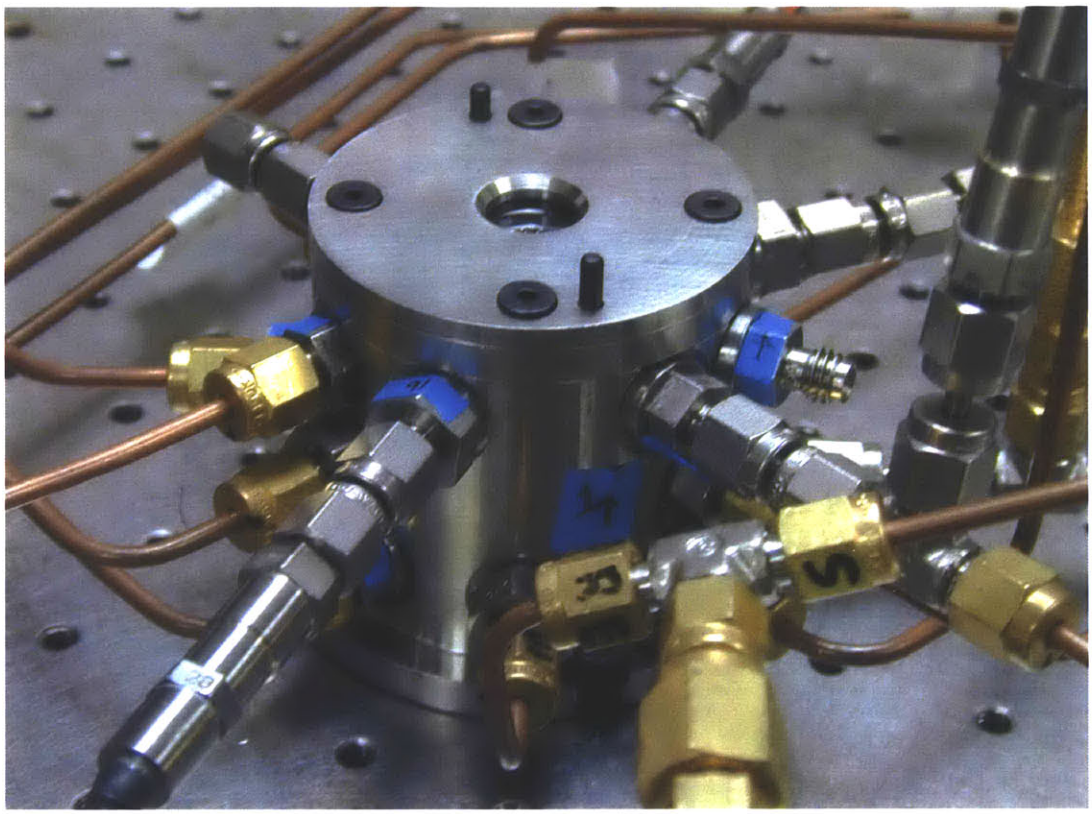

Figure 3-4: Packaged demonstration micro turbopump.

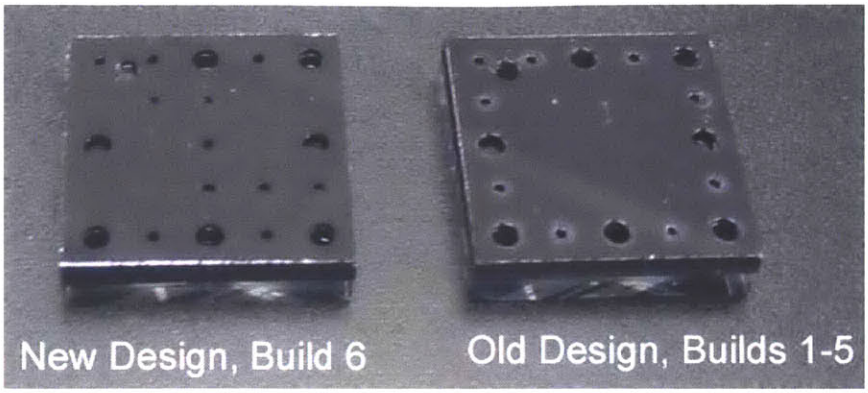

Figure 3-5: Picture of the backside of two pumps showing the added connections.

the aft side and the anisotropic journal bearing, three new channels, and thus three new connections were necessary. The addition of these connections made it impossible to maintain the original die geometry die where all the fluid connections into the die were placed on the outer periphery of the die. Therefore, some connections were moved to the inside of the die. Figure 3-5 shows a picture of the back of an old die and a new die.

The addition of connections to the inner portions of the die leads to an increase in the level of complexity of the packaging. With connections in the center of the die, more depth of packaging is required to avoid crossing lines inside the base connection piece. However, due to the small diameter of the holes in this piece, there is a limit to the depth that can be safely and accurately drilled. The original package designed by Jamonet used a hexagon-shaped block of material and drilled in from the 6 sides on three different depth levels. In order to allow more connections to the device at a given level, the hexagon shape was abandoned for a circular block. Figure 3-6 shows a drawing of the base piece with the connections and their depths labelled.

The package designed by Jamonet connected the rig to the package using Scanivalve fittings. These fittings contain an internal o-ring. O-ring shavings were found inside the die on multiple occasions and inspection of the internal o-rings showed that in some cases pieces of the internal o-rings were missing, presumably shaved off by the connection system and carried into the die by the flow system. The lubricant used

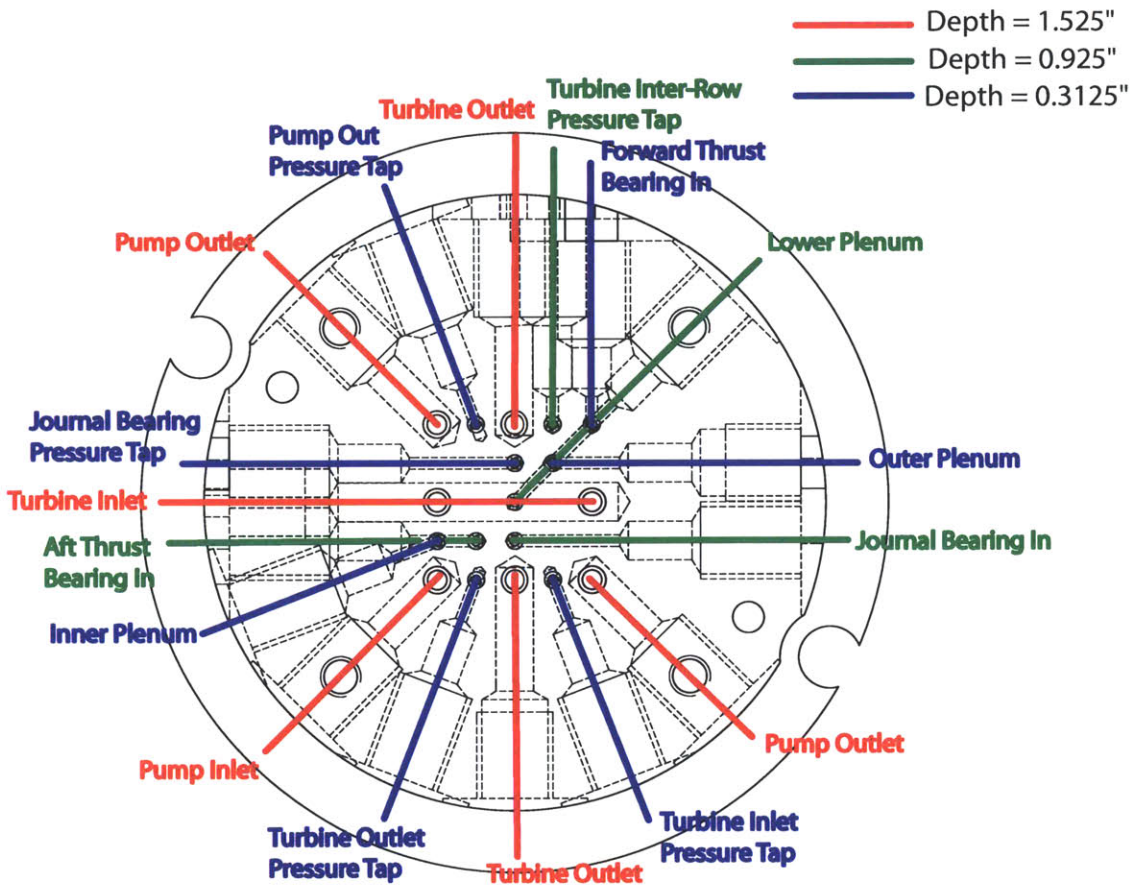

Figure 3-6: Drawing of the package as seen from above with all connections labelled.

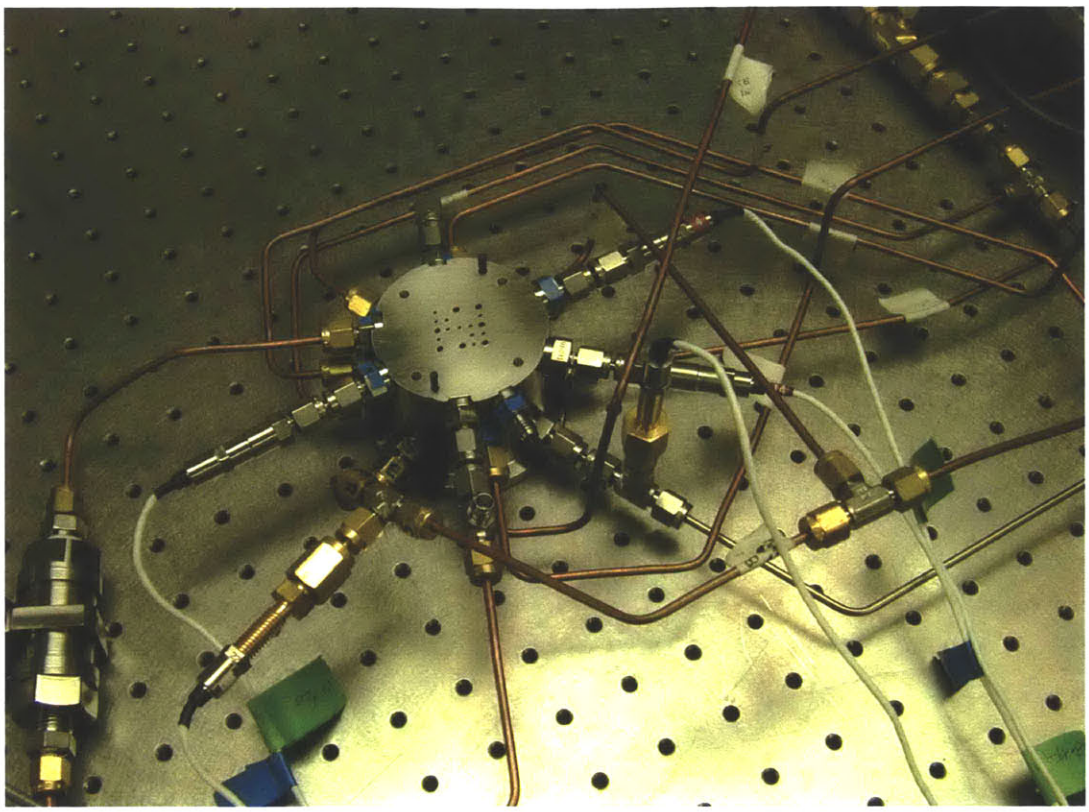

Figure 3-7: Base piece of packaging with all fluid connections and pressure transducers attached.

by the manufacturer of these valves was also seen to redeposit inside the inlet to the valves, raising concerns that it may also redeposit inside the dies. For these reasons, it was decided that the new package would contain only metal to metal connections. The new package connects to the rig with 1/8 inch Swagelock face seal fittings. This fitting requires that each connection have a spot face of at least a 0.56 inch diameter. These face seal fittings are also used for the pressure taps. In these situations, the pressure transducers connect to the face seal fittings by way of a custom attachment piece. Figure 3-7 is a picture of the base packaging piece on the rig with all the fluid connections and pressure transducers in place.

In order to secure the package to the table, a flange was added to the outside rim of the bottom of the base piece. The entire assembly was constructed out of 316 stainless steel. This material was chosen due to its compatibility with hydrogen peroxide, the oxidizer currently planned for use by the microrocket engine system. One of the next

stages in the pumping tests will be to test the pump with 98% hydrogen peroxide as the pumped fluid. In order to prepare for this, the entire package, as well as all hardware connections were designed and built out of stainless steel. The only exception to this is the tubing connecting the rig to the package. Most of the tubing lines are copper because it is easier to work with than steel. The pump inlet tubing line is stainless steel to avoid corrosion.

Due to the complexity of the base piece, as well as the accuracy requirements on the o-ring grooves that create the seal between the die and the base piece, this part was built in a 5-axis precision numerical mill. The part was designed in Solidworks and converted to MasterCAM for the machining process. Appendix E contains the detailed drawings of all three parts of the packaging assembly.

3.2 Testing Strategy

As discussed in Chapter 2, the changes in the aft side allow for more flexibility in the testing strategy by creating more ports on the aft side. This section will discuss the different strategies that were considered as well as explain the current course of action.

3.2.1 Major Factors

The axial thrust balance and stable bearing operation are the two major factors that determine the ability of the rotor to spin up to speed. The axial thrust balance refers to the ability of the thrust bearings and lower plenum to balance the pressure forces on the top and bottom of the rotor. The thrust bearings were designed to perform optimally when the rotor is centered between the forward and aft thrust bearings. In order to ensure operation close to this position, the pressure forces on the forward side need to closely match the pressure forces on the aft side. Because all of the turbomachinery for the turbopump is on the forward side, careful consideration of the plena on the aft side is needed to match the forces.

Both the thrust bearing system as well as the journal bearing will be discussed in

detail in Chapter 4, but it is important to understand that the thrust bearings for the rotating turbomachinery in the microengine projects have been traditionally used as an axial position indicator. As the rotor moves, the gap between the rotor and the thrust bearing pad changes, changing the flow resistance that the thrust bearing flow sees and thus affecting the flow rate, which is measured on the rig. By monitoring this during operation, the axial location can be inferred. Having an axial location indicator is considered a critical piece of information for stable and safe operation of the micro turbopump.

3.2.2 Axial Thrust Balance Model

After redesigning the aft thrust bearing system as discussed in Chapter 2, a number of options for how to best utilize the new aft plena were analyzed. As the axial thrust balance is both a major factor and difficult to quantify experimentally, a model was developed to explore the axial thrust balance of the rotor. This model uses the pressures injected into the device at specific locations along the rotor and integrates the pressure forces over the surfaces of the rotor to get a net force on the rotor. It also plots the pressure distribution across the rotor. In locations where the rotor is in contact with a static plenum, such as the area above the lower plenum, the pressure force is given as the pressure multiplied by the area of the rotor in contact with that plenum. In the cases where there is a radial pressure gradient, such as through the pump blades, the gradient is assumed to be linear to simplify the model and the resulting pressure function is integrated over the area it occupies. Data output from this model will be used to describe the strategies discussed in the rest of this section.

The approximations made by this model are meant to produce quick, simple results and plots that increase the understanding of the axial thrust balance problem. The model does not take piping losses into account or make an accurate estimate of the pressure variation through the turbomachinery. This model cannot be used to accurately estimate the rotor location, however it does give valuable insight into the general pressure variation across the rotor. It can also be used to look at the first-order approximation of the rotor sensitivity to changes in the pressures in the

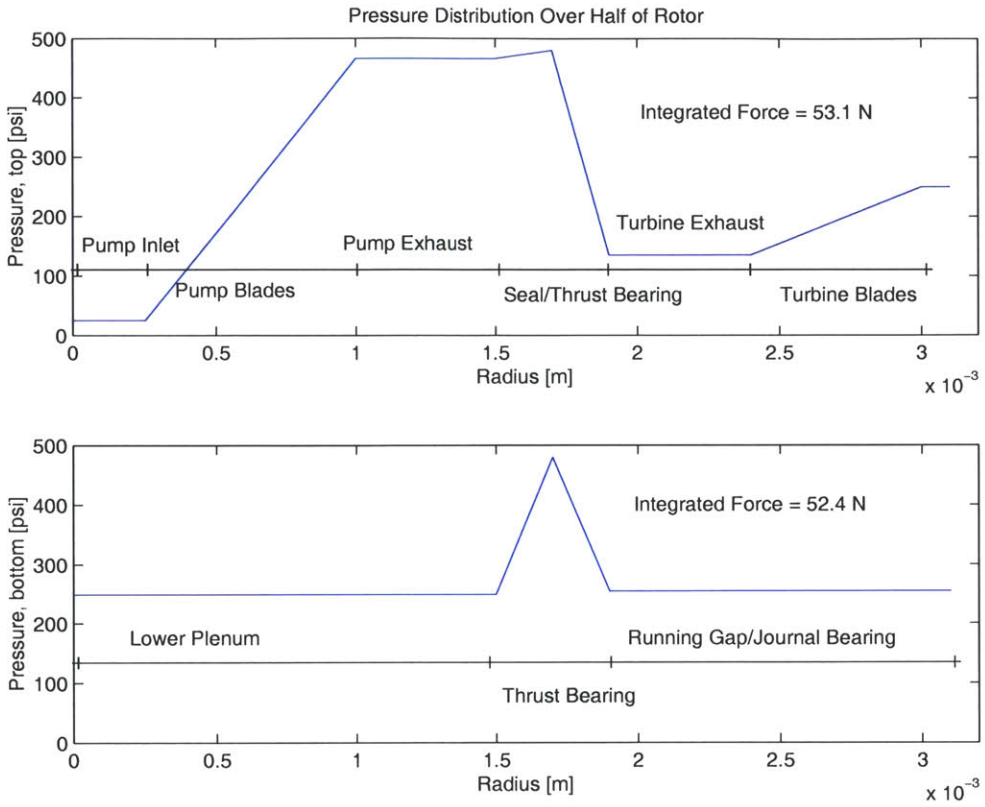

Figure 3-8: Pressure distribution for original design.

aft plena.

3.2.3 Original Testing Scheme

The original testing scheme, before the inclusion of the aft decoupling plena, calls for the majority of the thrust balance to be controlled with the single lower plenum. Since the original design has only the aft thrust bearing and lower plenum on the aft side, all the thrust force from the forward side must be compensated by adjusting the pressures at these two locations. As originally designed, the two thrust bearings are kept at a constant pressure and the lower plenum is used to account for the rest of the thrust balance. Figure 3-8 shows the pressure distribution of the rotor as a function of radial position at design speed when operated in this scheme. As discussed above, the thrust bearings and their flow rates are used as the axial position indicators in this scenario.

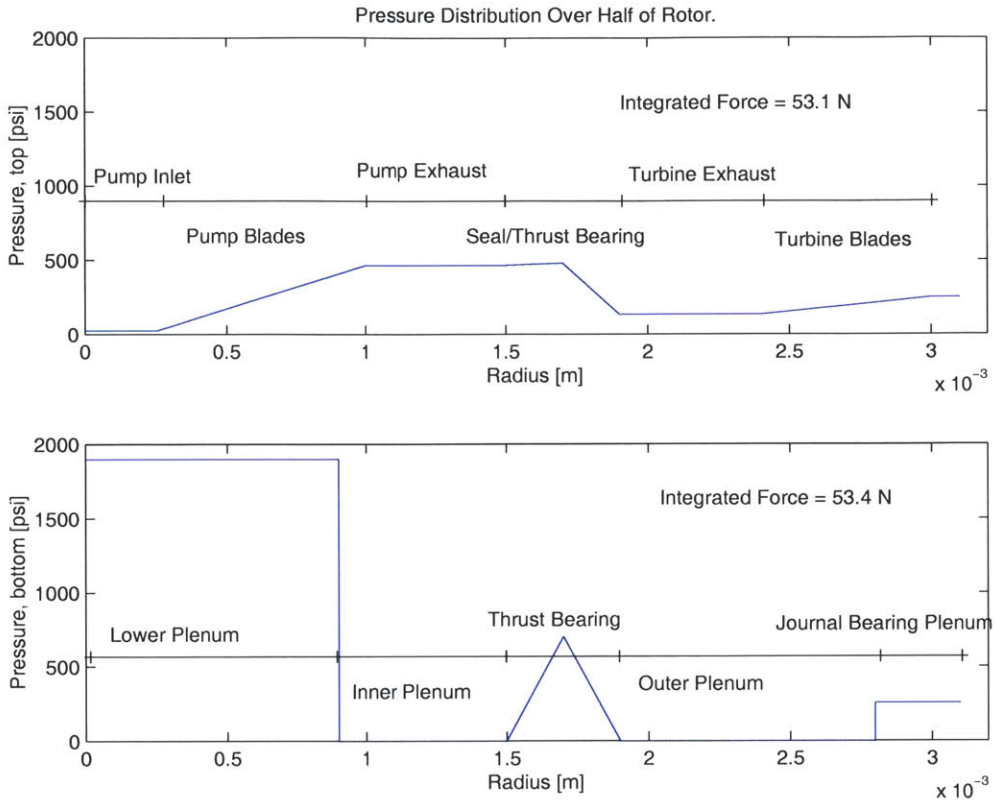

Figure 3-9: Pressure distribution for new aft design without self-balancing.

Taking this strategy and applying it to the design including the two additional aft plena, these new plena are vented, and the center lower plenum pressure is increased to balance the force on the top side of the rotor. Figure 3-9 shows the pressure distribution on the rotor at design speed when operated in this scheme. Because the lower plenum is smaller in the new design, the lower plenum pressure must be much higher at design speed for this scenario. This realization led to the suggestion that the two new aft plena may be utilized in such a way as to allow the rotor to balance itself.

3.2.4 Axially Self-Balanced Rotor Concept

The concept of the self-balanced rotor was first suggested by Ehrich [3]. The idea is to connect the plena on the aft side to pressure lines on the forward side to attempt to match the pressures with as little external balancing as possible. The axial self-

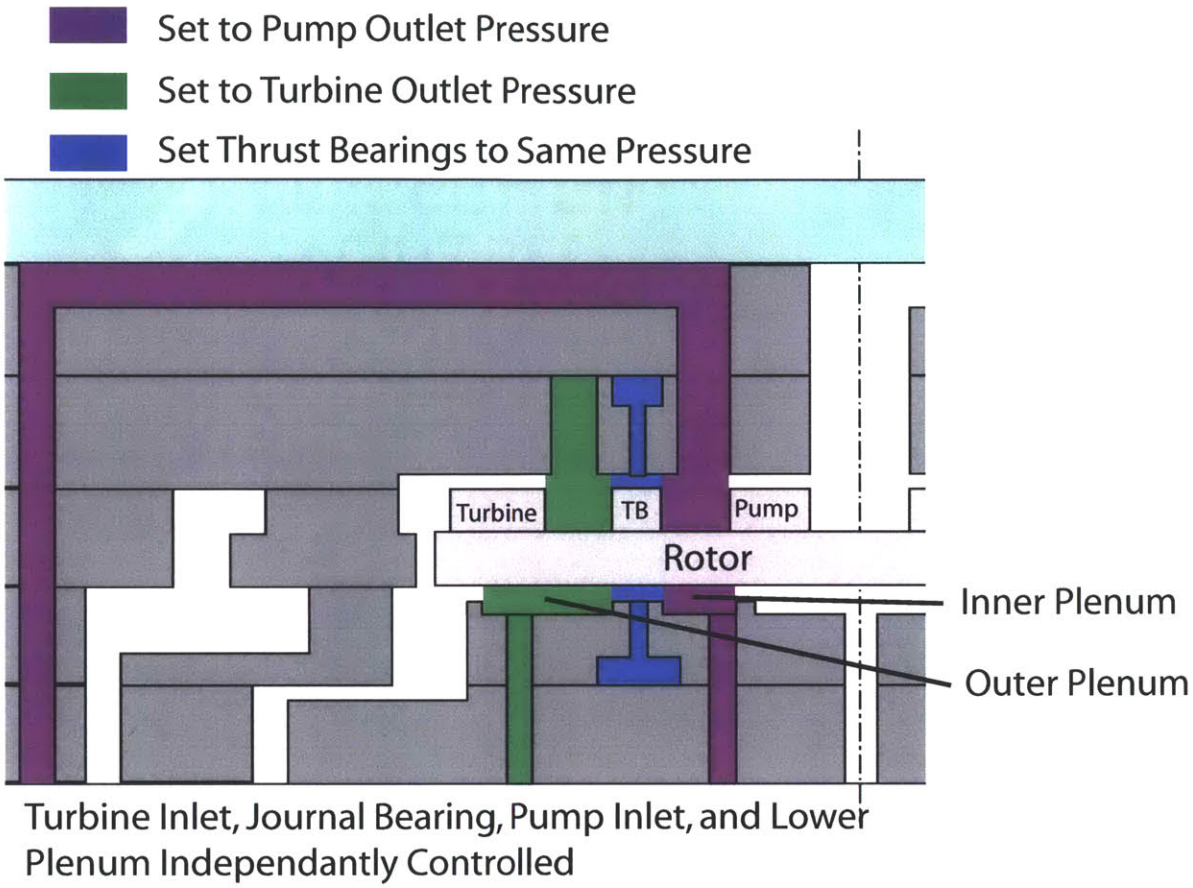

Figure 3-10: Sketch showing the axial self-balanced rotor concept.

balanced rotor concept is illustrated in Figure 3-10. By connecting the pump out pressure line to the inner plenum and the turbine out to the outer plenum, most of the pressure force of the rotor will balance automatically as the rotor spins up. Figure 3-11 shows the axial balance model results for this concept at design speed. Since the point of this operating scheme is to match the two sides of the rotor as closely as possible, the pressure distribution on the top and bottom sides is much more closely matched than the original concept.

Running the pump in this way has the added advantage of creating identical discharge conditions for the thrust bearings on the forward and aft side. Assuming that the geometry of the thrust bearing nozzles is identical, at a given pressure the forward and aft side should have nearly identical flow rates. For the operator to

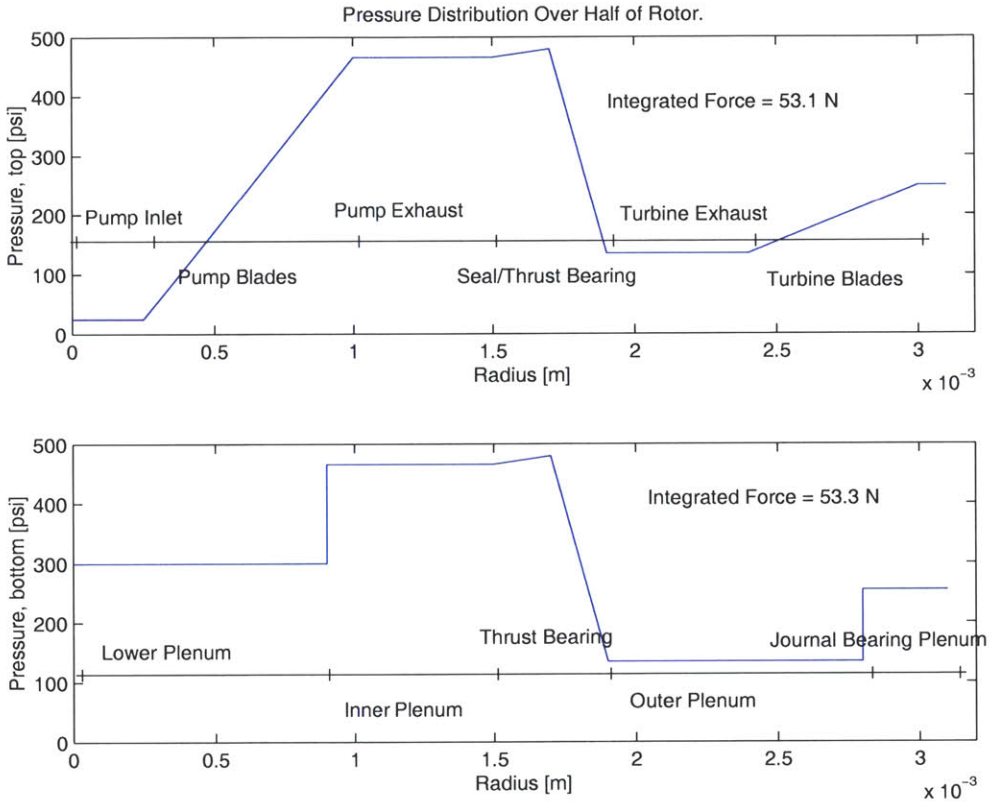

Figure 3-11: Pressure distribution for the axial self-balanced rotor concept.

maintain a centered position, the lower plenum pressure should be adjusted until the bearings have equal flows. Therefore, the axial thrust balance could be achieved by turning a single knob (the lower plenum pressure) as opposed to operating each of the thrust bearings and the lower plenum separately. Another advantage is the decrease in the sensitivity of the lower plenum pressure. In the original design, the lower plenum needs to be adjusted approximately 1400 PSI from a stationary rotor to a rotor spinning at 750,000 RPM. For the self-balanced design, the lower plenum would need to be adjusted 350 PSI across the range of speeds.

The major disadvantage to this method is the re-coupling of pressures on the aft side. Once again, complex 3D flows will be produced on the aft side. The lack of an aft exhaust will make venting pressure from the aft side more difficult. By connecting the plena to pressure inlets instead of using them as exhausts, single changes in any of the system inlets can have effects on the thrust of both sides. Another concern is the possible introduction of water to the aft side. The added drag caused by water flowing into the aft side is not acceptable from the standpoint of system power. This concept would need to be implemented carefully to ensure that the aft side stays free of water.

3.2.5 Partially Balanced Axial Thrust Concept

A final method suggested involves using the turbine inlet air for partial automatic balancing. This method connects the outer plenum to the turbine inlet supply. A sketch of this scenario is shown in Figure 3-12. The larger area of the outer plenum, in comparison to the lower plenum, allows this method to give a larger aft side restoring force at a lower pressure than the original suggested lower plenum pressure. As can be seen by Figure 3-13, at design speed, the outer plenum is able to almost completely balance the forward side of the rotor, leaving the lower plenum at a much lower pressure than the previous two schemes.

By using the inner plenum as an exhaust, the pressure-flow relation of the inner seal can be used as an axial position indicator. All of the lower plenum flow will exit the device through this exhaust. This flow rate will be restricted by the seal

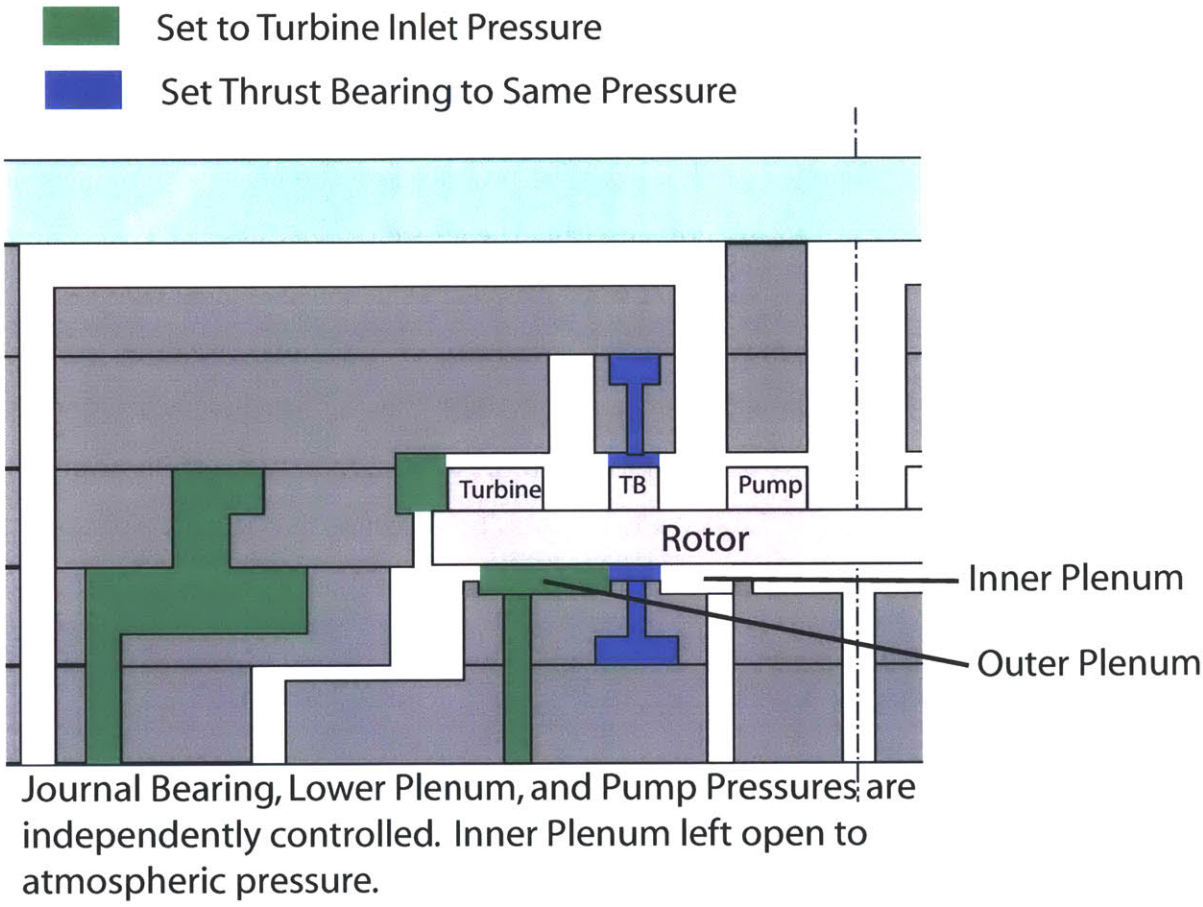

Figure 3-12: Sketch showing the partially balanced concept.

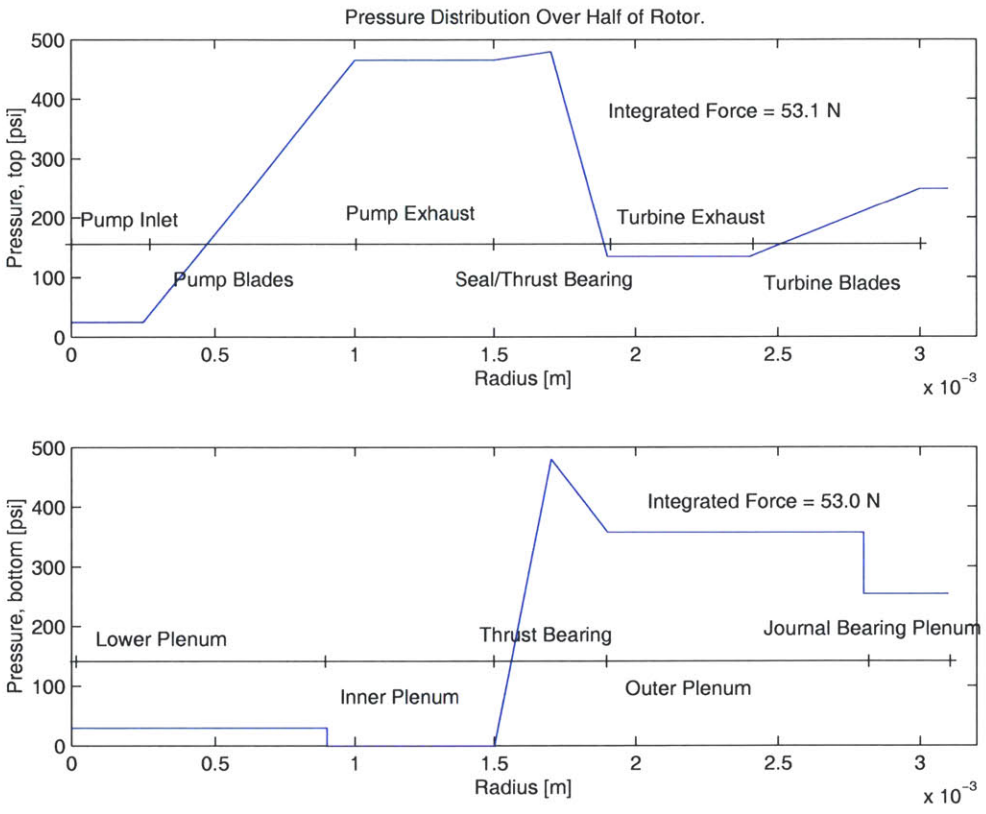

Figure 3-13: Pressure distribution for the partially balanced concept.

between the lower and inner plena. By monitoring the lower plenum flow rate, the axial position of the rotor can be inferred. In terms of the sensitivity of the lower plenum, this method is better than even the self-balanced concept, requiring a 5 PSI change in the lower plenum pressure across the range of speeds.

3.2.6 Conclusions

Although the self-balanced concept is the most attractive from an ease of operation point of view, it has been decided that for the time being, this operating scheme does not offer enough control on the aft side. All of the aft pressures are coupled to the forward pressures. The added risk of water in the aft side of the device is also of serious concern. The partially balanced concept allows for easier operation than the original scheme and allows the operator to maintain independent control over most of the device, allowing for more flexibility in operation. For these reasons, the partially balanced concept has been adopted for the time being, with the self-balanced concept to be further investigated at a later date.

3.3 Startup Procedure

Previous work on the demonstration micro turbopump illustrated the difficulties of starting the pump [7]. Development of a starting procedure was one of the integral steps in obtaining pumping data. The following section will discuss the development of the procedure used to start the pump.

3.3.1 Priming the Pump

One of the challenges associated with starting the micro turbopump is that of priming the pump. In general, there are two ways to get the liquid into the pump. Either start with the liquid in the pump and then spin it up to speed or inject the fluid into the pump while it is already spinning. Multiple pumps were destroyed by attempting the second of these two options. When a liquid is injected into a pump that is already

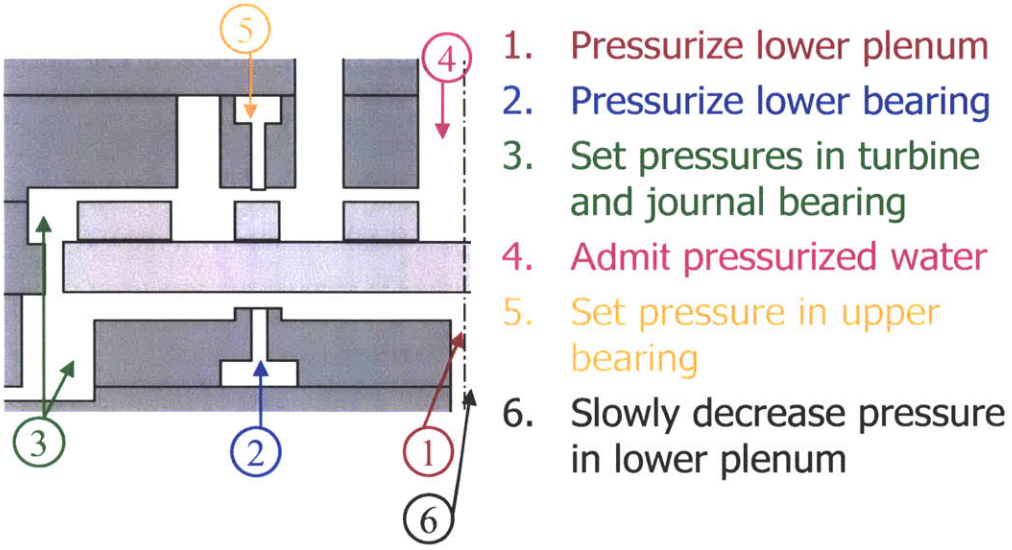

Figure 3-14: Overview of the starting procedure.

spinning, the high density fluid is unable to flow into the pump without causing a large momentum transfer as it is injected. This option has been shown to cause the rotor to crash and break even at low speeds.

In order to ensure safe startup, it is necessary to prime the pump with water before starting the main turbine air and without the use of the gaseous seal. The gaseous seal cannot be used in startup because the low pressures at the pump outlet allow for large amounts of nitrogen to enter the pump, creating bubbles, which inhibit steady operation. To maintain the seal, a startup procedure was developed that utilizes the thrust bearings and back plenum to create a mechanical seal while priming the pump. A summary of the full starting procedure is shown in Figure 3-14.

Priming the pump requires the use of all of the plena on both sides. First, the aft plena are pressurized to hold the rotor in place against the forward thrust bearing. The pressures in the turbine, journal bearing, and thrust bearings are set to their appropriate values, depending on the startup speed required. Pre-pressurized water is admitted into the pump, priming it. The final step is to slowly decrease the pressure in the lower plenum until the rotor falls and is supported solely by the gas bearings.

This startup procedure has worked successfully to start the pump on all tests

presented. Starting the pump in this way allows the pump to start spinning at speeds of approximately 25,000 RPM. By setting the pressures in the turbine and journal bearing correctly, this "jumping" method allows the pump to start up above the journal bearing natural frequency which is discussed below. By jump starting, many of the difficulties associated with low speed operation can be avoided.

3.3.2 Rotordynamic Considerations

Once the pump begins to spin, and before it can be run up to high speeds, it must cross the first natural frequency of the journal bearing [7]. When the rotor passes through this natural frequency, the whirl amplitude of the rotor increases, creating large amplitude oscillations in the motion of the rotor. Crossing the natural frequency must be accomplished in a regime where the journal bearing supplies adequate damping to allow the rotor to operate through this region. Analytically, the damping ratio has been shown by Spakovszky and Liu to vary as

$$\zeta = \frac{1}{\sqrt{\frac{\Delta P}{P_0}}} \tag{3.1}$$

where ΔP is the pressure drop across the journal bearing. This implies that higher damping will be achieved at smaller values for the pressure drop across the journal bearing. Experimentally this has been supported by successfully crossing the natural frequency at low values for the pressure drop across the journal bearing [15]. As discussed above, problems with crossing the natural frequency of the journal bearing can also be addressed by starting the device above the natural frequency curve.

There is also a dynamic instability that occurs at higher speeds and that cannot be crossed. This will be discussed in detail in the next chapter. Both the journal bearing natural frequency and instability boundary change with the pressure drop across the journal bearing. In order to avoid reaching this instability boundary or crossing below the natural frequency at high speeds, the device is operated through a "stair-step" method as shown in Figure 3-15. The operator wants to cross the natural frequency at a low speed and low journal bearing pressure difference and

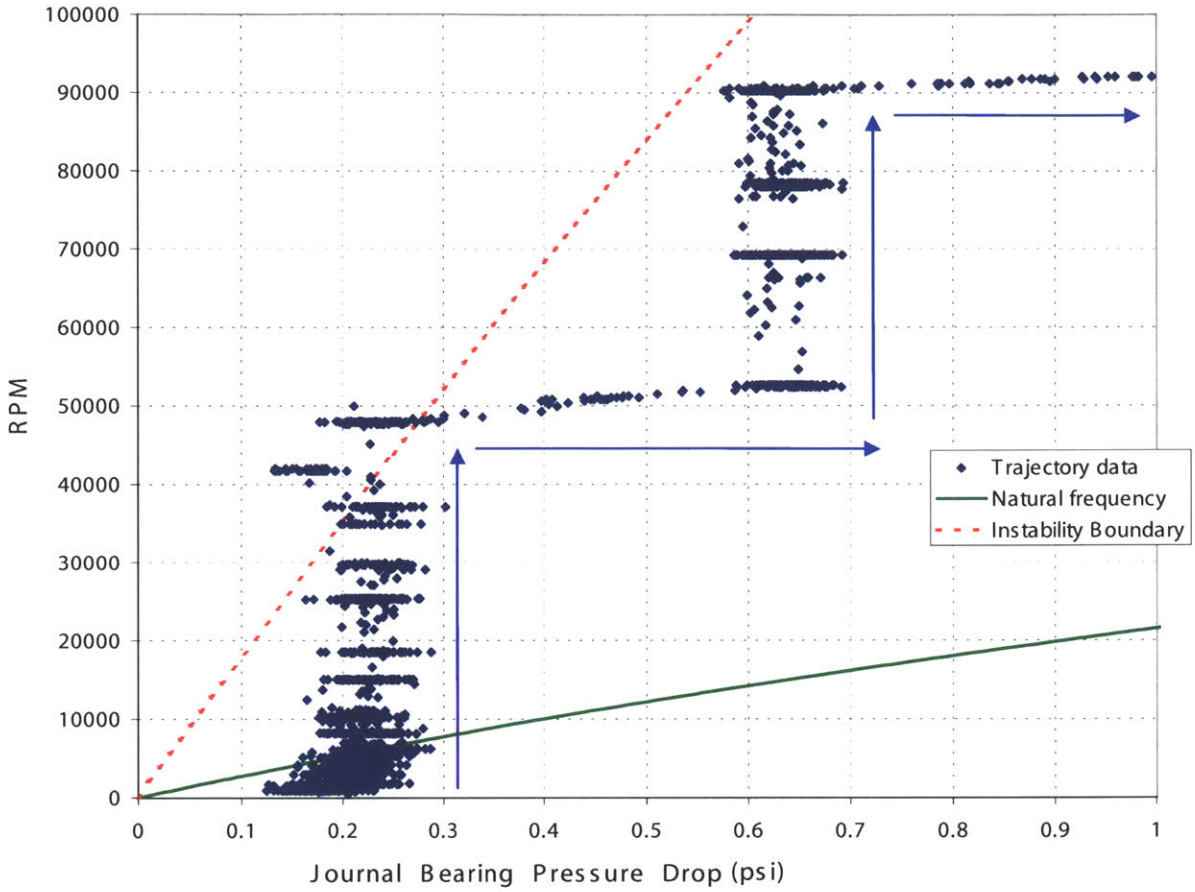

Figure 3-15: Example trajectory that might be taken in order to spin a die up to speed [7]. Instability boundary and natural frequency shown are analytical estimations.

then stay between the natural frequency and instability boundary at higher speeds. The operator oscillates between increasing the speed and increasing the pressure drop across the journal bearing in order to successfully bring the pump up to speed. More theory behind the journal bearing will be discussed in the next chapter [10].

3.4 Experimental Phenomena and Challenges

There are many considerations that must constantly be taken into account when running the turbopump. This section will discuss a few of the problems encountered during testing.

3.4.1 Maintaining the Forward Seal and Single Wafer Rotor Implications

One of the unique aspects of the turbopump is the single wafer rotor construction. The advantage to this design is the lower rotor static imbalance and easier fabrication than a double wafer rotor. The disadvantages are the need for an annular seal to separate the liquid and gas flows and the problems discussed previously pertaining to axial thrust balance. There have been experimental difficulties operating with water from the pump discharge leaking into the seal, as well as with gas leaking out of the seal into the pump discharge. To avoid this, the seal is operated such the gaseous outlet of the seal matches the pump discharge pressure. This mode of operation is difficult to maintain as the rotor speed increases.

Water leaking into the seal causes increased drag in the location where the leak occurs. Whether a water leak across the seal happens at all radial locations simultaneously, or only in a few circumferential sectors is unclear, but in either case, the results are an increase in drag that either slows the rotor quickly to a low speed or could cause a crash.

Because of the viewing window at the pump outlet, observation is possible for in situation where air leaks into the pump outlet from the seal. In all cases where this occurred, an oscillation in speed was seen and recorded by the fiberoptic data. This phenomena was discussed by Jamonet [7]. It has since been suggested that the reason for this oscillation is the loading and unloading of the pump. The nitrogen bubbles conglomerate, forming a large bubble that moves into the pump blades, momentarily causing the pump to be running in nitrogen gas instead of water. The excess power is then diverted to accelerating the pump up to speed quickly. This increase in speed causes the bubbles to be entrained out of the flow, once again filling the pump with water and slowing it down to near its previous speed and pressure rise, which allows more bubbles to enter, starting the cycle over again.

Because the pressure loss across the seal land is determined in large part by the gap between the rotor and the seal, the axial location plays a role in the matching

of the pressure at the exit of the seal to the pressure at the exit of the pump. Also, the experimenter controls both the inlet pressure of the pump as well as the inlet pressure of the bearing nitrogen. Adjusting these also affects the pressure balance at the critical liquid to gas interface. The situation at this interface is not well understood and is difficult to control.

3.4.2 Forward Bearing Pull-In Force

In normal operation, if the operator wants to move the rotor up or down inside the thrust bearing gap, the pressures in the thrust bearings are modified. Increasing the pressure in one bearing should push the rotor away from that bearing, increasing the gap on that side and thus the flow rate through that bearing. The change in location is monitored using the flow rate through the bearing.

In some tests, the thrust bearing exhibited the opposite behavior. As the pressure on the forward side of the rotor was increased, the flow rate through the forward thrust bearing decreased, indicating that the rotor was moving closer to the thrust bearing on the forward side. The data indicating this is shown in Figure 3-16. Here, the decreasing value of the forward thrust bearing flow indicates that the rotor is moving towards the forward side. In this case, the speed of the pump, and thus the turbine inlet and pump outlet pressures, were increasing while the thrust bearing pressure remained constant. One hypothesis explaining this behavior involves the change in the surface tension force caused by the meniscus between the water from the pump and the nitrogen from the bearing. A sketch of the sealing situation in the pump is shown in Figure 3-17. Balancing the pressure forces and the surface tension forces gives

$$2\pi r h(P_b - P_p) = 2(2\pi r \sigma_{water} cos\theta) \tag{3.2}$$

and rearranging this to get the gap as a function of the pressure difference yields

$$h = \frac{2\sigma_{water} cos\theta}{P_b - P_p} \tag{3.3}$$

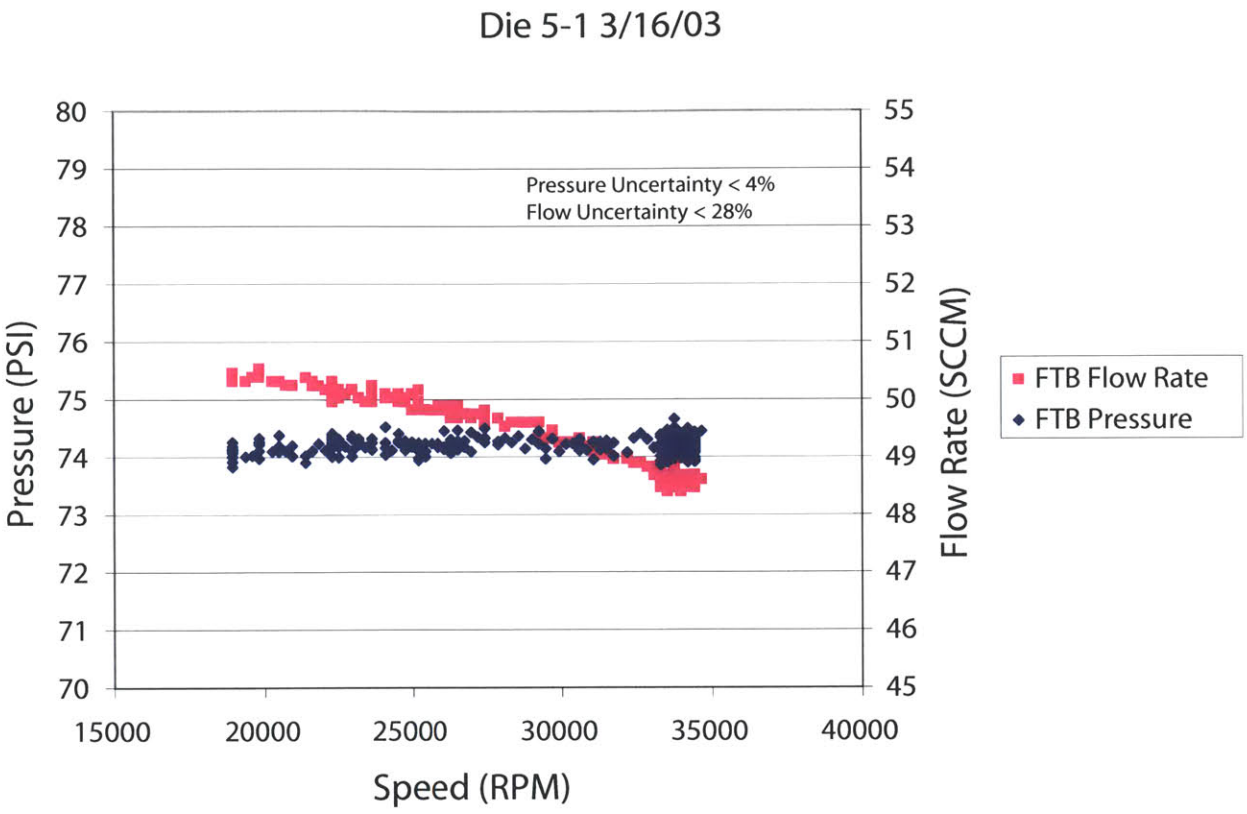

Figure 3-16: Data for the forward thrust bearing indicating a pull-in force.

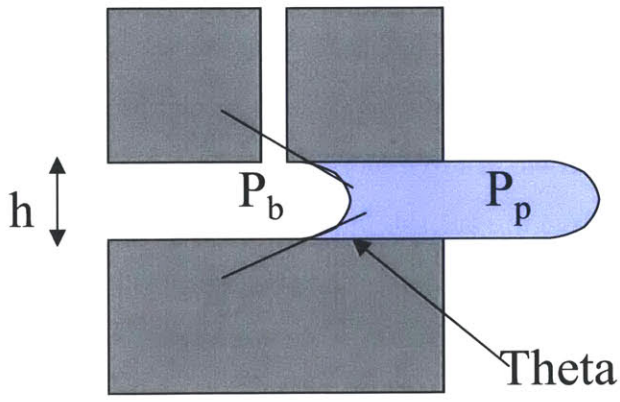

Figure 3-17: Sketch of the meniscus inside the forward thrust bearing pad.

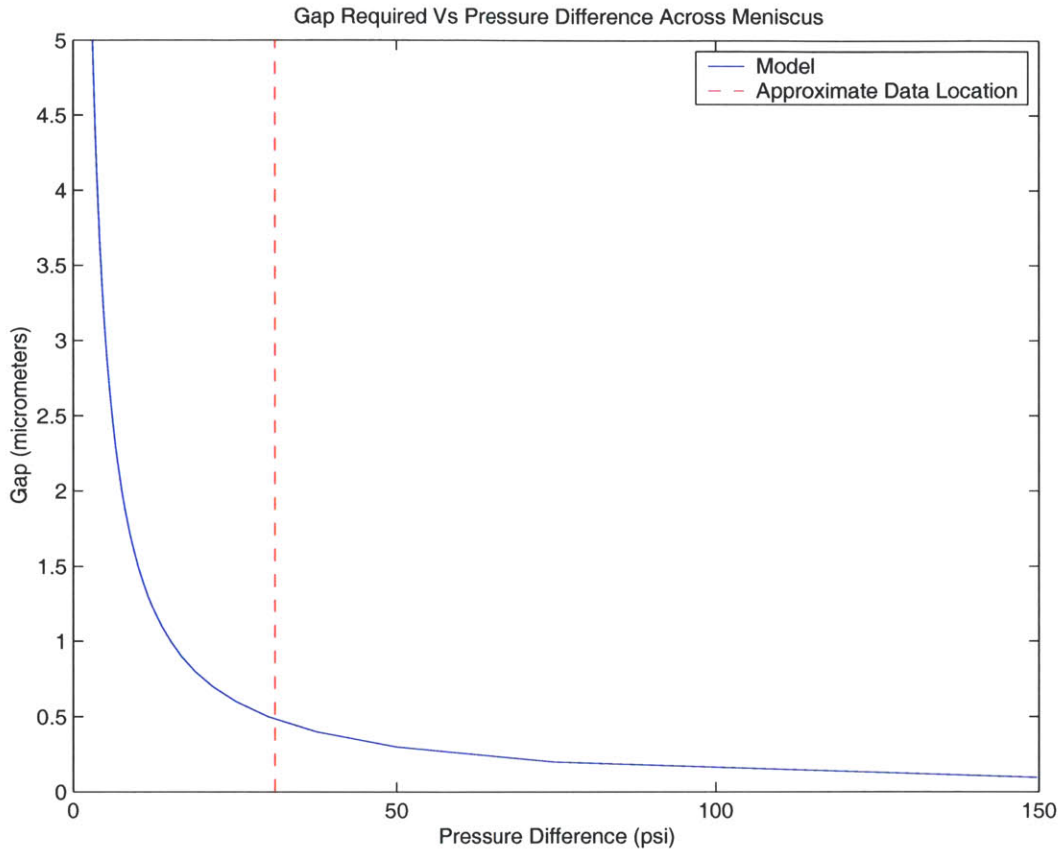

Figure 3-18: Plot indicating the gap required to maintain a meniscus in the forward thrust bearing as a function of the pressure difference across the meniscus.

Figure 3-18 indicates the gap required to maintain the meniscus as a function of the pressure difference across the meniscus. This assumes a constant 45 degree wetting angle. The model also assumes that the wetting angle is the same on both the top and bottom surfaces of the meniscus. As the pressure difference between the water and the nitrogen gets larger due to the pump outlet pressure increasing, the gap between the rotor and the bearing must decrease in order to maintain the meniscus between the water and the nitrogen. The dashed line indicates the approximate pressure difference for the data shown in Figure 3-16. The data location intersects near the corner of the model curve, indicating that the surface tension may need to be considered as a factor in the total force on the rotor. The next section will discuss possible instabilities that this phenomena could bring about.

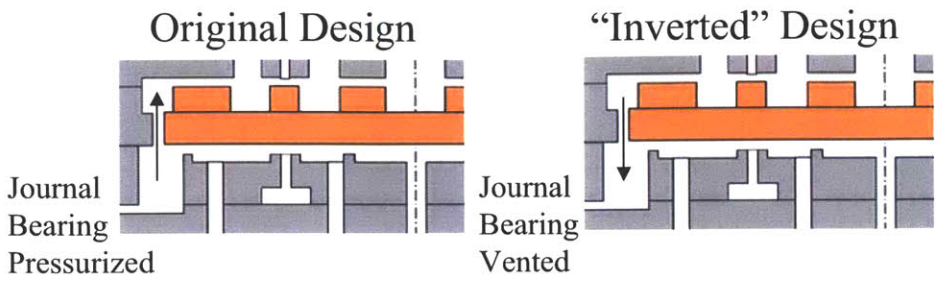

Figure 3-19: Comparison of normal operation and inverted operation for the journal bearing.

3.4.3 Raleigh-Taylor Instability

A classical Raleigh-Taylor instability occurs when a heavier fluid is supported by a lighter fluid, for example when a liquid is supported by a gas. Such a situation can be stable as long as the surface tension at the interface is large enough to compensate for the high potential energy of the heavier fluid. As suggested by Kerrebrock [8], a similar instability could exist in the micro turbopump at the interface between the pump exit and forward thrust bearing due to the centrifugal force field. The critical question is at what speed does the instability become too great for the surface tension to overcome, thus causing the seal between the pump and the turbine to break. Work by Jacobson [6] indicates that at a pressure of 50 PSI in the forward thrust bearing, the system will be stable up to a speed of 225,000 RPM. At this point, the thrust bearing pressure will need to be adjusted to maintain the seal. As speeds of 225,000 RPM have not been achieved in the demonstration micro turbopump, this has not been verified. Current testing is attempting to investigate the possibility of this instability in greater detail.

3.4.4 Journal Bearing Flow Direction

As designed, the journal bearing gas flows from the journal bearing plenum to the turbine inter row location as shown in Figure 3-19. It was seen experimentally that the system more easily stabilized at higher speeds if the journal bearing gas flowed in

the opposite direction. This is believed to be caused by the highly coupled system on the aft side, prior to the aft redesign. In this design, the journal bearing flow mixes with the aft thrust bearing flow near the inlet to the journal bearing. The influence of this flow changes the journal bearing pressure drop, but since the journal bearing pressure tap is inside the plenum, the instrumentation cannot read this pressure precisely. As discussed in Chapter 2, the success of the inverted journal bearing led to the the current aft bearing system design.

In order to realize this, a vent to the journal bearing port was installed. Instead of inserting pressurized air into the journal bearing plenum, a metering valve allows for controlled venting of air from the turbine inter row location to pass through the journal bearing. The reason for operating the journal bearing in this inverted fashion still needs more investigation.

3.5 Summary

The test rig for the demonstration micro turbopump has been described in detail. Different schemes for running the pump have been presented and discussed, and a partially balanced method has been suggested for future pursuits. The procedures developed for starting and operating the pump at low speed have been detailed. A number of difficulties have been found while attempting to operate the micro turbopump. These include the surface tension in the seals, the journal bearing flow direction effects, and the forward bearing pull in force. Some hypotheses for each have been presented. Future work needs to be done to fully understand these operational difficulties.

Chapter 4

Bearing and Seal Performance

For the demonstration micro turbopump, all of the bearing systems are hydrostatic, pressurized by an external gaseous nitrogen supply. This chapter will discuss the theory behind the hydrostatic journal bearing and hydrostatic thrust bearing systems and present the data obtained for these bearings and the aft seals in the micro turbopump.

4.1 Journal Bearing Performance

The hydrostatic journal bearing is a thin restrictor gap, which constitutes the bearing land, pressurized by a plenum built into layer 4. The restrictor gap is designed to have a straight profile, which is uniform around the periphery of the rotor.

4.1.1 Journal Bearing Theory

Extensive work on hydrostatic journal bearings has been completed by various members of the microengine project at MIT. Two issues pertaining to the bearing performance are the natural frequency of the journal bearing as well as its whirl instability boundary. The journal bearing acts like a spring-mass-damper system and the behavior and natural frequency are similar to a second order oscillator, thus $\omega_n = \sqrt{k/m}$ where k is the stiffness and m is the mass of the bearing. Due to imperfections in

fabrication, the mass center of the rotor is offset from the geometric center, leading to a static imbalance on the rotor of each micro turbopump. As the rotor accelerates, this causes it to feel a sideload. The imbalance drives the rotor to a synchronous precession around the geometric center of the rotor. The speed at which these precessions grow in an unstable manner is the whirl instability boundary for that given bearing and rotor imbalance [10].

Both the journal bearing natural frequency as well as the instability boundary have been analyzed and can be predicted by Liu's analytical model [10]. The hydrostatic direct stiffness, hydrodynamic cross stiffness, and the unsteady forces due to the damping force of the squeezed flow are taken into account in this model. The model assumes the flow can be represented as a combination of Couette flow and Poiseulle flow. Figure 4-1 shows an example of the predicted values of the natural frequency and instability boundary for various amounts of rotor imbalance for the original design specifications of a 300 micrometer long and 12 micrometer wide journal bearing at a radius of 3.1 millimeters with parallel sidewalls.

Since the current journal bearing system is hydrostatic, both the natural frequency and instability boundary can be predicted as a function of the pressure drop across the journal bearing. The pressure drop across the journal bearing can be set to allow the pump to operate away from the journal bearing natural frequency and instability boundary. The next section will discuss how this model was used to design the journal bearing gap for builds 5 and 6 of the turbopump.

The turbopump system is further complicated by the introduction of water into the pump blades. The higher density of the water (as compared to the nitrogen running the turbine) causes it to be a concern in terms of imbalance. If some of the water leaks through the seal, it acts as an additional point mass on the rotor, taking the center of mass further away from the geometric center. The density of water is 43% that of silicon. With this mass the water can have significant effects on the rotor mass properties. For the calculations in this thesis, the effects of imbalance caused by the water will be neglected unless specified otherwise.

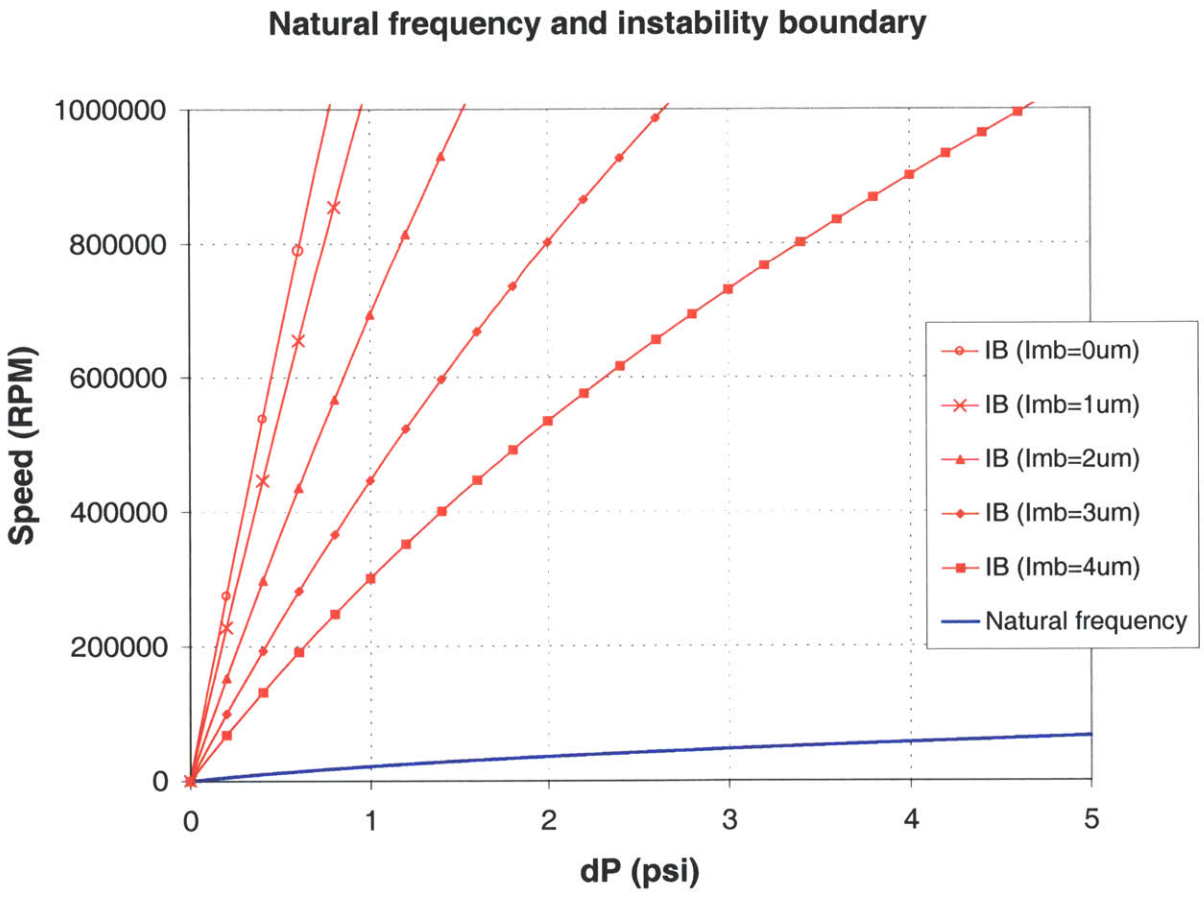

Figure 4-1: Example of natural frequency and instability boundary predictions for various levels of imbalance[11, 7].

4.1.2 Design Strategy

Since it is impossible to cross the whirl instability boundary, its value represents the maximum speed that the rotor can achieve at a given pressure difference across the journal bearing. Work by Liu suggests the existence of a singularity in the instability boundary for certain width journal bearings with a given static imbalance indicating that at these conditions, an infinite stability boundary would exist and thus infinite possible rotor speed [10]. The original design of the demonstration micro turbopump does not take any static imbalance into account, thus operation near this singularity is not likely. In order to make use of the theoretical singular behavior or the journal bearing, builds 5 and 6 have journal bearings cut at widths that were customized to achieve the highest possible speed.

First, the rotors are analyzed using a procedure introduced by Teo [16]. After the rotors have been etched, the etch variation is measured by comparing the etch depths at different circumferential points along a fixed radius of the rotor. The etch variation accounts for most of the static imbalance. The variation is used to determine the imbalance by creating a 3D model in AutoCAD with the indicated etch variation and calculating the mass properties of the resulting rotor. The additional imbalance caused by the journal bearing etch misalignment to the turbomachinery is ignored as the etch variation is the major contributor to the static imbalance [7]. Table 4.1 gives the measured etch variation and calculated imbalance for builds 5 and 6a.

Next, dummy journal bearings are cut to better understand the profile of the current fabrication process. Once the profile is determined, the length of the bearing can be inferred. The profile is important in determining this information. As can be seen by Figure 4-2, some journal bearings exhibit a wide opening on the forward side of the bearing. This changes the effective length of the restrictor. The wide opening is large enough that it does not cause an adequate restrictor here and thus reduces the effective bearing length. The length of the wide opening is subtracted from the total length of the bearing, which can be determined by subtracting the turbomachinery etch depth from the total wafer thickness. With this information

Table 4.1: Calculated Imbalance for Builds 5 and 6a.

Die	Calculated Imbalance (in micrometers)
5-1	1.22
5-2	1.08
5-3	0.1
5-4	0.51
5-5	1.33
6a-1	1.36
6a-2	2.18
6a-3	1.04
6a-4	2.45
6a-5	1.39

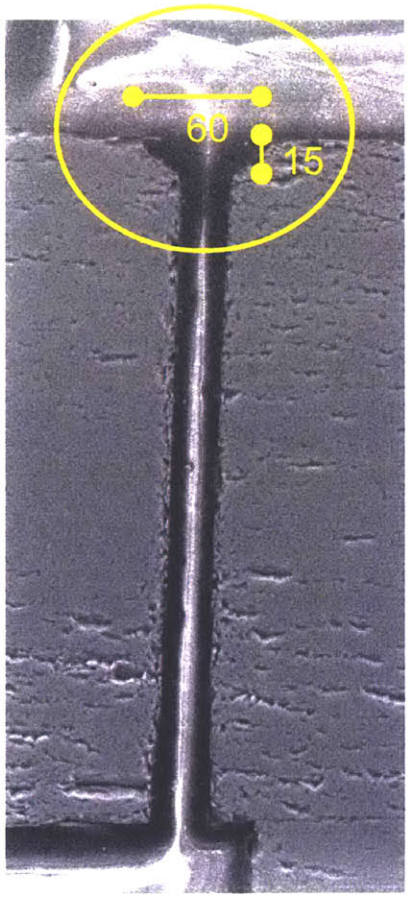

Figure 4-2: SEM picture of a journal bearing showing the blow-down effect on the forward side [12].

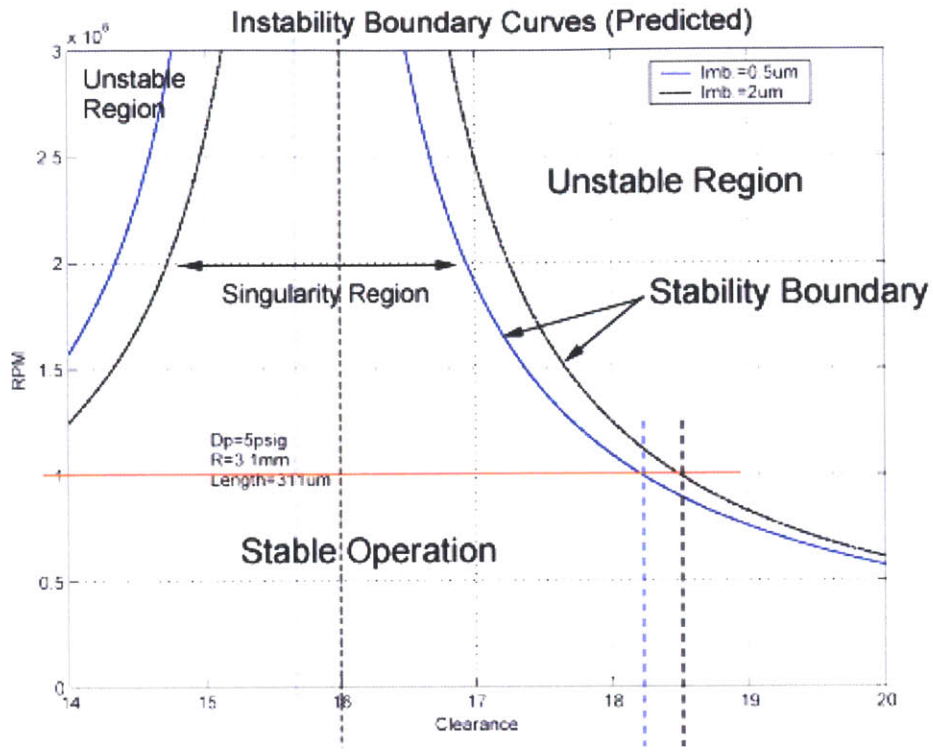

Figure 4-3: Instability curves and singularity region shown with vertical lines illustrating target widths for this case. [11, 12]

charts such as Figure 4-3 can be created using Liu's model.

The shape of the bearing has other implications as well. Common bearing shapes include tapered bearings as well as bearings that are wider in the center of the length than at the inlet and outlet. Calculations by Liu suggest that tapered bearings can be approximated as a straight bearing with the average width of the tapered bearing. Bearings with a wide center are more difficult to model and have generally been found to have poor performance [11].

Figure 4-3 shows the predicted singularity region of the bearing. Considering the required design speed and the imbalances of the rotors for a particular build, a bearing opening width can be read from the x axis of a graph such as Figure 4-3. With this width chosen, a mask is designed to produce this width bearing. By using this procedure, the effects of the static imbalance can be compensated for, creating devices that can spin up to design speed across a range of imbalances.

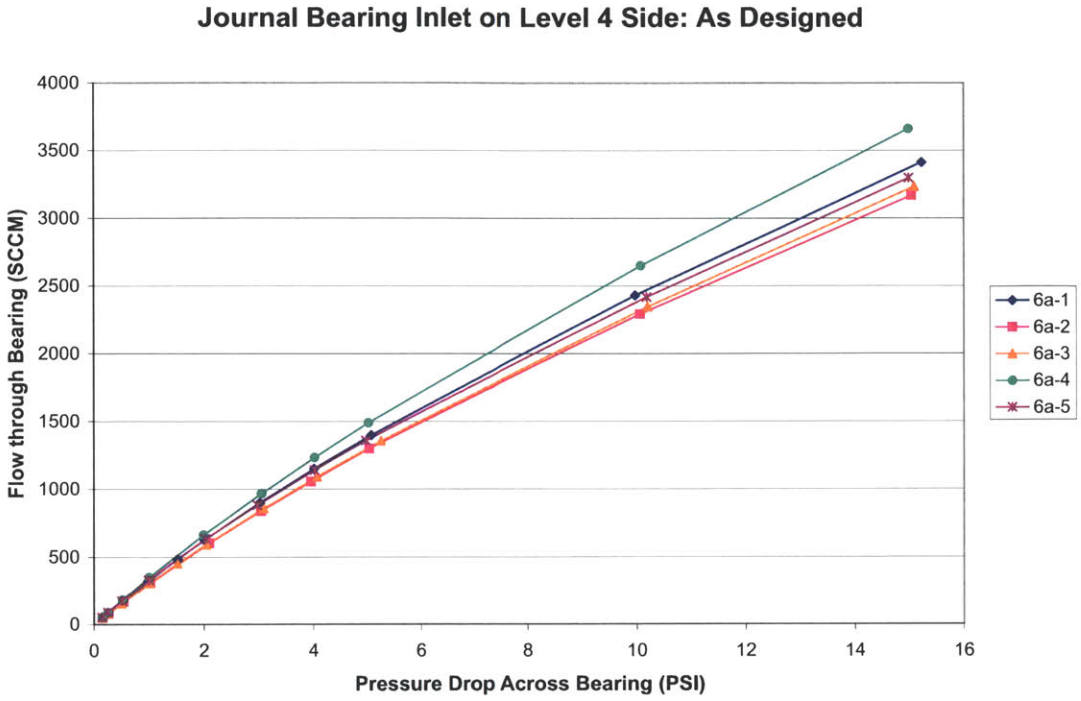

Figure 4-4: Static flow test data of the journal bearing if run as designed. Legend entry refers to die number.

4.1.3 Static Flow Tests

As discussed in Chapter 2, after the 5 silicon wafer stack is bonded and before the pyrex top wafer is anodically bonded, static flow tests are completed. Because the rotor is still held in place by a set of silicon oxide pads, it is exactly radially centered inside the journal bearing. This configuration allows for static testing with a known location.

Two types of static tests are completed for the journal bearing. As was discussed in Chapter 3, the journal bearing has been operated both as designed as well as with a throttled vent on the journal bearing plenum, thus leaking flow from the turbine and running in an inverted fashion. The wide opening on the forward side of the bearing causes a different inlet loss for the bearing if the flow is from the forward to the aft side rather than the opposite way as designed. Figures 4-4 and 4-5 plot data from static flow tests for the two schemes. Because the inlet loss, exit loss, and

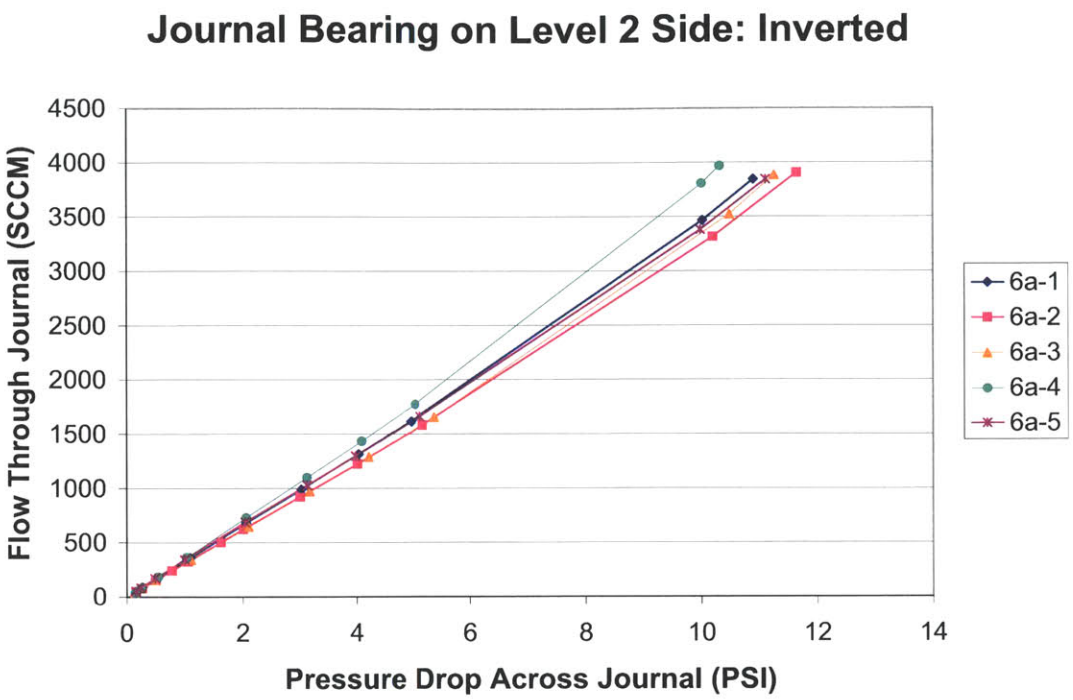

Figure 4-5: Static flow test data of the journal bearing if run inverted. Legend entry refers to die number.

flow profile create different pressure-flow relationships depending on the direction of the flow, there is a variation in the static test curves for the two tests. There is also a variation from die to die. This indicates that the journal bearing for each die may have a slightly different profile. These tests indicate that control over the shape of the journal bearing is critical. Studies into the journal bearing profile must take all geometric concerns into effect to ensure accuracy.

4.1.4 Rotordynamic Testing

Once the rotor is free, tests are run without water in the pump to find the natural frequency of the device. Since build 6a has an anisotropic bearing, two natural frequencies are expected. In order to find the natural frequency, the pumps are spun up to speed at a constant journal bearing pressure difference. When accelerating through a critical frequency, the increased eccentricity is characteristic of a decrease in the flow resistance at this location. Since the pressure difference is set for this test, the mass

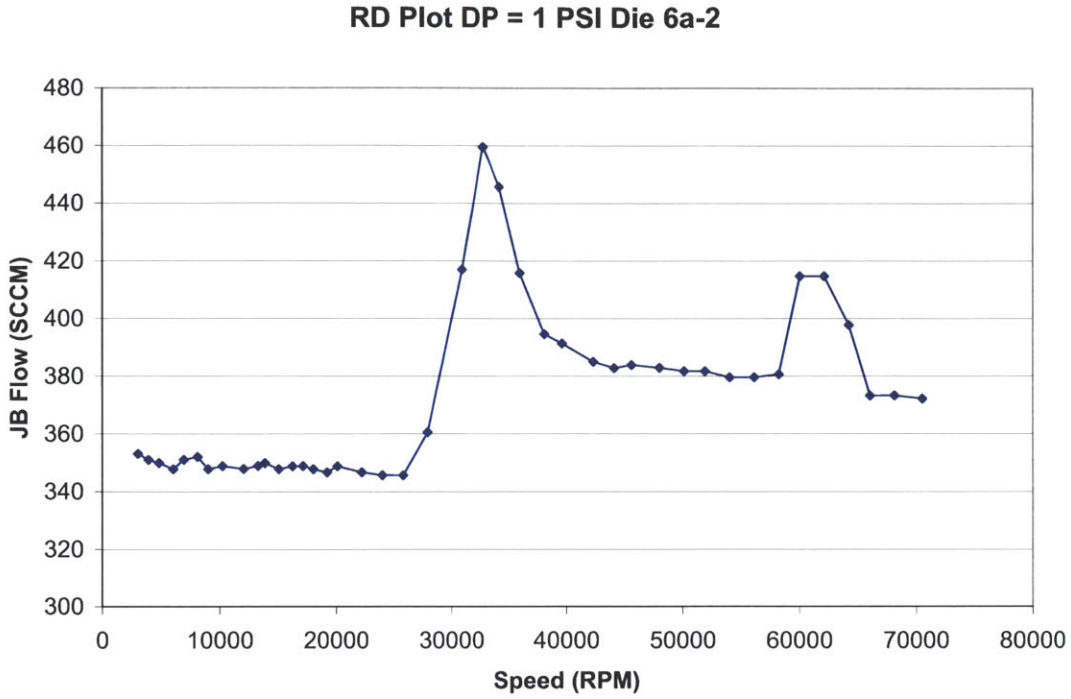

Figure 4-6: Rotordynamics plot showing natural frequency locations at approximately 30,000 and 60,000 RPM.

flow through the journal bearing increases near the natural frequency in response to the decreased flow resistance. The natural frequency can then be approximated by plotting the flow rate vs the speed of the rotor. This test is completed at a few different pressure differences and then the data is extrapolated to get an approximate value for the natural frequency across the full range of pressure differences.

Figure 4-6 shows one of the rotordynamic tests for die 6a-2. This plot indicates the existence of critical frequencies at speeds of approximately 30,000 and 60,000. Two critical frequencies are expected from this build due to the anisotropic journal bearing plenum. These predicted critical frequencies can be used as a guide when running pumping tests to ensure that the journal bearing is operated properly to allow for stable operation through these locations.

By acquiring high frequency speed and journal bearing mass flow data from these rotordynamic tests, the amplitude of the whirl of the rotor inside the journal bearing can be calculated by models written by Teo [10]. The steady state value of this whirl

Table 4.2: Calculated and Measured Imbalances [16].

Die	Calculated Imbalance (in micrometers)	Measured Imbalance (in microns)
6a-1	1.36	1.2 ±0.5
6a-2	2.18	1.8 ±0.5
6a-4	2.45	2.3 ±0.5

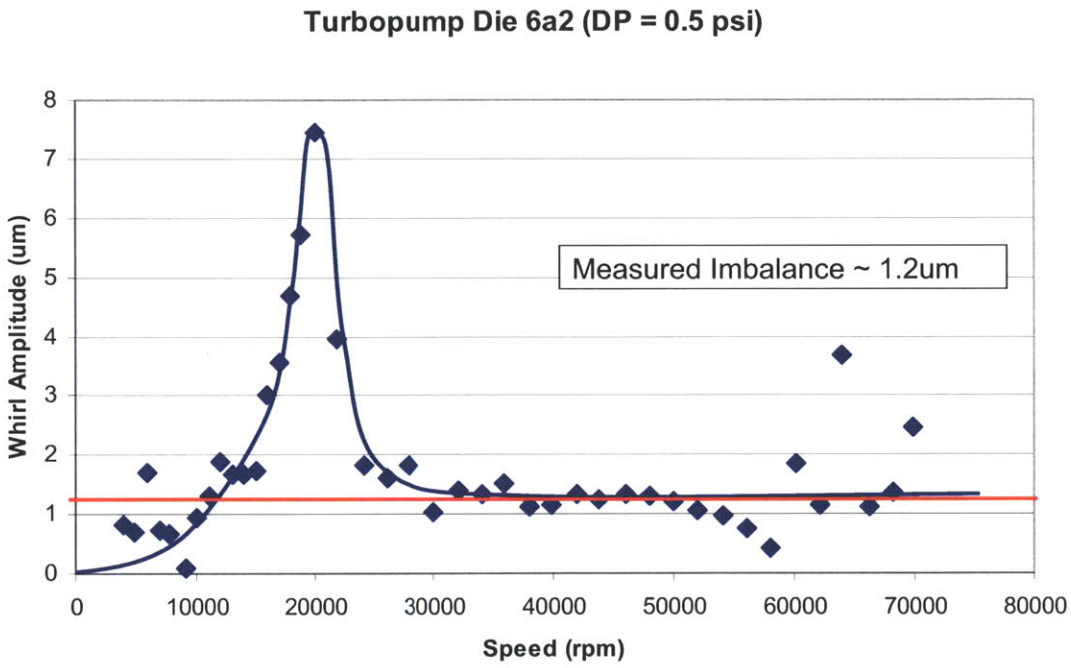

Figure 4-7: Rotordynamic data analyzed to give the whirl amplitude versus speed [16].

frequency is the dynamic imbalance. This imbalance as well as the predicted static imbalance as defined above is given for dies 6a-1, 6a-2, and 6a-4 in Table 4.2. A sample plot from this model showing how the imbalance is approximated is shown in Figure 4-7. The measured imbalance agrees well with the static imbalance, which validates the journal bearing design process.

Table 4.3: Thrust Bearing Specifications [2]

Location	Specified Dimension
Number of Injector Nozzles	60
Length of Injector Nozzles	100 micrometers
Diameter of Injector Nozzles	10 micrometers
Width of Annular Pad	400 micrometers
Total Thrust Bearing Gap	5 micrometers

4.2 Thrust Bearing Performance

In order to maintain axial stiffness, the demonstration micro turbopump has both a forward and an aft hydrostatic thrust bearing. These bearings each consist of a supply plenum, restrictor injector nozzles, and an annular bearing pad. In each case there are 60 restrictor nozzles, however on the forward side they are arranged in a slightly different pattern than the aft side. The thrust bearings on the forward side exhaust to the pump outlet and turbine outlet. The thrust bearings on the aft side exhaust to the lower plenum and journal bearing plenum in the original design and the two exhaust plena in the new design. The bearing specifications are summarized in Table 4.3.

4.2.1 Thrust Bearing Theory and Model

Before the redesign of the aft bearing system, a detailed model was created to model both thrust bearings as well as the interaction of the forward and aft bearings. The thrust bearing model is an incompressible model. The incompressible assumption limits the range in which the model is valid. At high pressures and high mass flows through the thrust bearings, the high mach number flows make the model invalid, therefore it can only be used to obtain accurate predictions at low thrust bearing pressures. The model assumes that most of the pressure loss in the bearing takes place in and around the injectors and bearing pad. Since the geometry of the individual nozzles is the same on each side, similar equations are used to describe these components. A sketch of the system is shown in Figure 4-8.

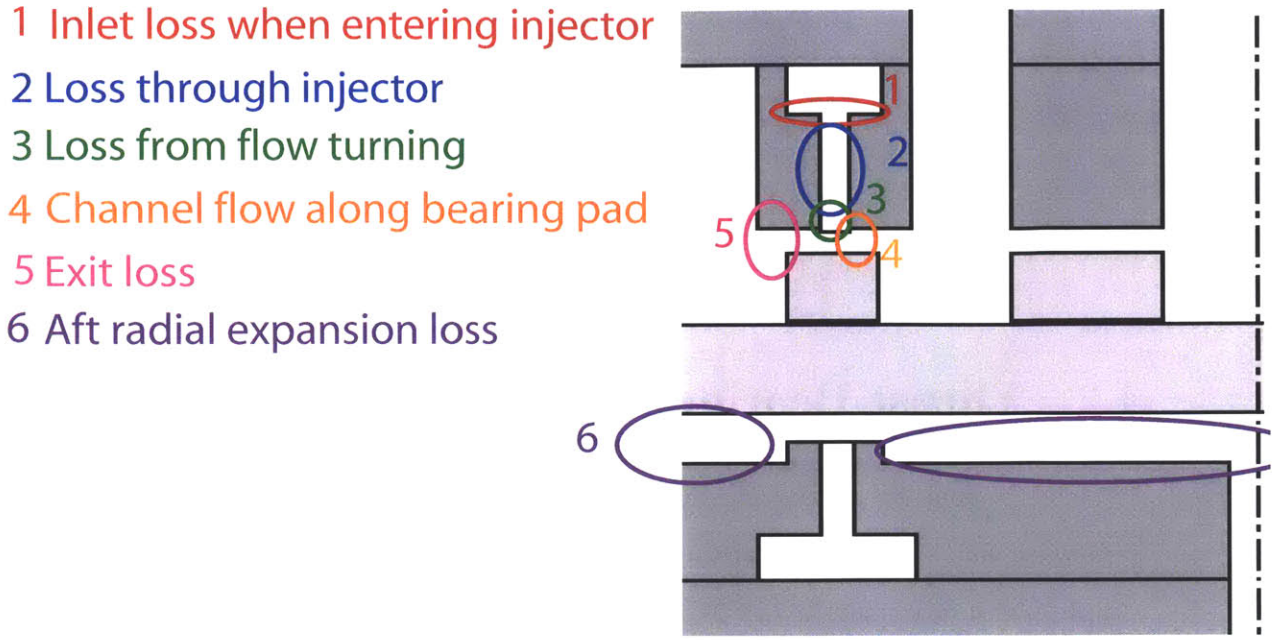

Figure 4-8: Illustration of losses taken into account in the thrust bearing model.

The total pressure loss caused by the flow entering the injector, shown as number 1 in Figure 4-8, is defined as

$$\Delta P_{tloss} = \gamma \frac{\rho}{2} \left(\frac{Q}{\pi R_{inj}^2} \right)^2 \tag{4.1}$$

where γ is chosen to be 1.5. The injector, shown as number 2 in Figure 4-8, is modelled as Poiseulle pipe flow. This can be described by

$$\frac{Q}{\pi R_{inj}^2} = -\frac{R_{inj}^2 \Delta P_{capillary}}{8 \mu L_{capillary}} \tag{4.2}$$

There is also a pressure loss as the flow turns when exiting the injector, which is labelled 3 in Figure 4-8. This loss was modeled by a CFD calculation done by Liu [11]. This loss is defined as

$$\Delta P_{loss} = \gamma \rho \left(\frac{Q}{\pi R_{inj}^2} \right)^2 \tag{4.3}$$

where γ can be defined as a function of the areas by

$$\gamma = 0.572 * \left(\frac{A_1}{A_2}\right)^{2.65}. \tag{4.4}$$

Equation 4.4 is a numerical fit to data obtained with a CFD model of similar thrust bearings. At the exit of the injector there is a pressure driven flow split. Along the annular bearing pad, the loss is modelled as Poiseulle channel flow along a rectangular slice of the pad, shown as 4 in Figure 4-8.

$$\frac{Q}{gap * w_{slice}} = -\frac{gap^2 \Delta P}{12 \mu R_{out}} \tag{4.5}$$

There is also an exit loss, show as 5 in Figure 4-8. This is modelled the same way as the inlet loss. For the aft bearing, there is the addition of the expansion flows that occur at the two locations shown as 6 in Figure 4-8. For these sections, the radial pressure difference is defined as [5]

$$\Delta P = \frac{6 Q \mu ln\left(\frac{r_{inner}}{r_{outer}}\right)}{gap^3 \pi}. \tag{4.6}$$

By rearranging the equations and inputing the pressures at the bearings, lower plenum, pump outlet, and turbine outlet, the model uses a Newton solver to find the flow rates through the bearings. These are then back substituted into the system of equations to get the intermediate pressures and integrated along the bearing area to get the total forces in the bearing system. The thrust bearing system stiffness is determined by looking at the force differential over a small axial perturbation.

Figure 4-9 shows the calculated flow rates for the new aft bearing design with all ports venting to atmospheric pressure. The data on the graph is from the one of the static tests, which will be discussed later in this chapter. Because this model only deals with incompressible flows, it is not valid at pressures above approximately 20 PSI as indicated by Figure 4-9. All model results will be shown for the pressure settings given in Table 4.4. This data point was chosen to indicate the approximate speed at the given thrust bearing pressures, which were chosen to accommodate the

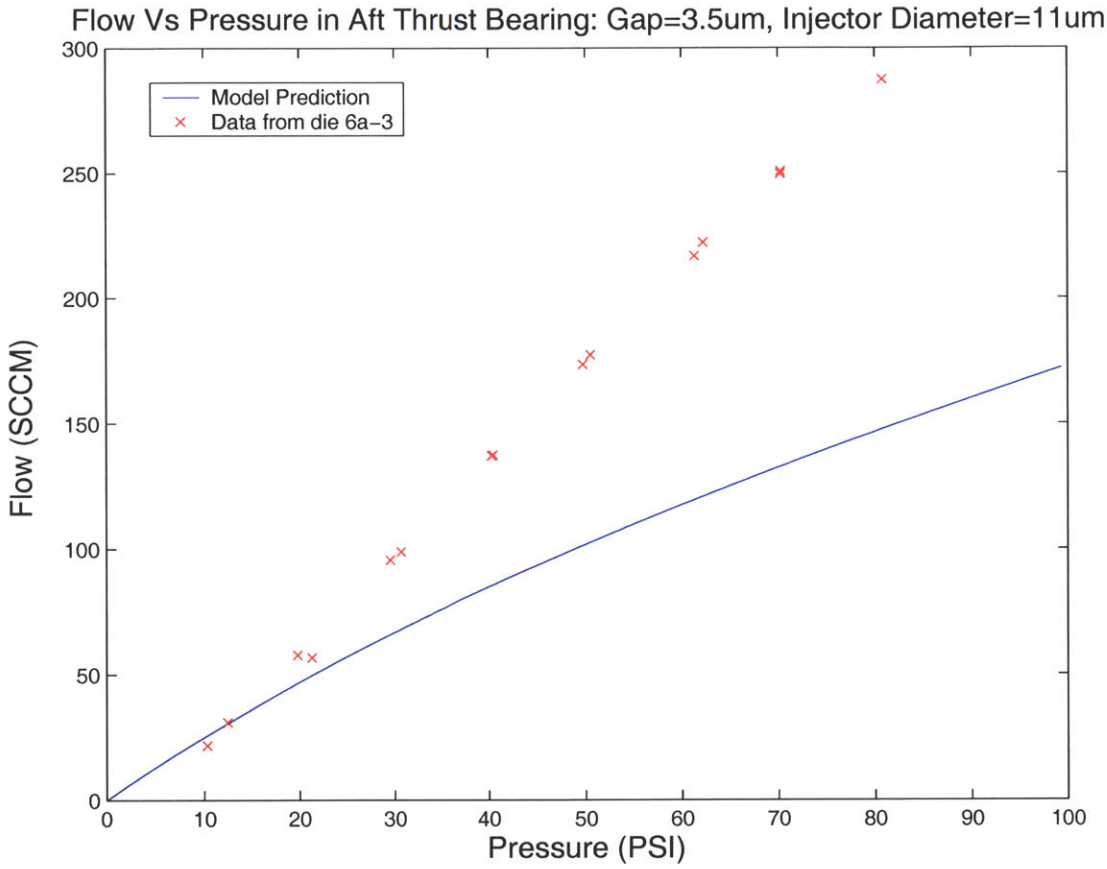

Figure 4-9: Comparison of calculated flow rate with experimental data for one bearing.

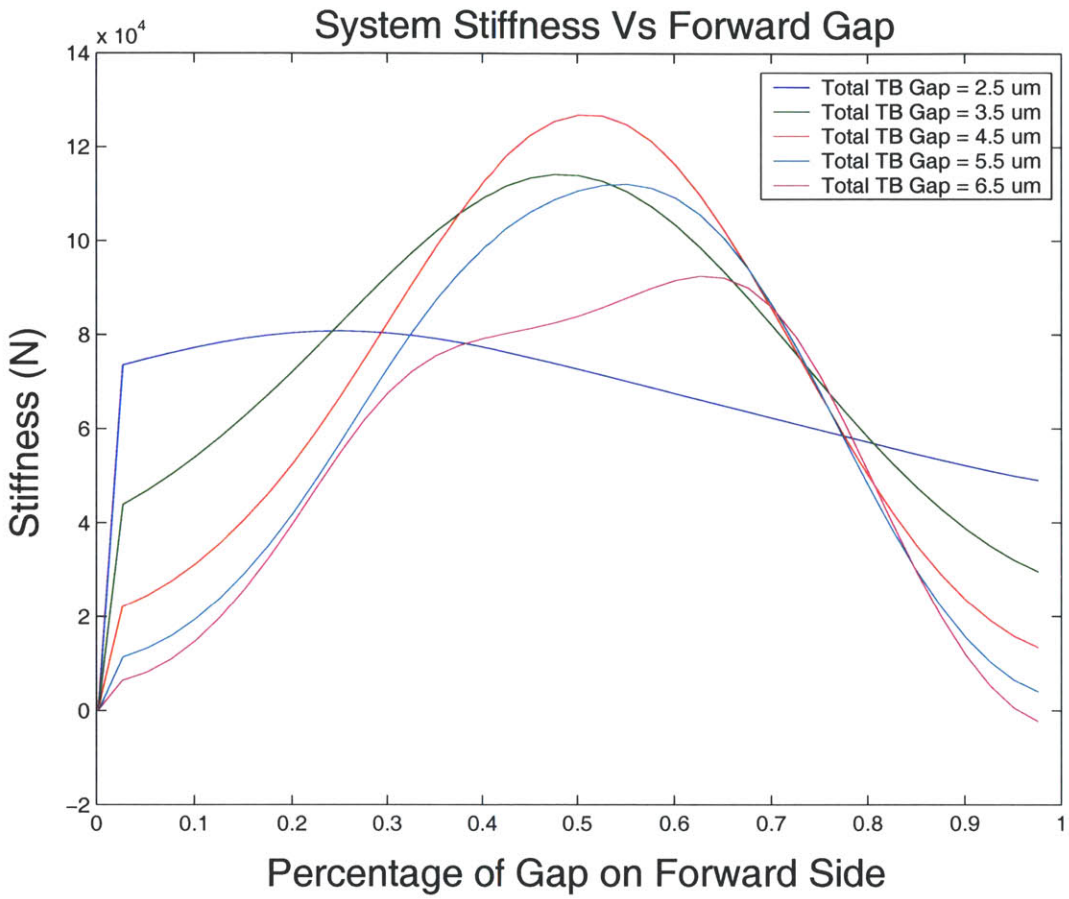

Figure 4-10: Stiffness for the bearing system for a variety of bearing gaps.

incompressible assumption of the model. Issues with the compressible flow inside the bearings and the effects of choking will be discussed later in this chapter. Figures 4-10 and 4-11 show the model result for the system stiffness and total bearing force for a range of the total thrust bearing gaps. All calculations shown are plotted against the percentage of the total gap that exists on the forward side. This is a measure of the axial rotor location. Therefore 0 on the x-axis indicates the rotor is stuck on the forward side and 1 indicates the rotor is stuck on the aft side.

The primary goal of this model is to determine the effect that out-of-spec parameters have on the system performance. Figures 4-10 and 4-11 indicate the degradation of the bearing performance as the total gap increases or decreases away from the 5 micron specification. Careful inspection of the total bearing gap is necessary to create pumps that will have thrust bearing systems capable of producing adequate stiffness.

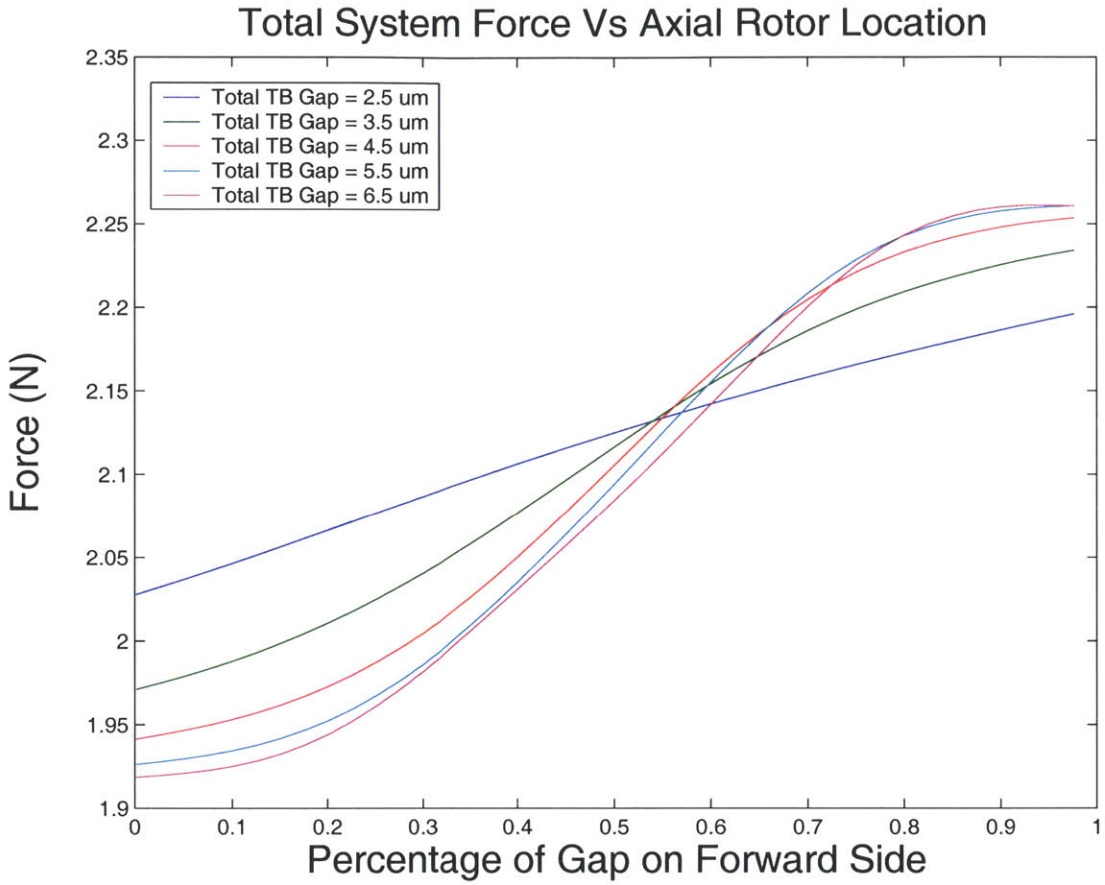

Figure 4-11: Total force on the rotor due to the bearings for a variety of bearing gaps.

Table 4.4: Model Point Used for Thrust Bearing Calculations Shown

Location	Gauge Pressure (PSI)
Thrust Bearings	20
Pump Outlet	17
Turbine Outlet	0
Lower Plenum	0
Journal Bearing	1.54

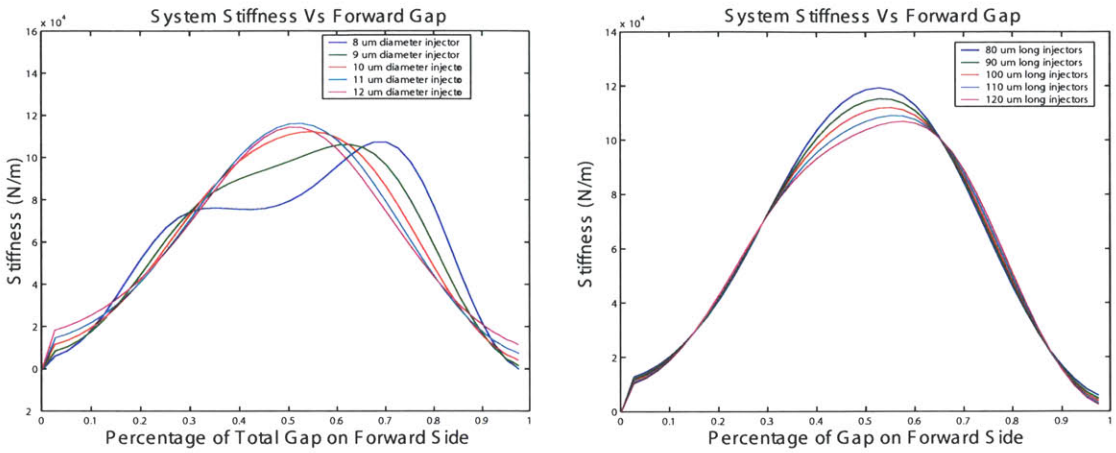

Figure 4-12: Bearing system stiffness as a function of location for varying injector diameters and injector lengths.

Figure 4-12 shows the effect that changing the nozzle hole diameter and injector length has on the bearing system performance. Figure 4-12 indicates that slightly longer or shorter injector lengths have little effect on the total stiffness. However if the diameter of the injectors is too small, the stiffness decreases. Undersize injector diameters also shift the maximum system stiffness to a non axially centered rotor location. For this reason the nozzle diameter is controlled more strictly than the nozzle injector length.

4.2.2 Static Flow Tests

Before the rotor is freed, static flow tests are completed on the aft thrust bearing. These tests are completed by pressurizing the bearing and venting the ports on either side of the bearing to atmospheric pressure. Figure 4-13 shows the data for the aft thrust bearing static tests of build 6a. Once the rotor is freed, similar tests are run with the forward thrust bearing. For these tests, the bearing gap is the full 5 micrometers. The static flow data allows the operator to have some indication of the axial location of the rotor during spin testing. For example, in Figure 4-13 the gap is fixed, and the axial location of the rotor is known. If, during a spin test, the operator can match the pressure to flow characteristics of a given die to the data shown, the

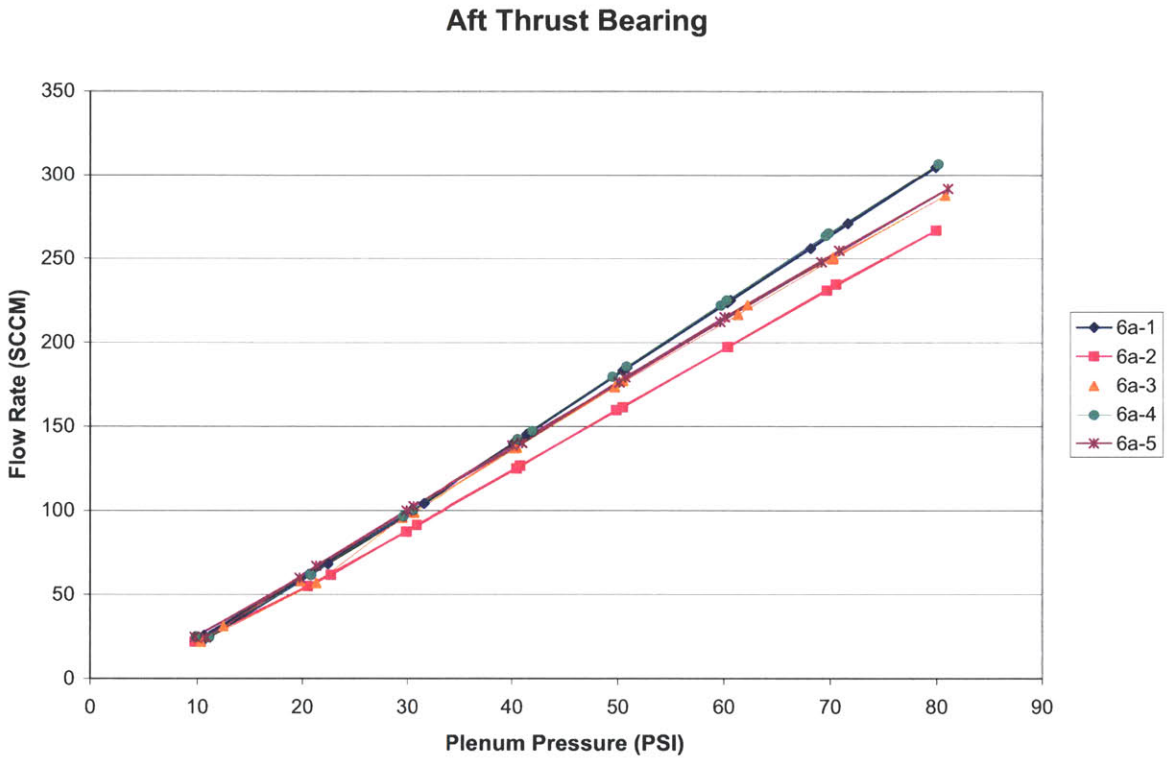

Figure 4-13: Aft thrust bearing static flow tests for build 6a. Legend entry refers to die number.

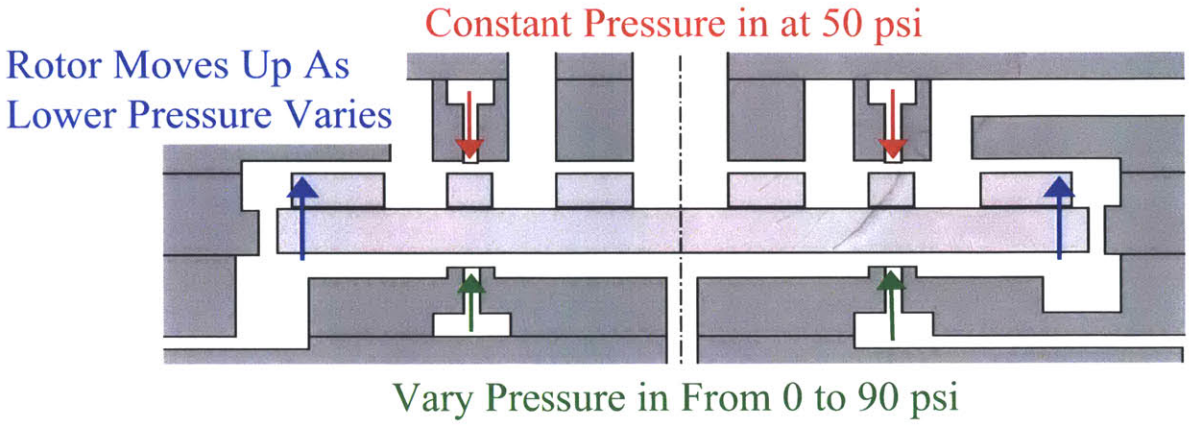

Figure 4-14: Illustration of the static thrust bearing response test.

operator can assume the rotor is in the same axial location as it was during the static flow test. If the flow is larger than shown at a given pressure, the aft gap is larger than it was during the static test and if the flow is smaller, the gap is smaller. Although this does not give an exact axial position, it gives some relative information to the rotor's axial location.

4.2.3 Thrust Bearing System Tests

In order to test the response of the bearing system the thrust bearing static response tests are completed. For these tests, one of the bearings is held at a constant pressure and the other bearing is pressurized in steps. The flow rate of the constant-pressure bearing is then plotted against the pressure in the variable-pressure bearing. The flow rate serves as an indicator of the axial location. Therefore, a flow rate of 0 indicates that the rotor is on the constant pressure side, and the maximum flow rate is approximately the flow rate when the rotor is on the variable pressure side. Figure 4-14 is a sketch showing an example of how a static thrust bearing response test is run with 50 PSI in the forward bearing and variable pressure in the aft.

A good response curve would be indicated by a bearing that closes off completely and has a steep transition slope. Figure 4-15 shows the results of a static thrust bearing response test for build 6a. This build indicated some existence of a response

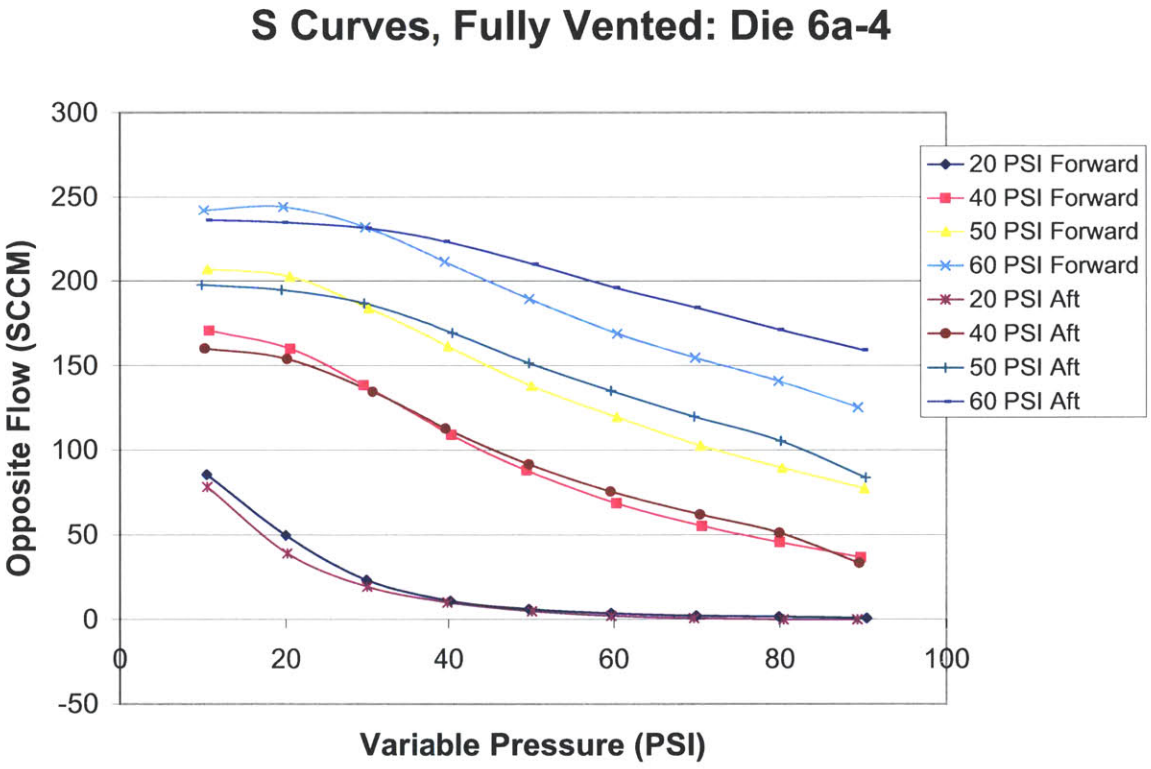

Figure 4-15: Static thrust bearing response tests for die 6a-4 at a variety of constant pressures. The pressure indicated in the legend is the pressure held constant for the test.

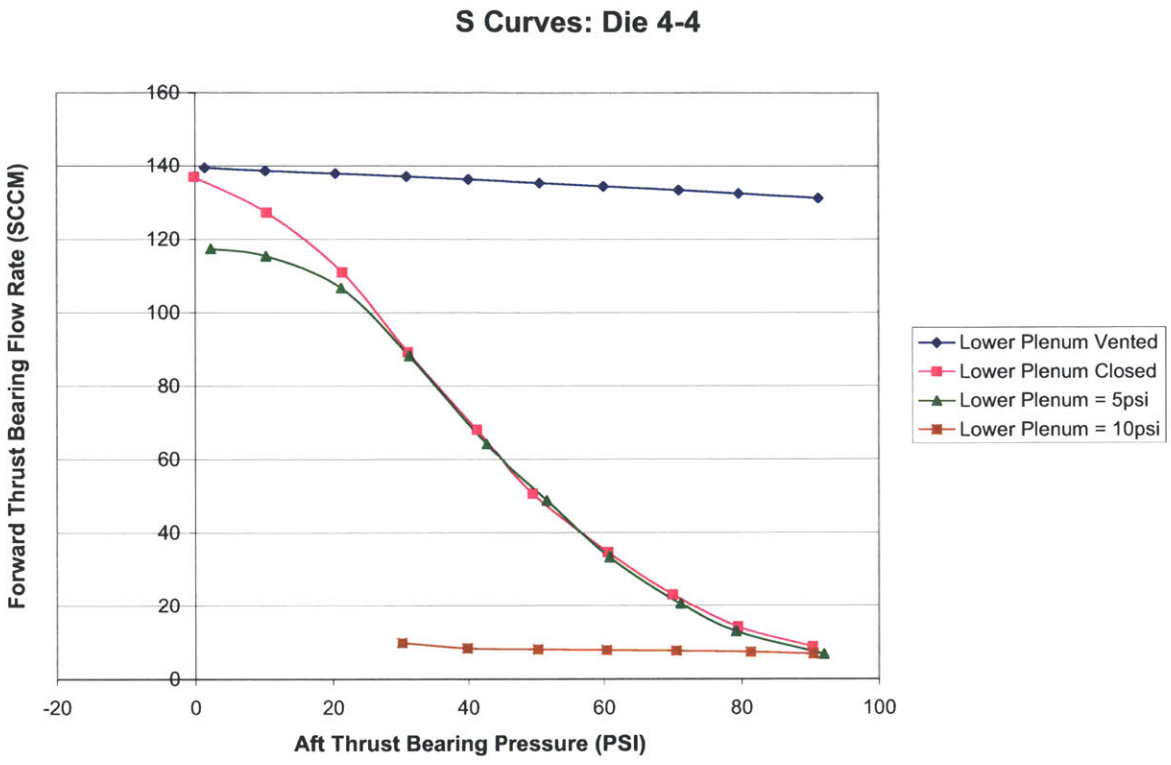

Figure 4-16: Static thrust bearing response tests for die 4-4 at a variety of lower plenum pressures.

curve, but the bearings were not able to be closed off except at low bearing pressures. A steep response indicates that for a small change in pressure on one side, there is a large change in the flow on the opposite side. An increase in the flow is proportional to an increase in the pressure change across the bearing pad. If the rotor moves very close to one of the bearing pads and the flow here is restricted, the the pressure loss on the bearing pad is decreased and thus the total pressure force on the bearing pad increased. Therefore a steep response means that as the rotor moves to one side, there is a stronger restoring force to bring the rotor back to an axially centered position.

Historically, the thrust bearings for the turbopump have had difficulty demonstrating a steep transition. As can be seen in Figure 4-16, the only way good response could be induced prior to build 6 was to increase the lower plenum pressure. This increases the total force on the aft side of the rotor during the tests. The bearings appear stiffer because the larger applied force compensates for the lack of response.

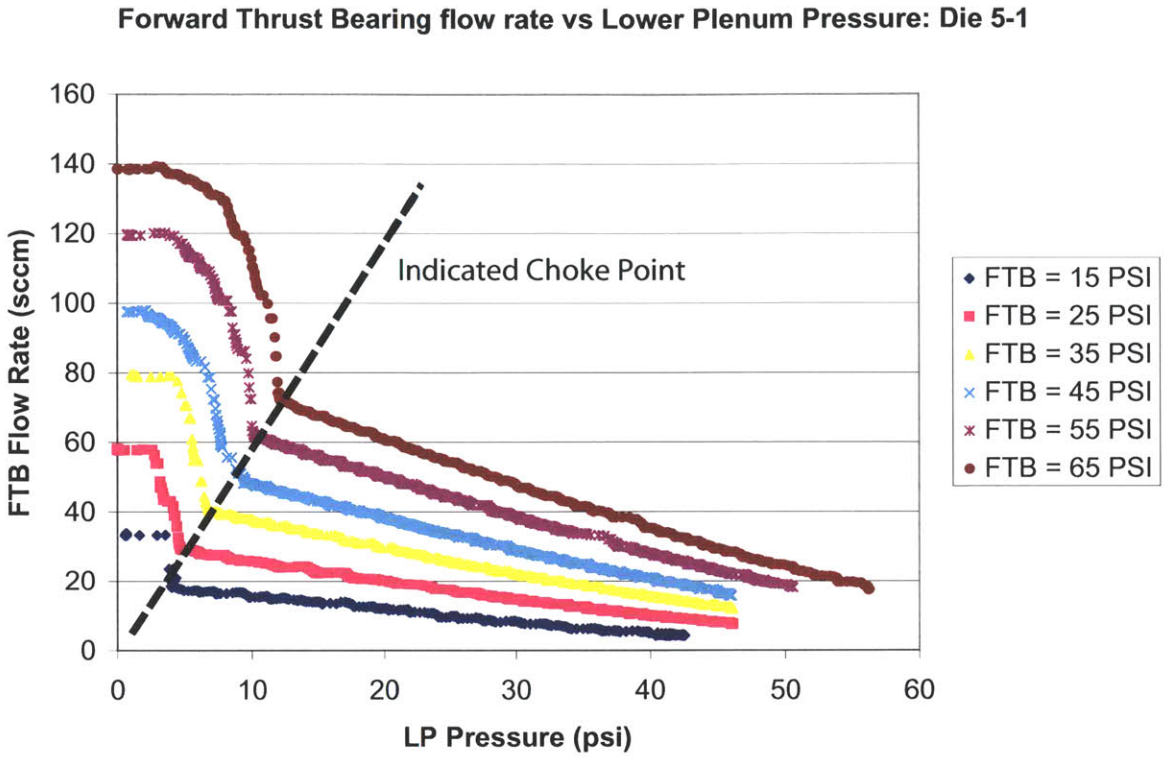

Figure 4-17: Experimental test to illustrate the effects of choking in the thrust bearings.

The next section will discuss the possibilities of choking in the thrust bearing systems and the implications this may have on these response curves.

4.2.4 Effect of Choking in the Thrust Bearing Injectors

While developing the thrust bearing model, indications of the choked flow inside the injector nozzles was seen in testing. Figure 4-17 shows a test that was done to demonstrate the effects that choked bearings have on the bearing response. This test was run by setting the forward thrust bearing pressure and then changing the lower plenum pressure. The bearing flow rate is plotted against the lower plenum pressure.

At a certain point, depending on the forward bearing pressure, the response curve begins to vary linearly with the lower plenum pressure. Choking occurs when the

corrected mass flow becomes a constant value. The corrected mass flow can be defined as

$$\dot{m}_{corrected} = \frac{\dot{m}\sqrt{T_t}}{P_t A} \tag{4.7}$$

Assuming the temperature, pressure, and gas properties are constant for each data line shown, the data points to the right of the dashed line indicate an inverse relationship with the cross sectional area, which is changing as a result of the varying lower plenum pressure. Therefore, the corrected mass flow becomes constant at this point in each test, indicating the choke point. After the choke point the flow responds to changes in axial position in a linear fashion, accounting for the change in the cross sectional area of the flow. Thus, once the bearings choke they have a fixed response, making a steep response curve impossible. This partially explains the historical difficulties with the thrust bearing static response tests discussed above.

Studies done by Teo [16] indicate that the bearing system will be stable if one of the bearings chokes but unstable if both bearings choke. In order to maintain axial balance, similar pressures in the two bearings are desirable. Therefore, it was decided that the bearings should be run at the lowest possible pressure to avoid choking. Care must also be taken when running very close to one of the thrust bearing pads as crossing into a region of choked flow is likely.

4.3 Seals

The addition of the two seals on the aft side of the device allows for two other sources of data pertaining to the axial location. By monitoring the flow that crosses the seals, some indication of how close the rotor is to the seals can be obtained. For this reason, static flow tests of the seals were performed. This also gives an opportunity to compare the data to the model used to design the seals.

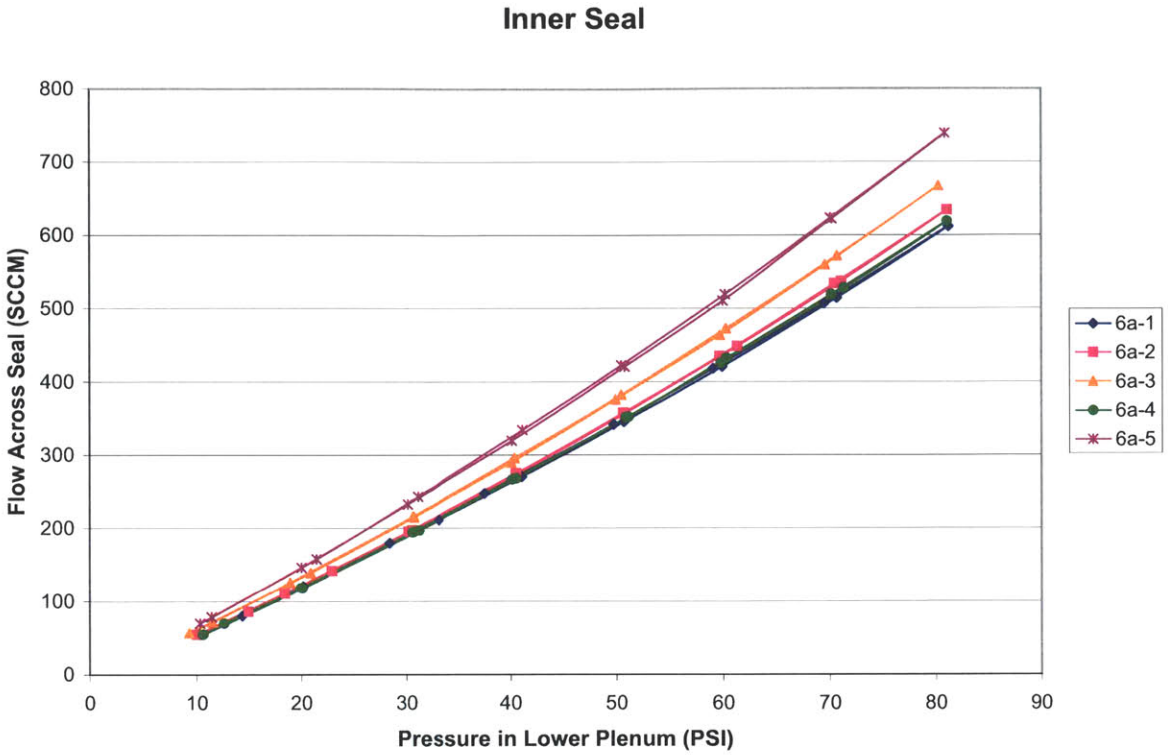

Figure 4-18: Static flow tests for the inner seals of build 6a. Legend entry refers to die number.

4.3.1 Static Flow Tests

The static flow tests were designed to allow data to be collected pertaining to the flow rate and pressure on each side of the seal. In each case, the experiment was set up to collect enough data to characterize the seal and make a comparison to the model.

Inner Seal Tests

For the inner seal static flow tests, the lower plenum was pressurized while the inner plenum was vented to atmospheric pressure. Since all the flow that goes through the lower plenum will also go through the seal, and the pressure both before and after the seal is known, the seal can be characterized. Figure 4-18 is a summary of the static tests completed on build 6a.

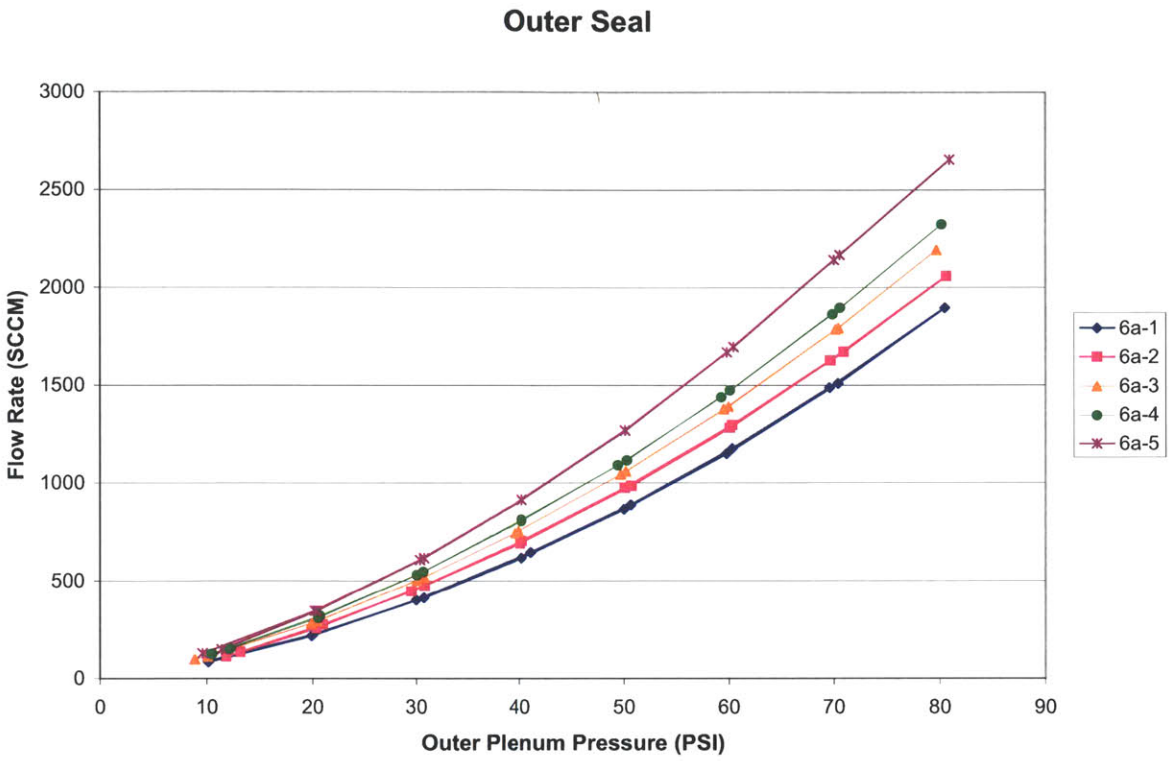

Figure 4-19: Static flow tests for the outer seals of build 6a. Legend entry refers to die number.

Outer Seal Tests

A similar test was completed on the outer seal. For this test, the outer plenum was pressurized while the journal bearing plenum was left open to atmospheric pressure. Figure 4-19 is a summary of these static tests completed on build 6a.

Conclusions

The differences in the seal pressure to flow response can be explained by small etch variations during the fabrication process. Since the outer seal has a larger cross sectional area, the larger flow rate through the outer seal is behaving as expected. The next section will compare this data to the original seal model.

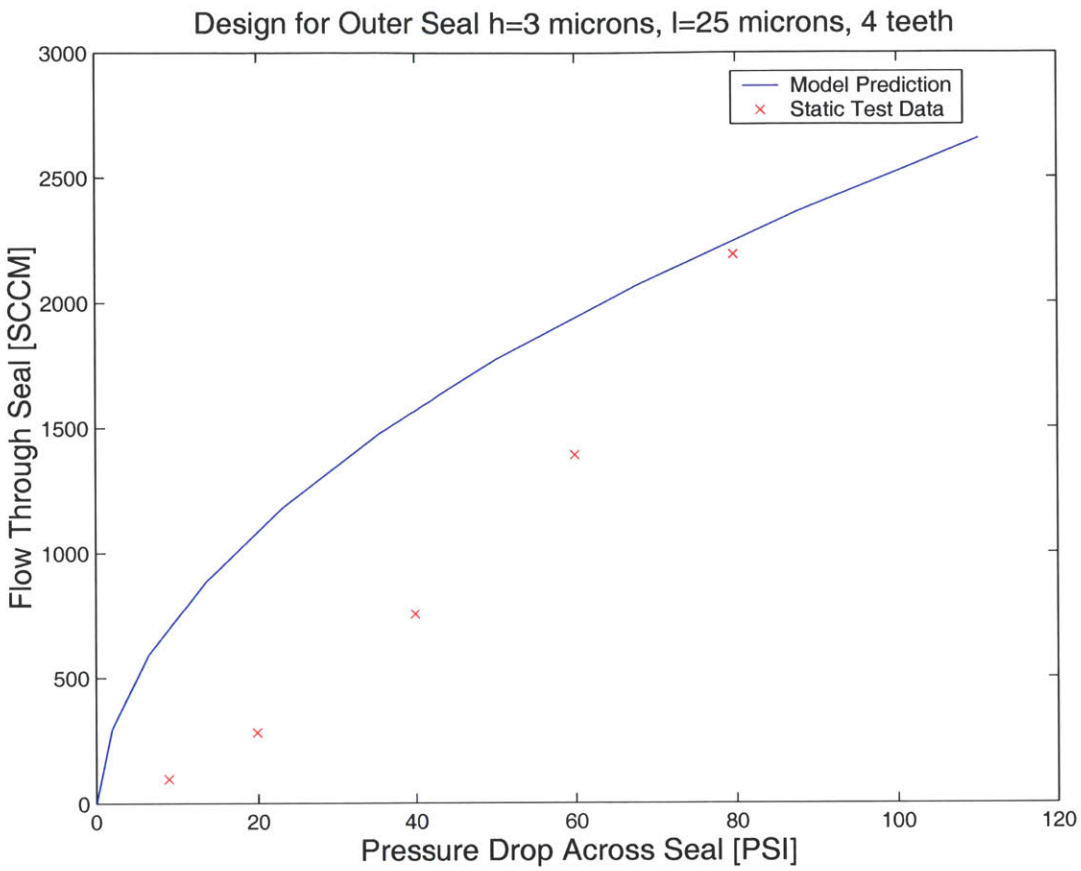

Figure 4-20: Comparison of predicted and experimental data for the outer seal.

4.3.2 Adjustment to Seal Model

Figure 4-20 shows the original prediction for the behavior of the outer seal as discussed in Chapter 2 with the data collected for die 6a-3 in the static flow tests. Figure 4-20 illustrates the high velocities seen in the seals, showing the need for compressibility effects in the model. Assuming an isothermal perfect gas model, the density can be defined as

$$\rho = \frac{P}{RT}. \tag{4.8}$$

Taking this into account in the original seal design model as discussed in Chapter 2, and adjusting the density as a function of pressure, Figure 4-22 was produced to more closely match the data. Since this assumption only partially accounts for the compressibility effects, the model still has difficulty predicting the data at high

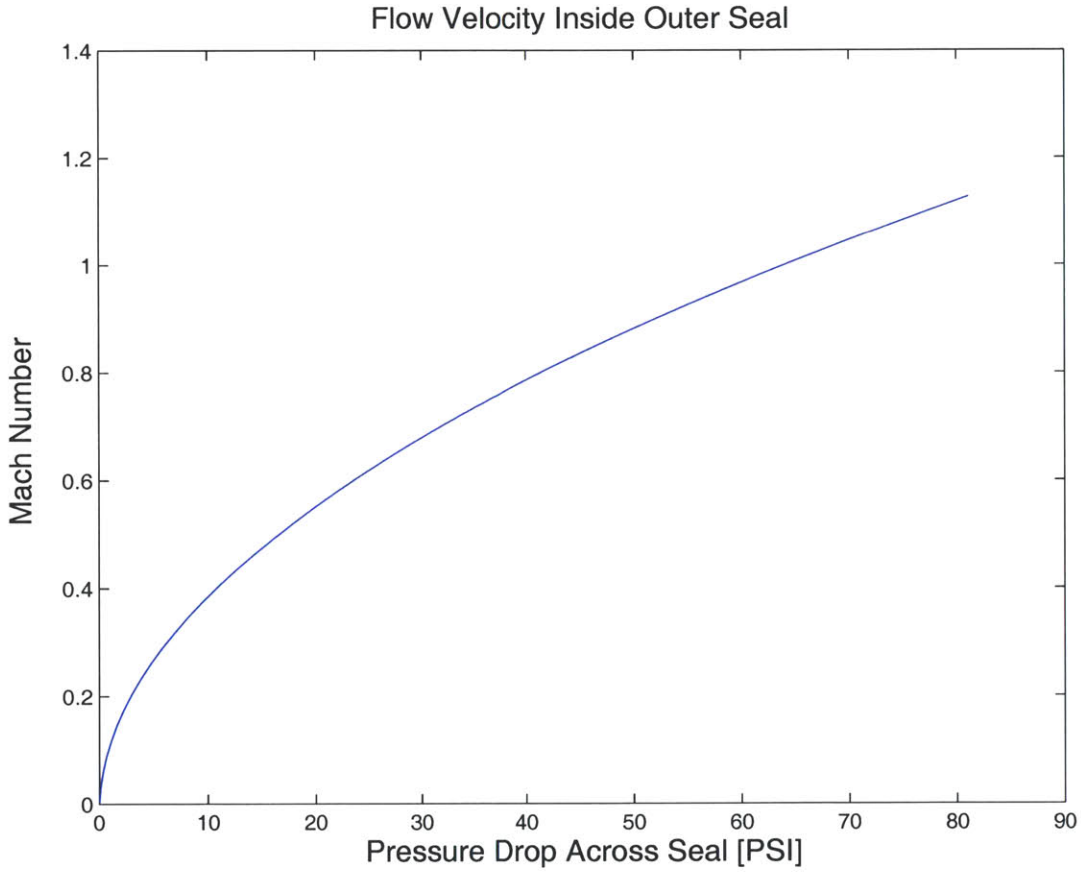

Figure 4-21: Predicted velocity inside the outer seal.

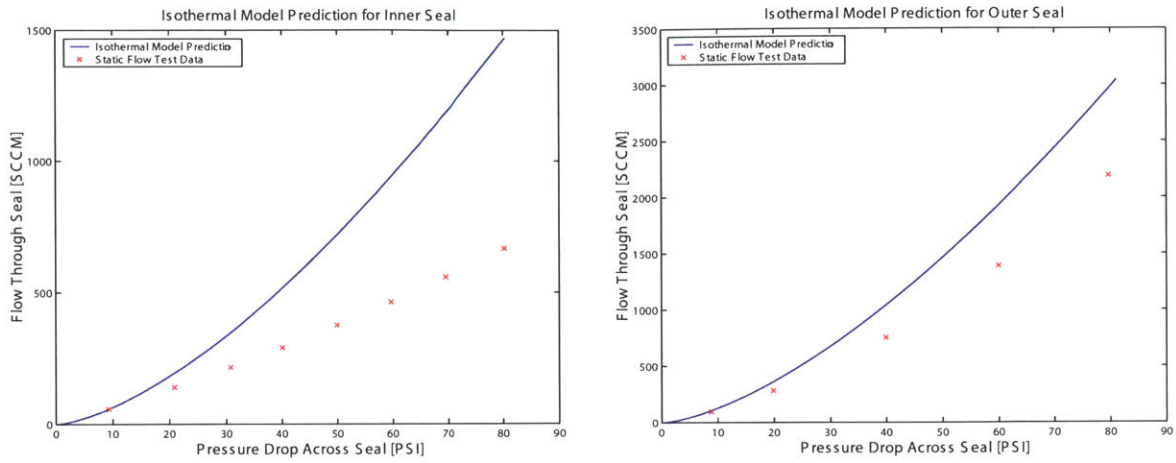

Figure 4-22: Corrected inner and outer seal flow prediction with experimental data comparison.

flow rates and flow velocities. Since the inner seal has a much smaller cross sectional area than the outer seal, the flow velocities at this location are larger than those in the outer seal. For this reason, the inner seal predictions are not as accurate as the outer seal predictions. With the partial compressibility effects, the model is able to predict the correct trend, however for precise quantitative predictions, a fully iterative compressible model is needed.

4.4 Summary

The bearings for the demonstration micro turbopump have been studied and data has been collected for static tests, rotordynamic tests, and static thrust bearing response tests. The journal bearing width for the demonstration micro turbopump has been optimized based on an analytical model. This allows the fabrication team to offset the measured static imbalance of the rotor. A thrust bearing model is discussed and some of the results shown indicating the importance of strict fabrication tolerances on the nozzle injector diameters and total bearing gap. Some of the difficulties specifically pertaining to the thrust bearings have been addressed. The choking inside the thrust bearings is of concern to the system stiffness and stability and choking should be

avoided if possible. The seals have been re-analyzed and compared to experimental data results. It is important to take compressibility effects into consideration when modeling these seals.

Chapter 5

Turbomachinery Performance

This chapter discusses the pump and the turbine components of the demonstration micro turbopump. It gives a brief overview of the design of the turbomachinery and then discusses the preliminary pumping data obtained for the demonstration micro turbopump.

5.1 Turbomachinery Theory

The demonstration micro turbopump is designed with the turbine and pump on the same side of the rotor for reasons discussed in Chapter 2. This section will briefly discuss the theory used to design the turbomachinery.

5.1.1 Design Overview

The pump and turbine blades for the demonstration micro turbopump were designed by Youngren [17]. More detail on the design of the blades can be found in Jamonet and Deux [2, 7]. The calculations were completed in MISES, a quasi 3D CFD code. The pump blades were further studied by Jamonet [7] and more information on their design can be found in his thesis.

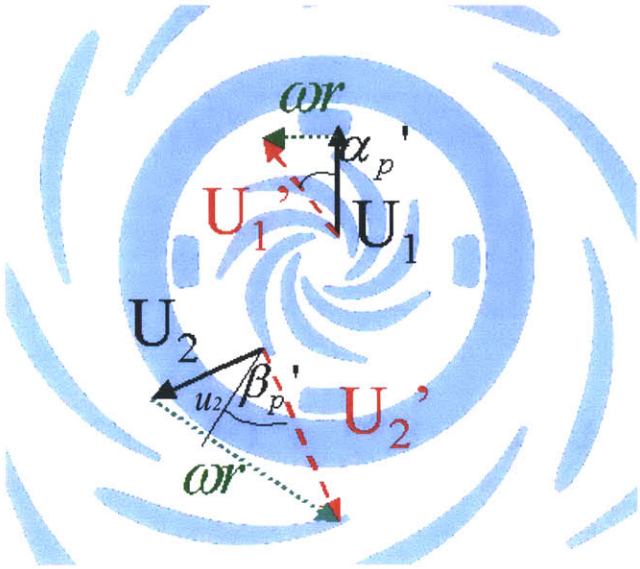

Figure 5-1: Velocity triangles for the pump blades. Solid black lines indicate the absolute velocity, thick dotted red lines indicate the relative velocity, and fine dotted green lines indicate the velocity of the rotor.

5.1.2 Velocity Triangles

For centrifugal pumps and turbines the torque, required or output, can be defined as the net change of angular momentum, and the work rate is the torque multiplied by the angular velocity ω. Thus, the blades are designed to require or produce a specific amount of power based on the change in the tangential velocity of the flow imposed by the blades.

Figure 5-1 shows the velocity triangles for the pump blades. The geometry of the demonstration micro turbopump does not allow for a diffuser. For this configuration, the ideal pumping power can be defined as

$$\mathcal{P}_{ideal} = \dot{m}(\omega r_{outer})^2(1 - \frac{u_2 tan\beta'_p}{\omega r_{outer}}) \tag{5.1}$$

Figure 5-2 shows the velocity triangles for the turbine blades. In this configuration, the ideal turbine power can be defined as

$$\mathcal{P}_{turb} = \dot{m}\omega r_{inlet}(V_2 sin(\alpha_t)) - \dot{m}\omega r_{outlet}(\omega r - V'_3 sin(\beta'_t)) \tag{5.2}$$

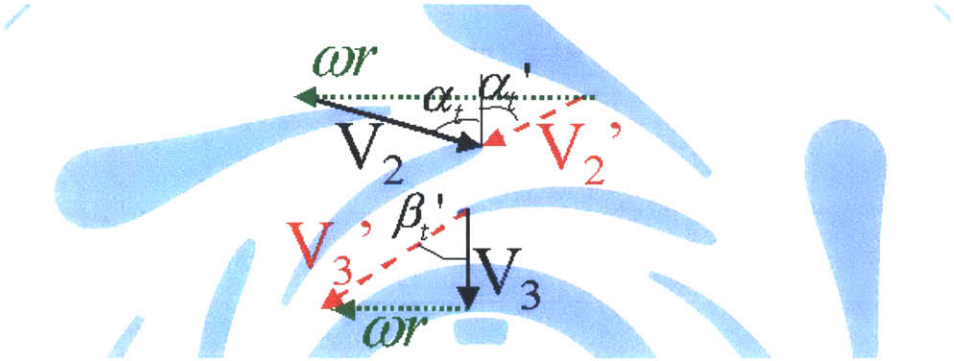

Figure 5-2: Velocity triangles for the turbine blades. Solid black lines indicate the absolute velocity, thick dotted red lines indicate the relative velocity, and fine dotted green lines indicate the velocity of the rotor.

In Figure 5-2 V_3 is shown to be exiting the rotating turbine blades with zero swirl. This is an example case and the actual exit swirl will vary depending on the rotor speed. These equations assume that the flow follows the blade trailing edge and exits tangential to the previous blade row, in the relative frame.

5.1.3 Designed Power Balance

Assuming an efficiency of 30% for both the pump and the turbine [2], the pump requires 36 Watts of power at full speed and the turbine delivers 50 Watts of power at full speed. The additional power margin accounts for losses in the system, mainly viscous losses in the bearings. The power balance was also calculated at 50,000 and 190,000 RPM as discussed by Deux [2]. These numbers can be found in Table 2.1.

5.2 Pump Performance

Successful pumping tests were performed up to speeds of 114,000 RPM. At this speed, the pressure rise and pumping power can be studied to determine the preliminary performance of the device.

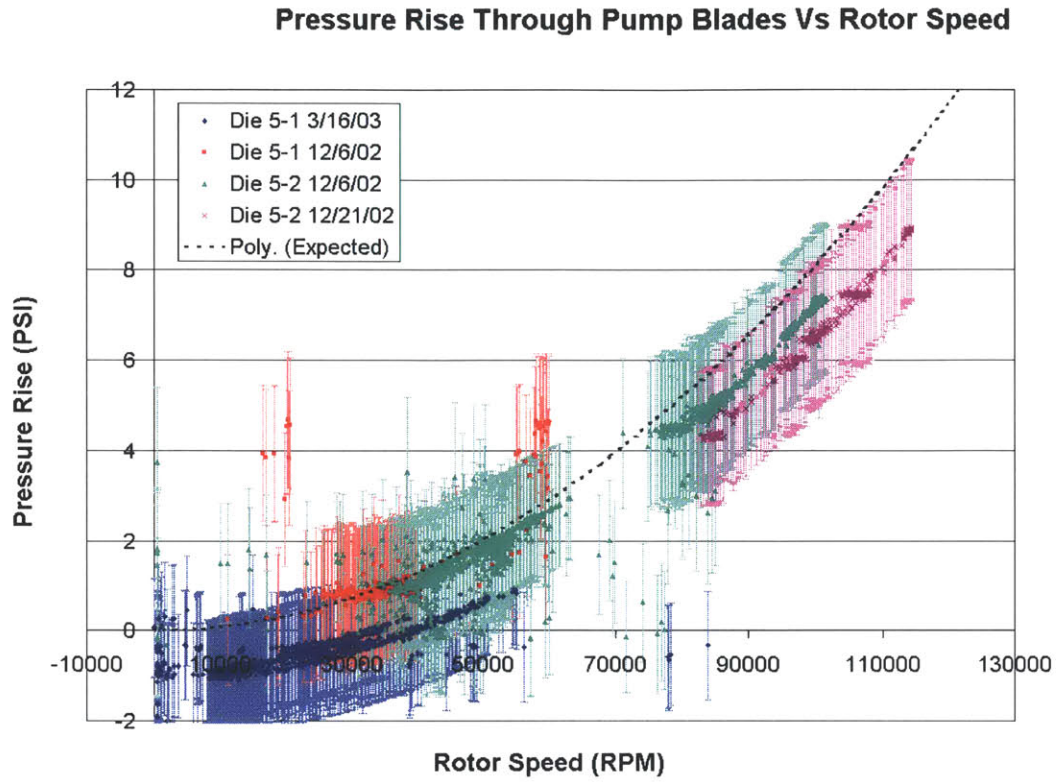

Figure 5-3: Isentropic pump pressure rise as a function of rotational speed.

5.2.1 Pressure Rise

In a centrifugal turbopump, the pressure rise through the blades should vary as

$$\Delta P = \rho(r_{outer}\omega)^2 \left[1 - \frac{u_2}{r_{outer}\omega} tan\beta'_p\right] \tag{5.3}$$

where r_{outer} is the radius of the pump, ω the angular velocity, u_2 the radial velocity at the exit of the pump, and β'_p is the exit swirl angle [2]. The exit swirl angle can be obtained from the geometry of the blades to be 58 degrees. The radial velocity can be obtained at a given speed from the mass flow through the pump. This indicates that the pressure rise should go as the square of rotational speed, ω.

Figure 5-3 shows the pump pressure rise as a function of the speed of the rotor. The expected pressure rise as predicted by Equation 5.3 is also shown. The positive pressure rise shown proves that pumping liquids on the microscale using turbomachin-

ery is possible. This data was gathered over 3 different days, with 2 different pumps, at varying pump throttle settings. The throttle settings affect the power balance and thus the pressure rise. For example, increasing the pump throttle reduces the flow rate, which decreases the radial velocity component u_2, resulting in an increasing pressure rise per Equation 5.3. This explains the variation in pressure rise at a given speed from test to test.

In order to prime the pump, the water is pre-pressurized. As a result of the pressurization, there is flow through the pump even if it is not spinning. The negative pressure rise at low speeds indicates that in this region viscous losses through the pump blades are more dominant than the pumping power. This plot also illustrates the existence of certain dead spots where operation has not been achieved. This is due to the "jumping" method of starting and running the turbopump as discussed in Chapter 3.

5.2.2 Pumping Power

The pump power can be determined by

$$\mathcal{P}_{pump} = \frac{1}{\eta_{pump}} \dot{m} \frac{\Delta P}{\rho} \tag{5.4}$$

with the isentropic pumping power defined as

$$\mathcal{P}_{isent} = \mathcal{P}_{pump} \eta_{pump} = \dot{m} \frac{\Delta P}{\rho} \tag{5.5}$$

Figure 5-4 shows the isentropic pumping power based on the measured ΔP across the pump plotted against the speed. Since the power is directly proportional to the pressure rise and the pressure rise quadratically related to speed, the pumping power is also quadratically related to the speed. The low values for pumping power can be explained by the low mass flow through the pump. Figure 5-5 shows the pressure rise of the pump as a function of the mass flow through the pump. Comparing Figures 5-4 and 5-5, it can be seen that tests with higher mass flow produce a larger pumping

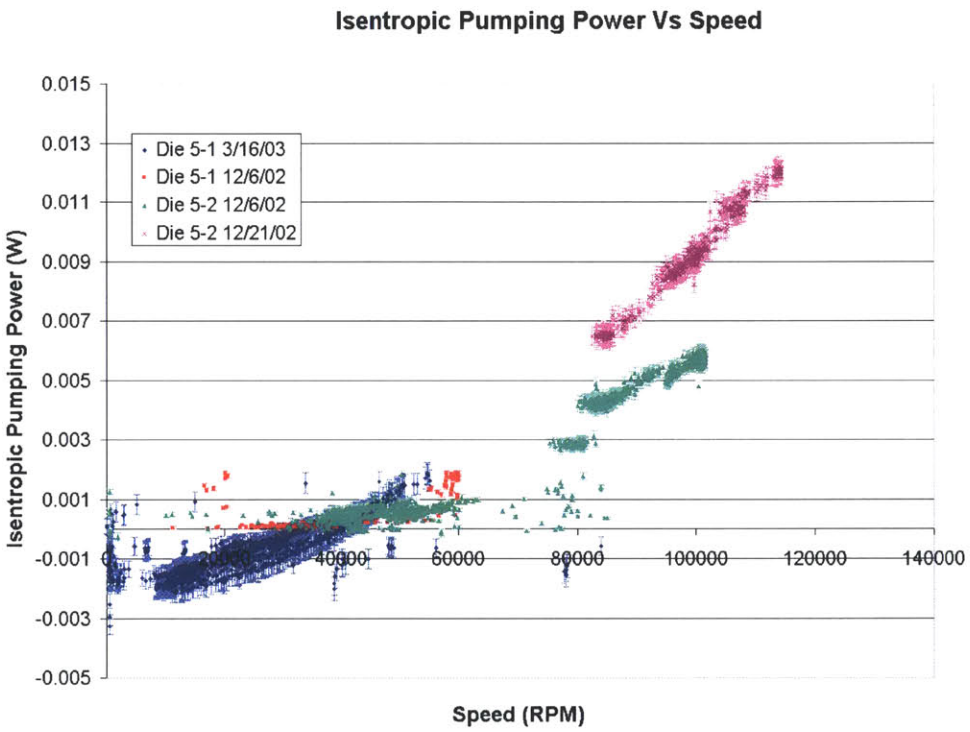

Figure 5-4: Pumping power as a function of rotational speed.

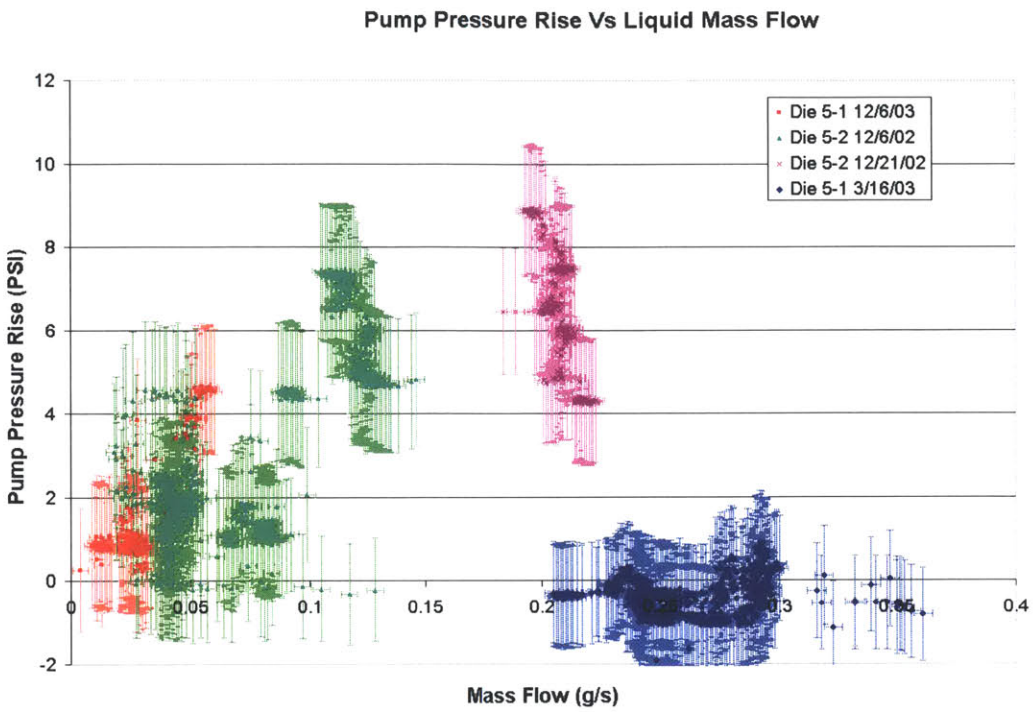

Figure 5-5: Pump mass flow plotted against the pump pressure rise.

power, as expected from Equation 5.4. As the pump is run closer to full speed, the mass flow through the pump will increase, and the pumping power should approach the predicted values.

5.3 Turbine Performance

The performance of the turbine can be examined using the same experiments as discussed above.

5.3.1 Pressure Relations

The pressure drop across the turbine is given as a function of speed in Figure 5-6. The expected value as indicated by Deux is also shown on this plot [2]. There is large variation in the turbine pressure drop at a given speed. This is partially due to the issues discussed above with regards to the mass flow through the pump. Depending

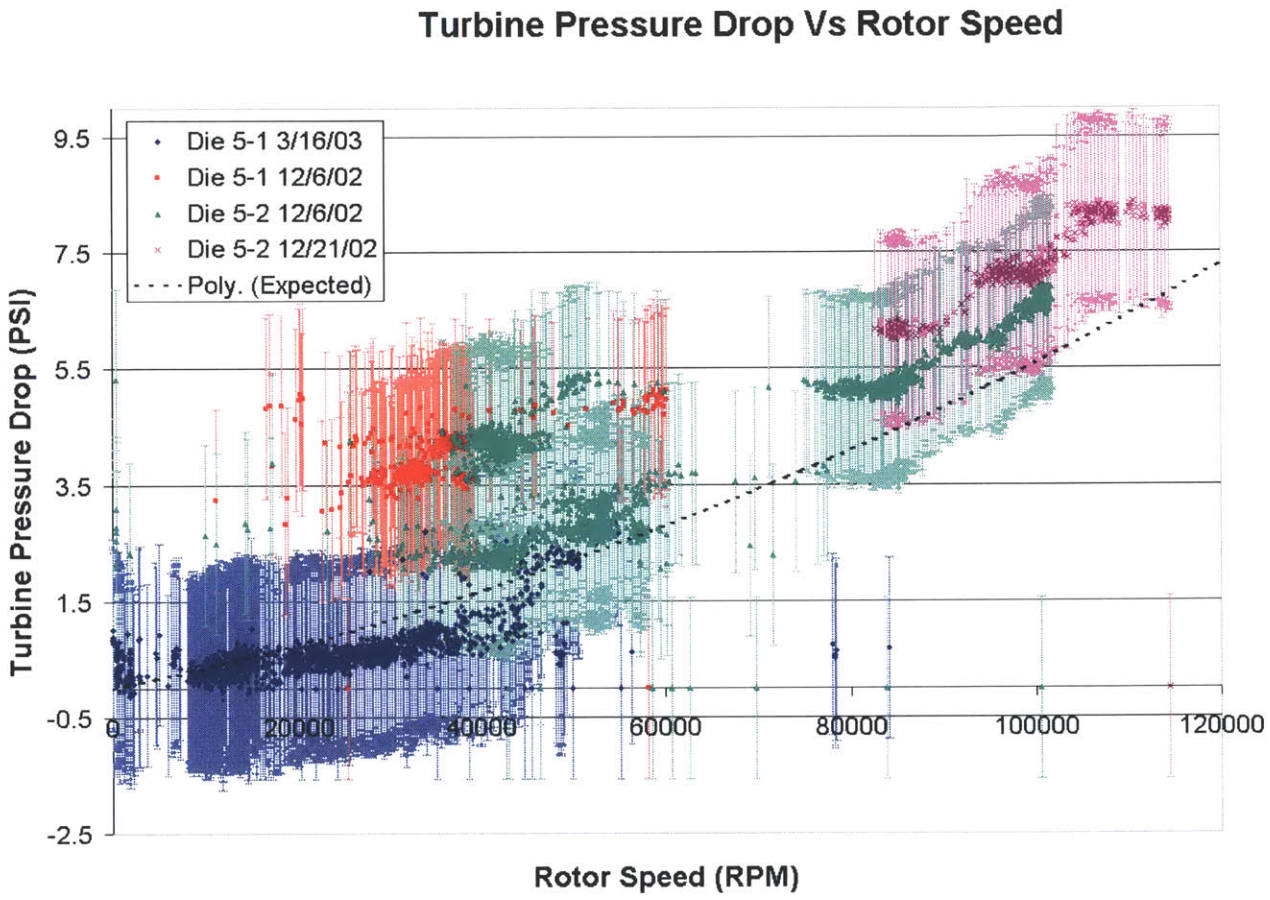

Figure 5-6: Pressure drop through the turbine blades as a function of rotational speed.

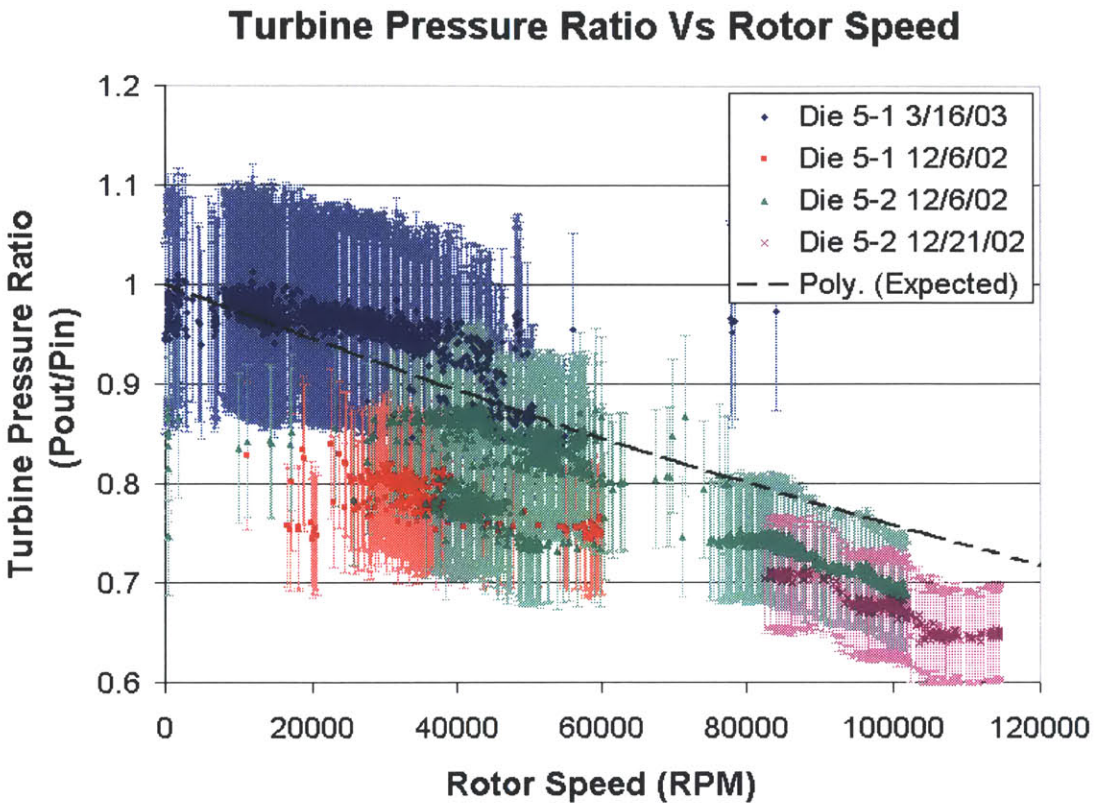

Figure 5-7: Turbine pressure ratio as a function of rotational speed.

on the mass flow through the pump, the turbine may need to produce a smaller or larger amount of power to spin up to a certain speed. This power is a function of the pressure ratio across the turbine and will be discussed in the next section. The turbine also produces the power dissipated in the bearings. Near natural frequencies and other instabilities, the bearing flow may fluctuate, causing a change in the power lost to that bearing. In order to accommodate changing power requirements, the turbine pressure drop may change at a given speed.

5.3.2 Turbine Power

Figure 5-7 shows the turbine pressure ratio π_p as a function of speed. The pressure ratio appears to be approximately the expected value, with variations similar to those for the turbine pressure loss. The mass flow through the turbine given as a function of

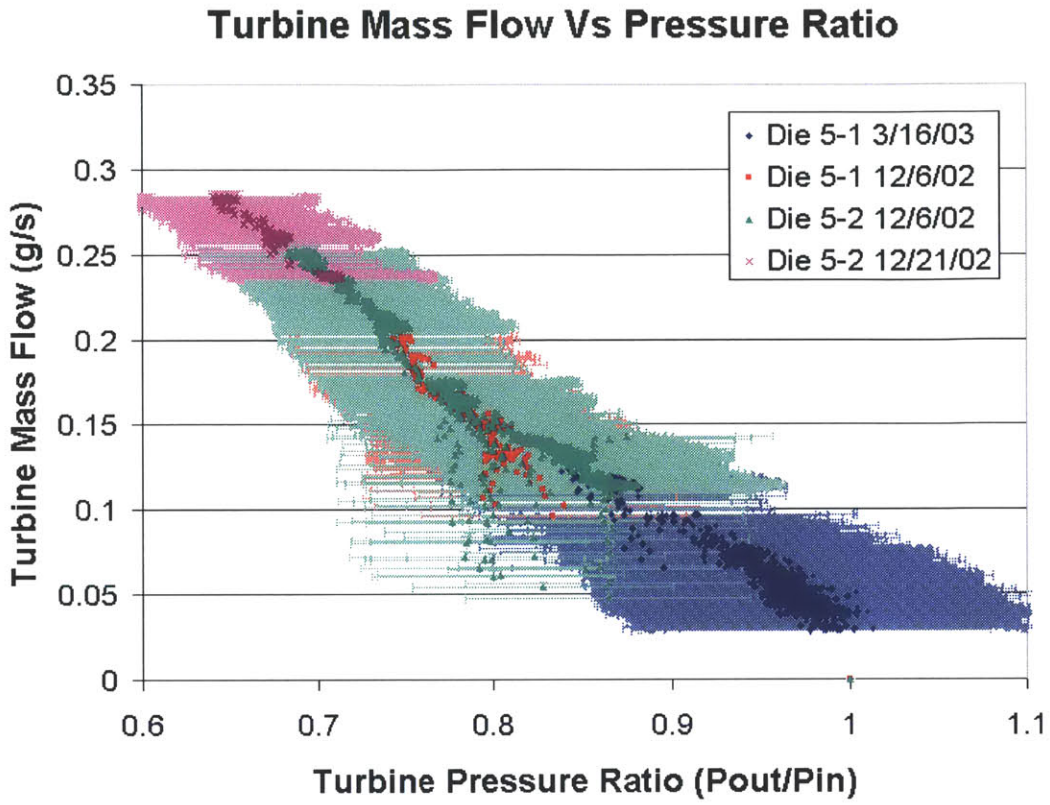

Figure 5-8: Turbine pressure ratio as a function of rotational speed.

pressure ratio in Figure 5-8. The mass flow seems to vary linearly with the pressure ratio. This is expected as the turbine exit pressure is kept constant and the turbine throttle setting has been kept constant throughout these tests, giving the turbine exit a fixed resistance.

The turbine power is described as

$$P_{turbine} = \dot{m}C_p(T_{tin} - T_{tout}) = \dot{m}C_pT_{tin}(1 - \pi_t^{\frac{\gamma-1}{\gamma}}) \tag{5.6}$$

where T_{tin} is the total temperature at the inlet to the turbine and π_t is the turbine pressure ratio. Here C_p is assumed to be a constant. This represents the maximum amount of power that the turbine could create for the given total temperature and pressure ratio assuming the turbine is adiabatic or the isentropic turbine power. To get the shaft power delivered by the turbine, an additional turbine efficiency would

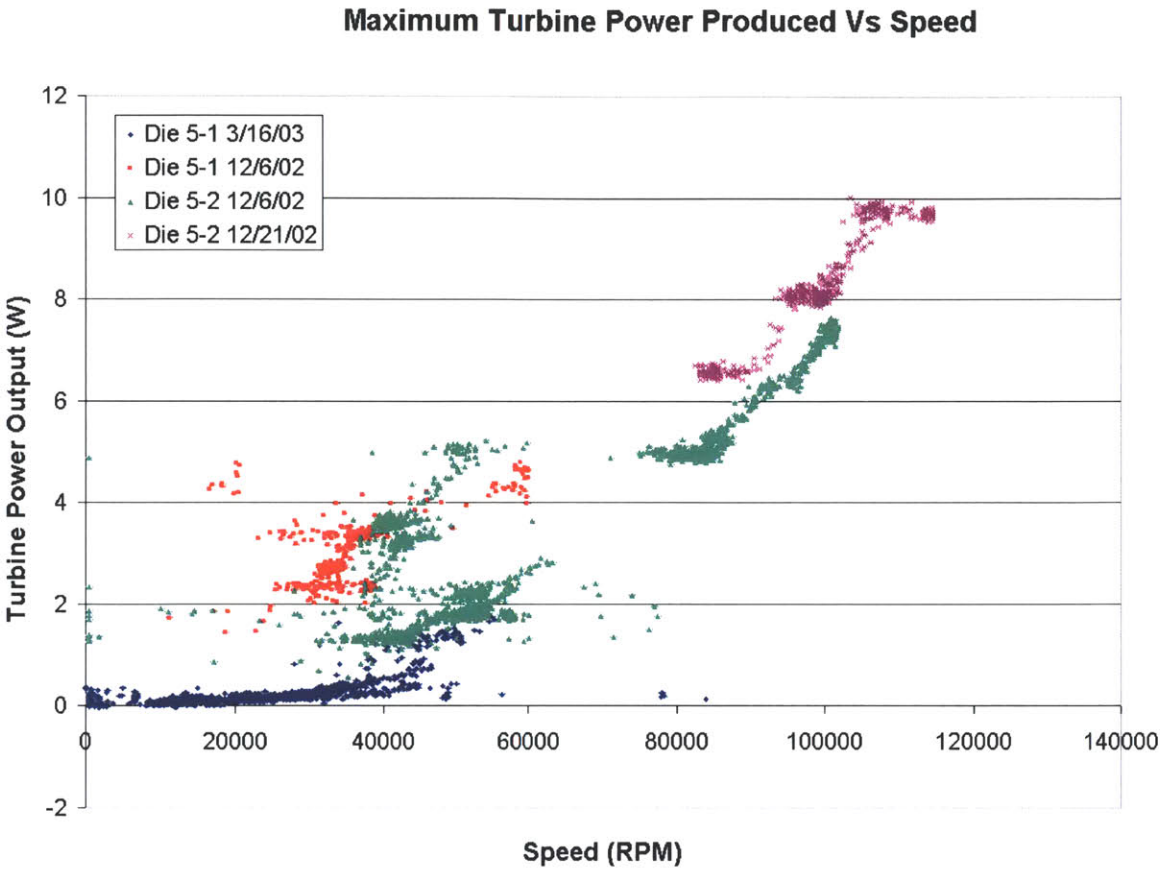

Figure 5-9: Calculated turbine power.

be added. Figure 5-9 shows the isentropic turbine power delivered as a function of speed.

5.4 System Efficiency

If the system is operating isentropically, with no loss to the bearings, then the ratio of the isentropic pumping power to the isentropic turbine power should be 1. Therefore, the ratio of the isentropic powers is a measure of how far the system is operating from isentropic conditions, and thus a measure of total system efficiency. This defines a

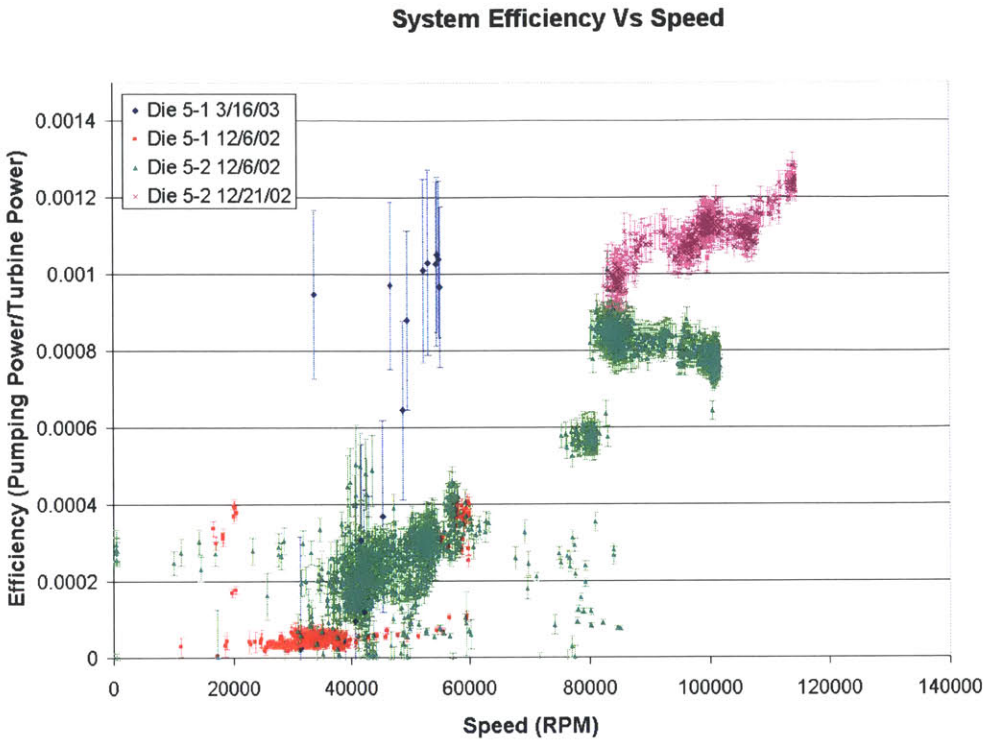

Figure 5-10: Calculated system efficiency.

general system efficiency as

$$\eta_{system} = \frac{\text{Isentropic pumping power}}{\text{Isentropic turbine power produced}} \tag{5.7}$$

By taking the pumping power shown in Figure 5-4 and dividing by the turbine power shown in Figure 5.2, this efficiency can be calculated. Figure 5-10 plots this system efficiency as a function of the speed of the rotor. As the rotor speed increases, the efficiency also increases. This indicates that at higher speeds, the micro turbopump achieves more pumping power for a given turbine pressure ratio.

Another way to approach the efficiency is through a power balance:

$$\mathcal{P}_{Turb} = \mathcal{P}_{Pump} + \mathcal{P}_{Loss} \tag{5.8}$$

Substituting in for the pump and turbine powers gives

$$\eta_{turb} C_p \left(1 - \pi_t^{\frac{\gamma-1}{\gamma}}\right) = \frac{\dot{m}\Delta P}{\eta_{pump}\rho} + \mathcal{P}_{Loss} \tag{5.9}$$

Assuming that $\mathcal{P}_{Cliff}$ is negligible at these low speeds, this can be rearranged for the system efficiency defined as

$$\eta_{sys} = \eta_{turb}\eta_{pump} = \frac{\frac{\dot{m}\Delta P}{\rho}}{C_p \left(1 - \pi_t^{\frac{\gamma-1}{\gamma}}\right)} \tag{5.10}$$

which is exactly the system efficiency shown in Figure 5-10.

At design speed, the pump power required is 36 Watts [2]. With the assumed 30% efficiency, this leads to 10.8 Watts of isentropic pumping power. The turbine power delivered should be 50 Watts. With the 30% efficiency, this implies 167 Watts of isentropic turbine power. Therefore, at design conditions, the system efficiency as defined above should be approximately 6.5%. At 0.12%, the current tests have shown the pump operating at about 2% of design efficiency. Assuming, as suggested by Equation 5.10, that the system efficiency is approximately η_{pump} times η_{turb} and assuming that these two efficiencies are equal, the efficiency of each component can be estimated at 3.5% at the top speeds shown. Figure 5-10 indicates that this system efficiency is increasing with rotor speed. These low values for efficiency can be attributed to the fact that the pump is being operated far off design. These efficiency numbers are expected to improve as the rotor speed is increased.

5.5 Summary

A brief discussion of the blade design of the demonstration micro turbopump is given. Preliminary data for the turbomachinery is presented. Data pertaining to the pressure rise and drop through the pump and turbine, respective powers, and system efficiency is shown and discussed. The ability to use turbomachinery to pump liquids on the microscale has been proven. In general the pump is operating as expected,

although low system efficiencies indicate that there may be more optimal settings for turbopump operation.

Chapter 6

Summary and Conclusions

This thesis details the first pumping tests of the demonstration micro turbopump as well as some of the design, modeling, and testing procedures that enabled these tests to take place. This chapter will summarize the major points of this thesis and discuss recommendations for future work.

6.1 Summary

The concept of a microfabricated turbopump has been reviewed, and the place for such a pump in a micro rocket engine system has been discussed. The reasons for creating a demonstration turbopump as a platform for proving the feasibility of a micro turbopump have been addressed.

The design of the demonstration micro turbopump has been discussed, and the process behind the design changes that have occurred over the past 2 years have been detailed. Reasons for the redesigns were given and the current demonstration micro turbopump design has been presented. The inclusion of aft exhaust ports into the design as well as the addition of an anisotropic journal bearing plenum is detailed.

A brief overview of the test rig has been given with discussions of the new packaging. A successful starting procedure for the demonstration micro turbopump has been outlined, and procedures for low-speed operation have been discussed. An axial balance model has been presented, and the implications of the new device design on

axial balance have been considered. A number of possible piping options have been presented to allow for automatic axial balancing. Problems with coupled forces on the aft side of the rotor have been discussed and the inverted journal bearing has been presented as a partial solution. A brief discussion of surface tension effects inside the forward bearing seals has been given.

The journal and thrust bearing systems have been described. A thrust bearing model has been presented and used to present the effects of fabrication errors on system performance. Static test data and rotordynamic data has been presented for the bearing systems.

The first proof of liquid pumping by a turbomachine on the microscale has been presented. Data pertaining to the performance of the turbine blades and pumping blades has been shown and discussed.

6.2 Conclusions

The major conclusion of the work presented in this thesis is that the demonstration micro turbopump is able to pump water with a positive pressure rise of approximately 10 PSI. The turbomachinery is acting as expected, and the pressure rise and power of the pump vary quadratically with the rotational speed, as expected.

Better understanding of the highly coupled aft bearing system in turbopump builds 1 through 5 has lead to operational procedures aimed at decoupling the aft pressures. This problem should be avoided on future turbopump builds by designing aft exhaust ports. Information on the axial position of the rotor is critical, and the ability to get this information should be considered when designing new systems. The effects of choked flow in the bearing injectors should also be considered in future designs.

Operational procedures, especially at low speeds and start-up are critical to running the micro turbopump. Starting the pump can be a difficult problem, and design implications on start-up procedures are important to note.

6.3 Future Work

More testing is necessary to continue to verify the design of the demonstration micro turbopump. Testing at a range of different pump throttle settings and inlet pressures is recommended to find the best operating point for the micro turbopump. Future experiments with axially self-balanced rotors should be explored only after the operational regime of the pump is well understood.

Although only briefly discussed in this thesis, the problems involving the surface tension forces in the forward thrust bearing and seal require more study. Understanding this force and its interaction with the pressures in the forward seal will be more and more critical as the pump speed is increased.

At higher speeds, turbomachinery performance should be compared with the CFD predictions. Cavitation limits should also be investigated, and bearing data should be compared to rotordynamic models at high speeds to determine the accuracy of the natural frequency and instability boundary predictions.

The main micro turbopump should be developed with both the successes and the difficulties of the demonstration pump in mind. Care should be taken to improve upon the current design and use as many existing features as possible, in order to learn from the experiences gained with the demonstration pump.

Appendix A

Current Demonstration Micro Turbopump Photomasks

The following 14 masks were used for build 6 of the demonstration micro turbopump. The marks indicating die saw location have been added in to help locate the features. These corners only exist on the first mask.

Level: 1
Side: Front
Wafer Thickness: 450um
Etch Depth: 350um
Etch #: 1/1 front, 1/2 total
Haloes: no

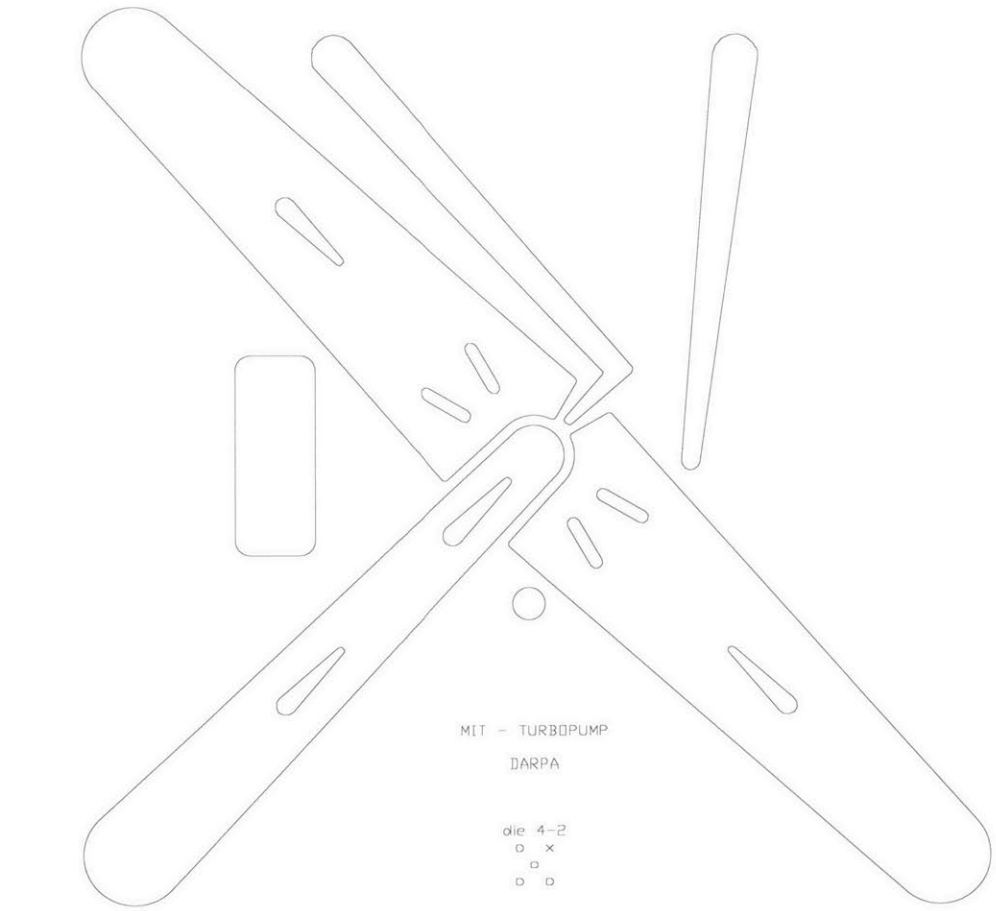

Level: 1
Side: Back
Wafer Thickness: 450um
Etch Depth: 100um
Etch #: 1/1 back, 2/2 total
Haloes: no

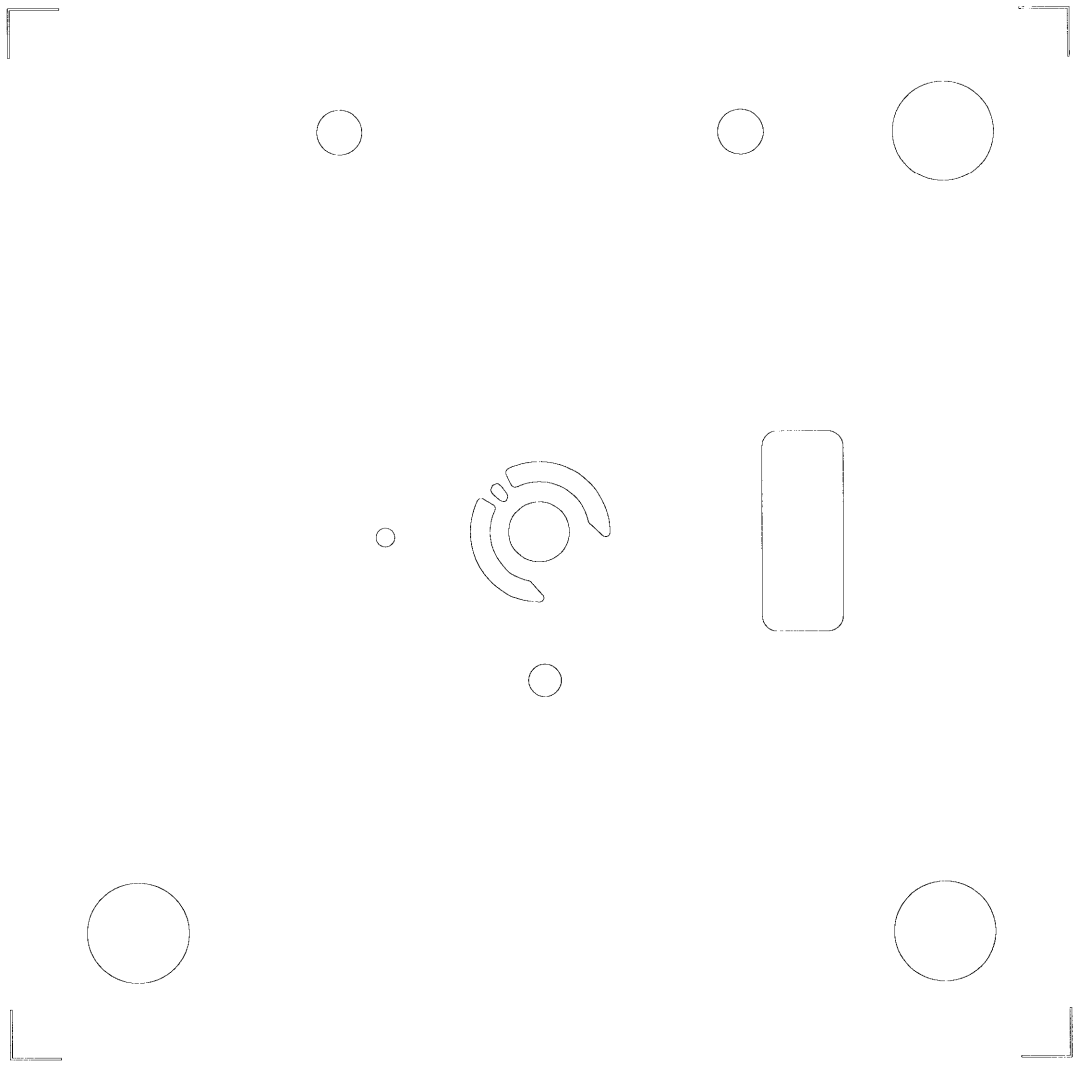

Level: 2
Side: Front
Wafer Thickness: 450um
Etch Depth: 350um
Etch #: 1/1 front, 1/3 total
Haloes: no

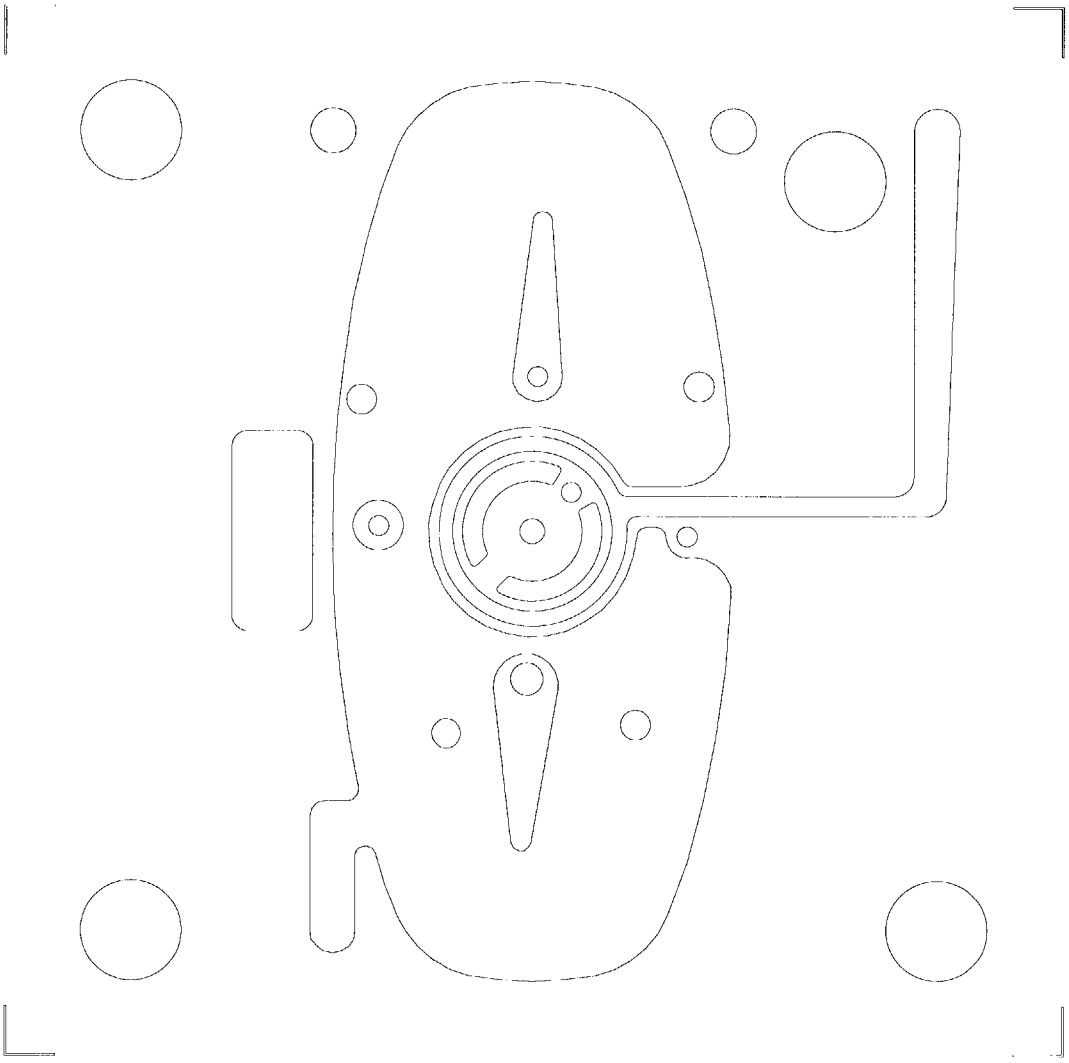

Level: 2
Side: Back
Wafer Thickness: 450um
Etch Depth: 20um
Etch #: 1/2 back, 2/3 total
Haloes: no

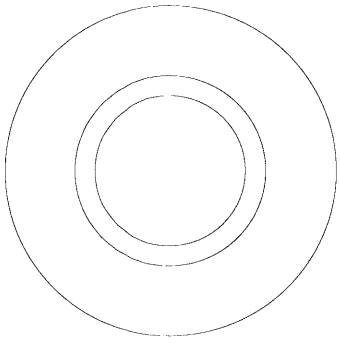

Level: 2
Side: Back
Wafer Thickness: 450um
Etch Depth: 100um
Etch #: 2/2 back, 3/3 total
Haloes: yes

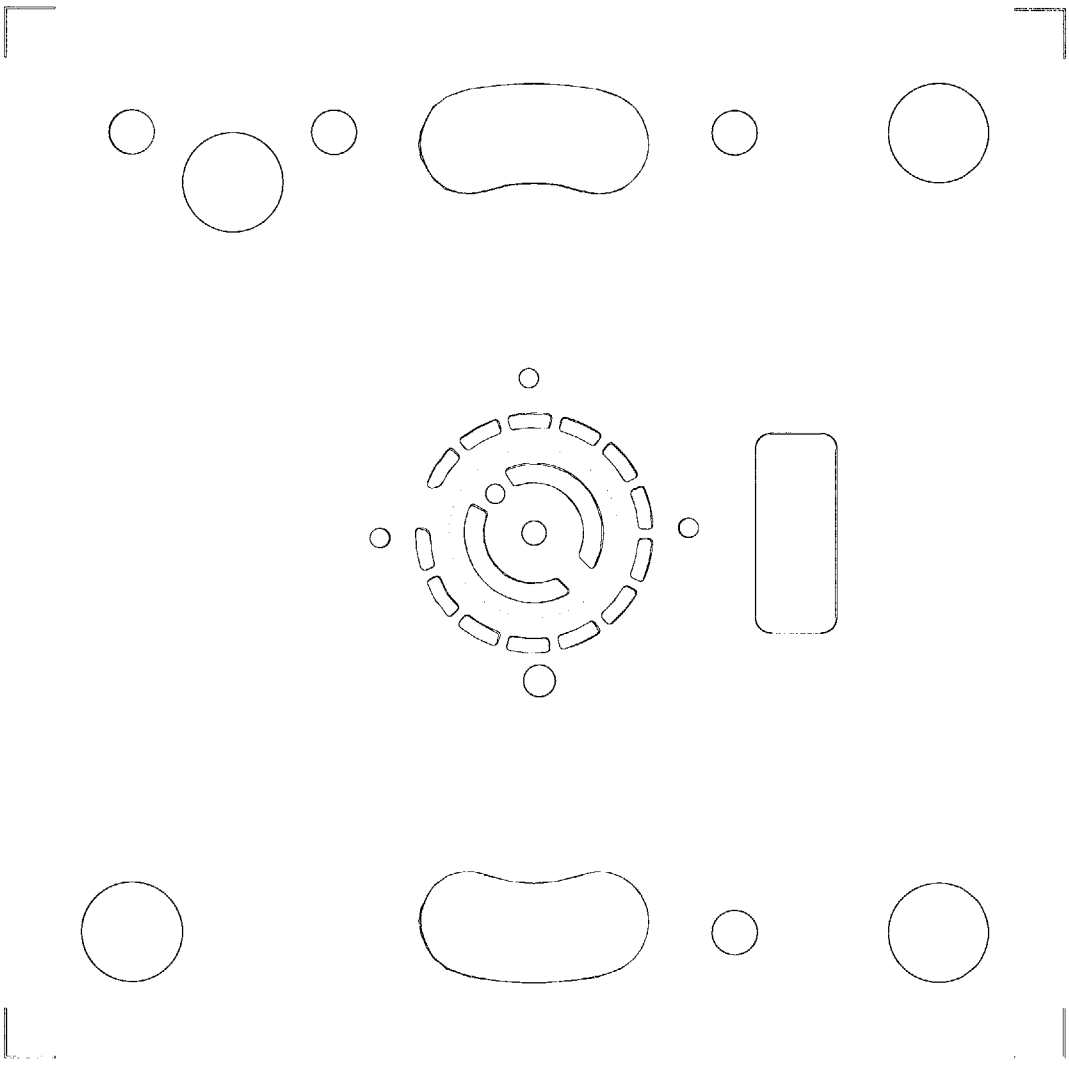

Level: 3
Side: Front
Wafer Thickness: 542um
Etch Depth: 0.5um
Etch #: 1/2 front, 1/3 total
Haloes: no

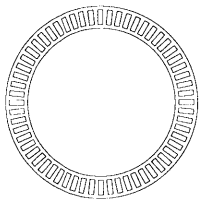

Level: 3
SIde: Front
Wafer Thickness: 542um
Etch Depth: 222
Etch #: 2/2 front, 2/3 total
Haloes: no

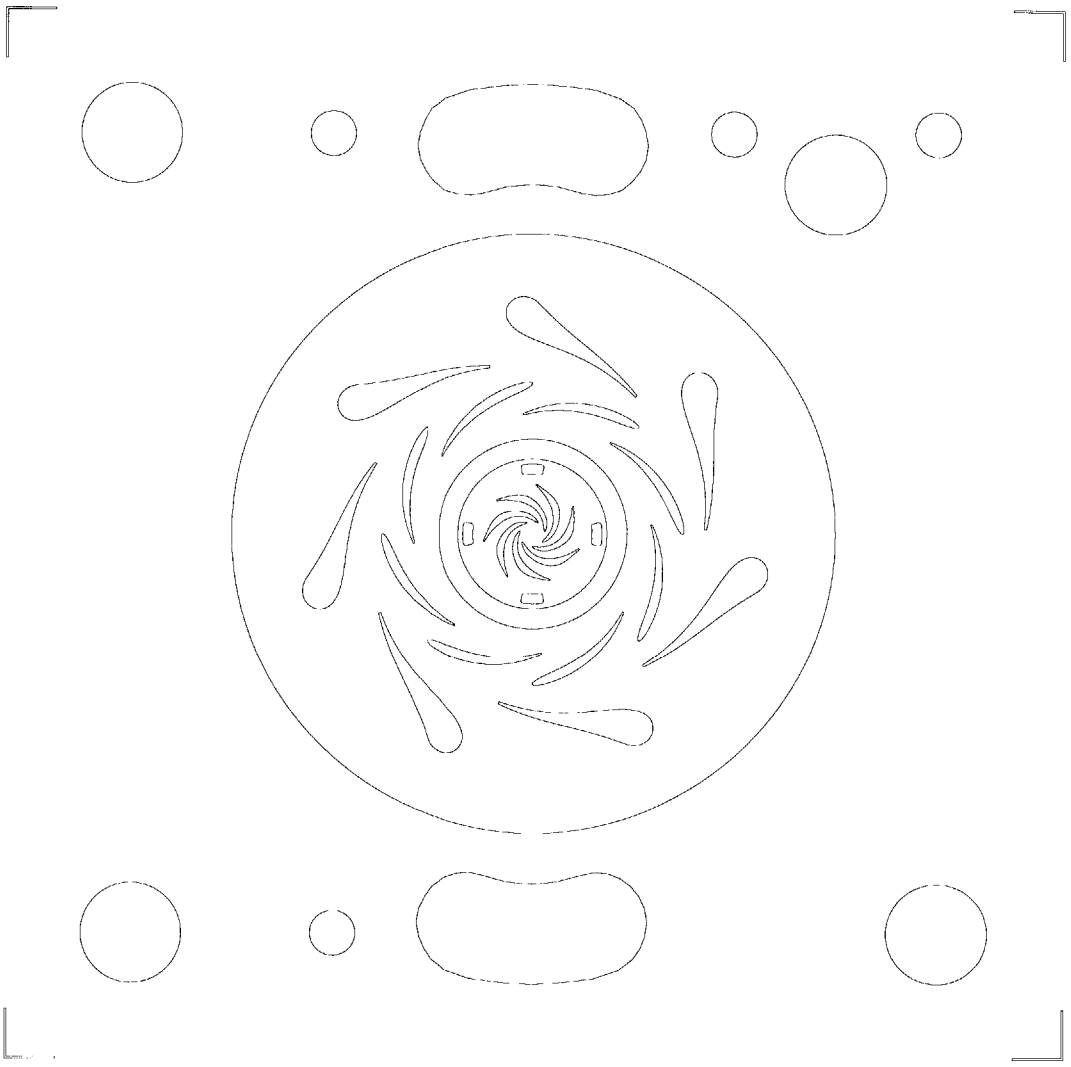

Level 3:
Side: Back
Wafer Thickness: 542um
Etch Depth: 320um
Etch #: 1/1 back, 3/3 total
Haloes: yes

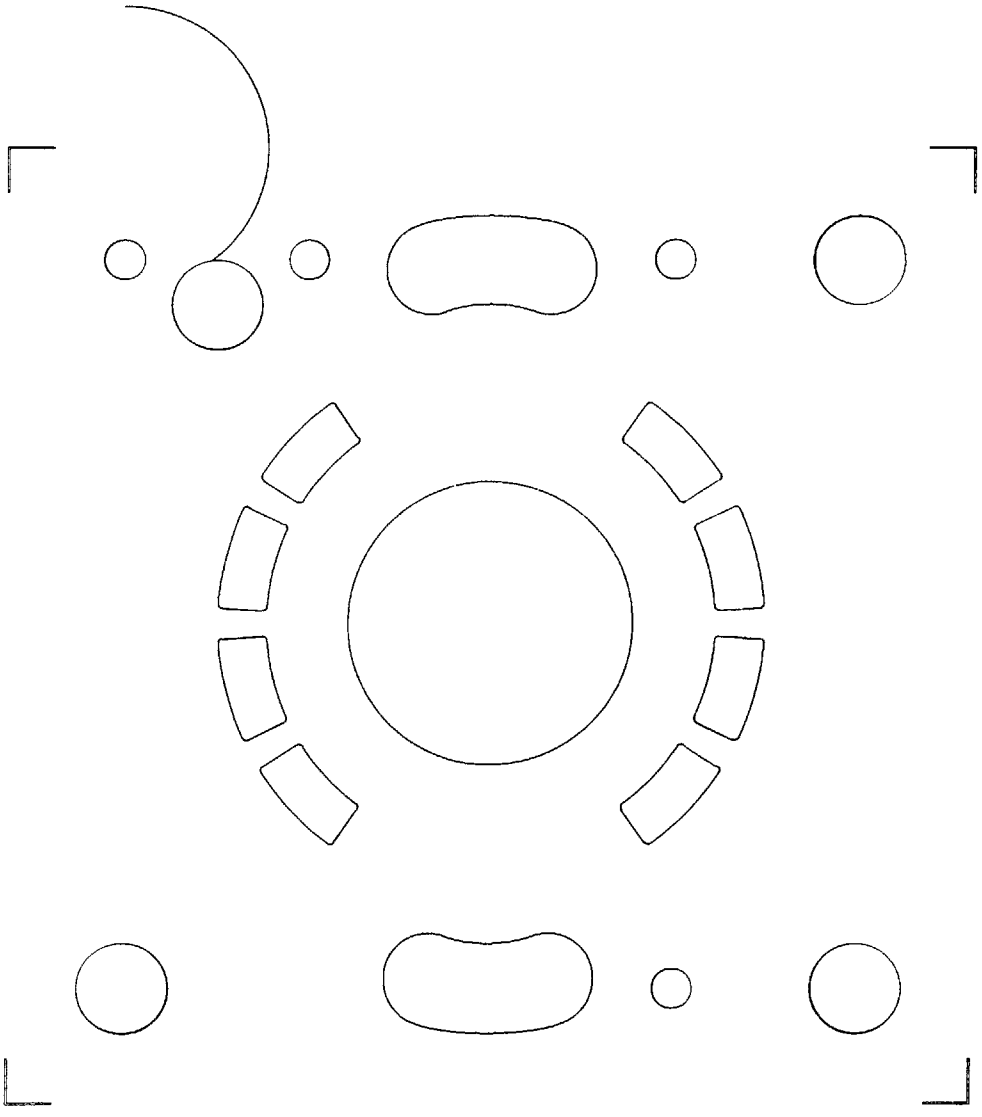

Layer: 4
Side: Front
Wafer Thickness: 450um
Etch Depth: 4.5um
Etch #: 1/3 front, 1/4 total
Haloes: no

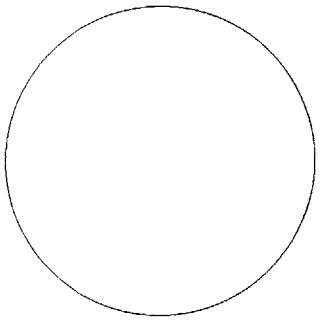

Level: 4
Side: Front
Wafer Thickness: 450um
Etch Depth: 50um
Etch #: 2/3 front, 2/4 total
Haloes: no

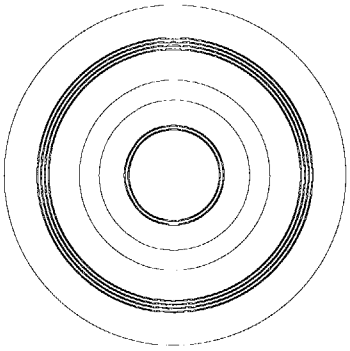

Level: 4
Side: Front
Wafer Thickness: 100um
Etch #: 3/3 front, 3/4 total
Haloes: no

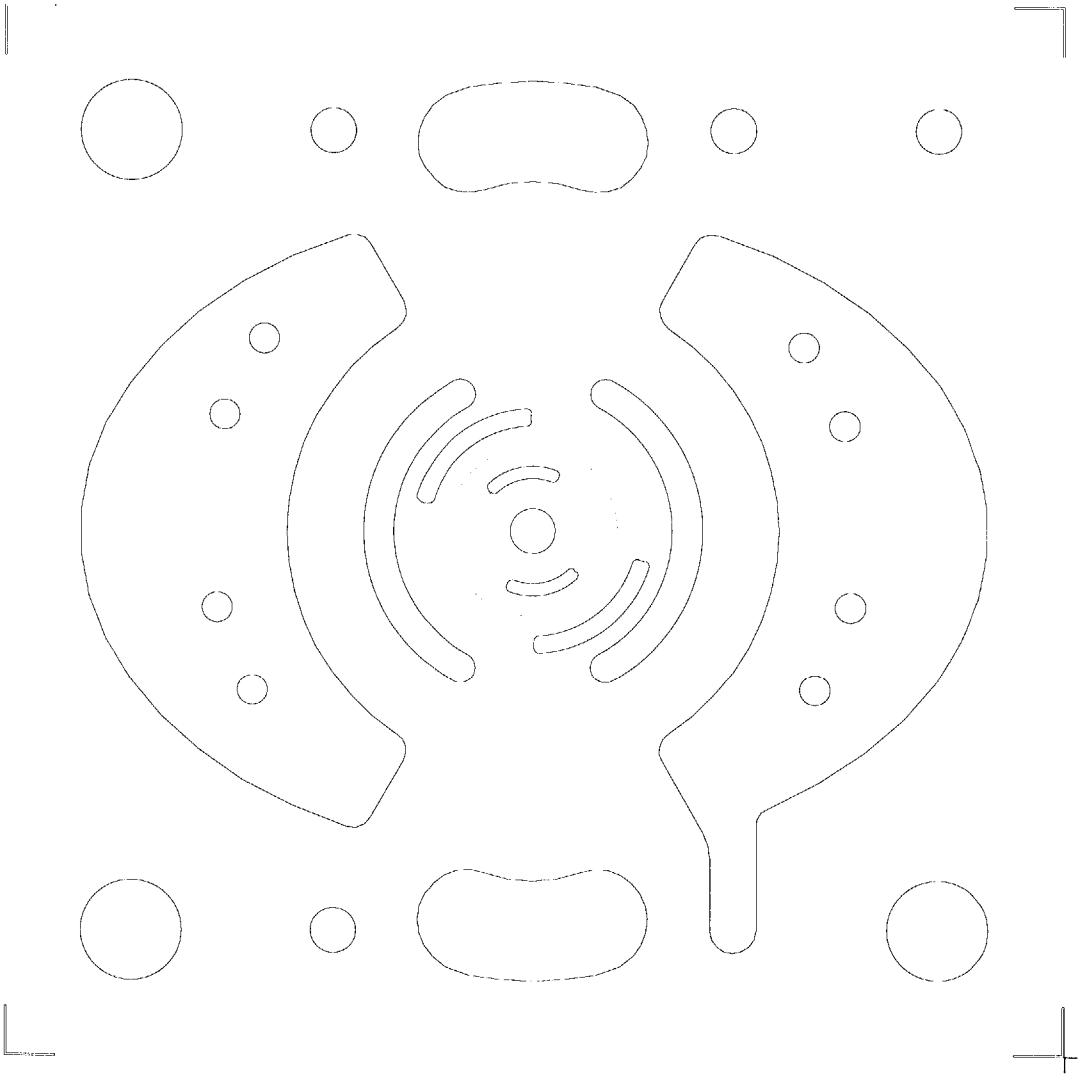

Level: 4
Side: Back
Wafer Thickness: 450um
Etch Depth: 350um
Etch #: 1/1 back, 4/4 total
Haloes: no

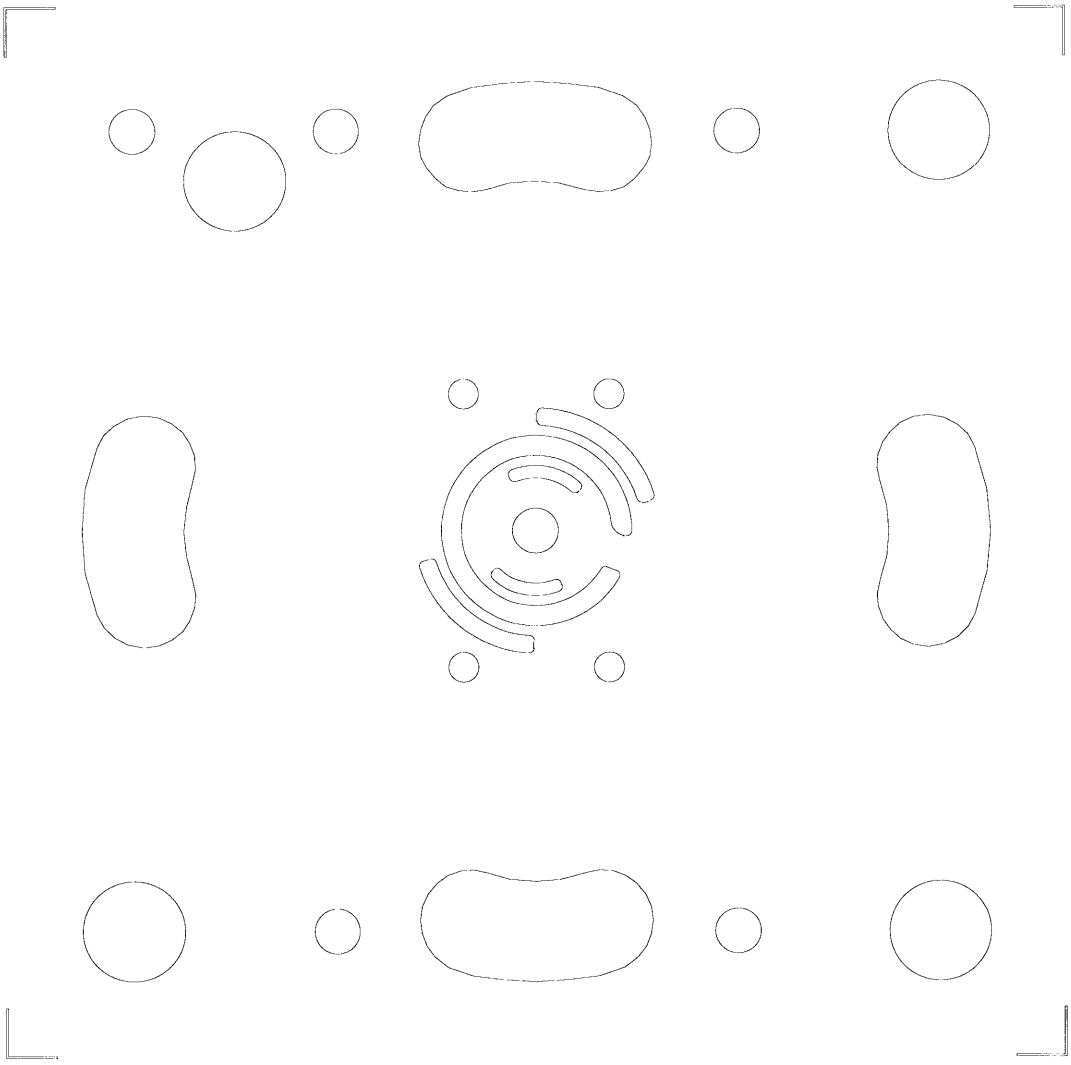

Level:5
Side: Front
Wafer Thickness: 450um
Etch Depth: 350um
Etch #1/1 front, 1/2 total
Haloes: no

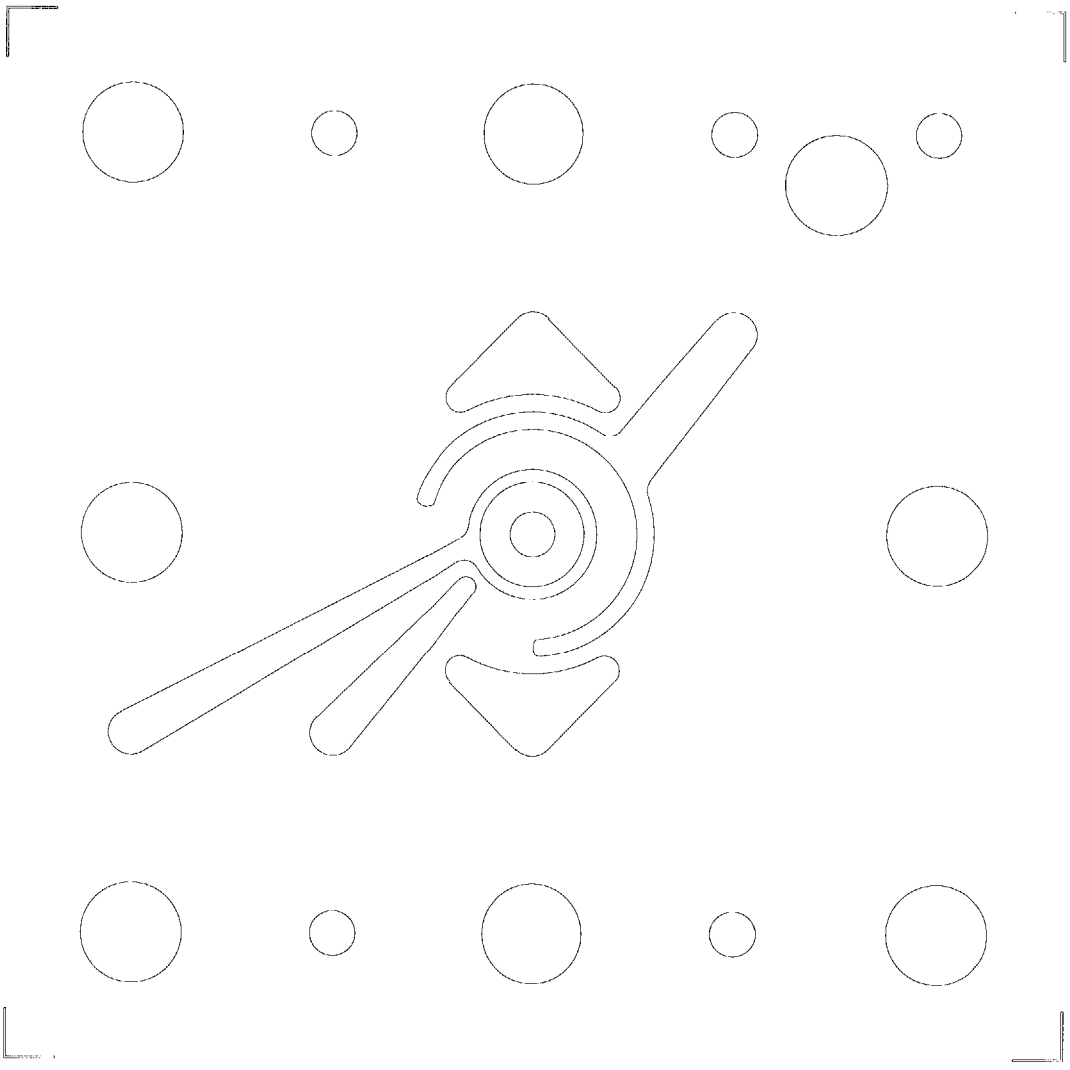

Level: 5
Side: Back
Wafer Thickness: 450um
Etch Depth: 100um
Etch #: 1/1 back, 2/2 total
Haloes: no

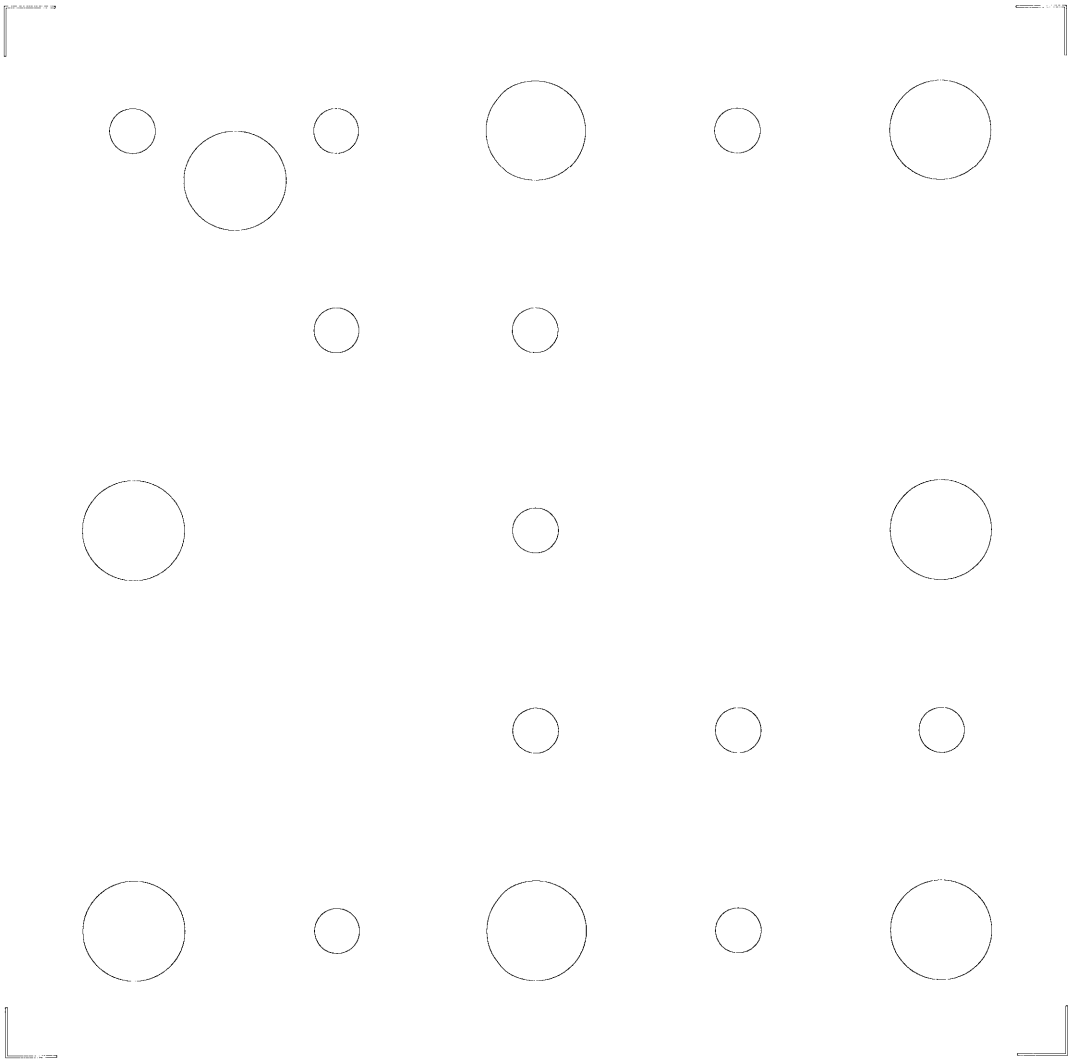

Appendix B

FEA Convergence Study

The following three plots show the convergence studies performed for each of the seal teeth modelled using NASTRAN. All three of these show that the analysis is converging to a single value, validating the final answers. The three cases tested correspond to a 100 micrometer long tooth (Figure B-1), a 50 micrometer long tooth (Figure B-2), and a 25 micrometer long tooth Figure B-3).

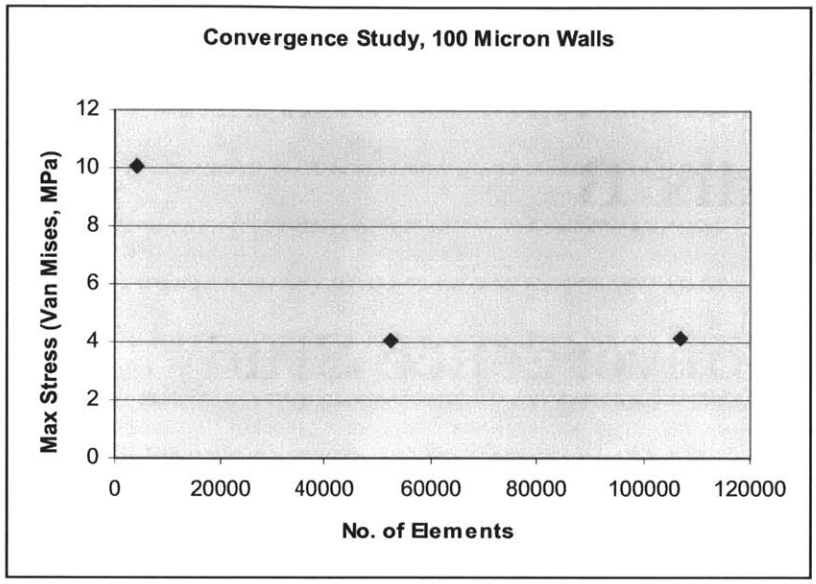

Figure B-1: 100 micrometer long seal tooth convergence study.

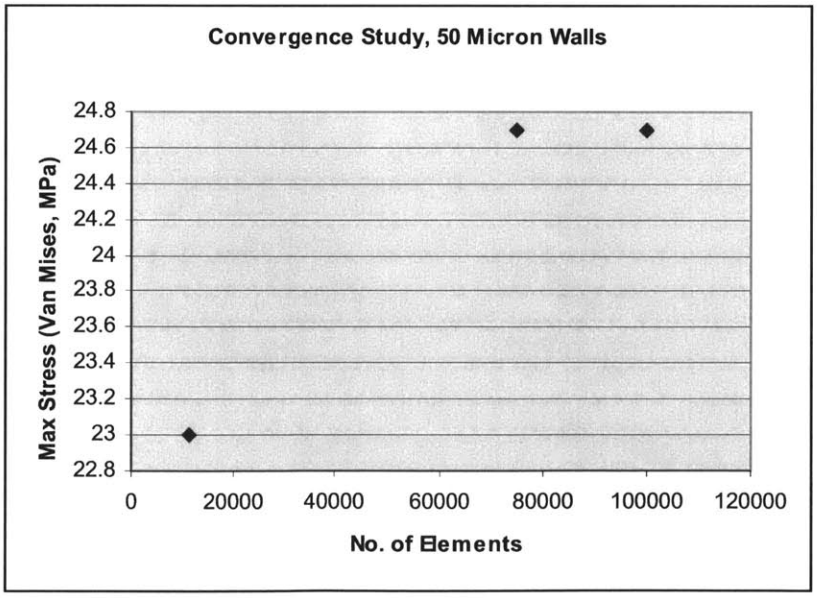

Figure B-2: 50 micrometer long seal tooth convergence study.

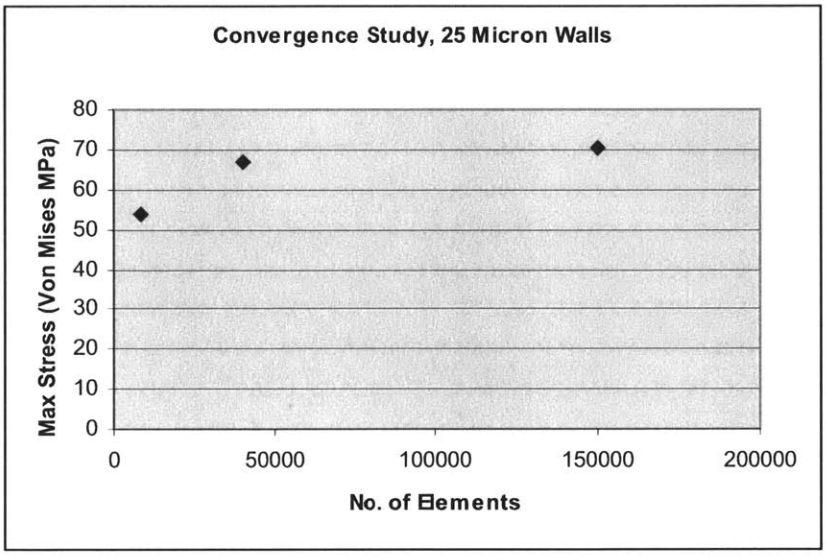

Figure B-3: 25 micrometer long seal tooth convergence study.

Appendix C

Seal Design CFD Details

This appendix contains more CFD results from the analysis done on the seals on the aft side of the new design of the turbopump. This analysis was completed by Teo [16].

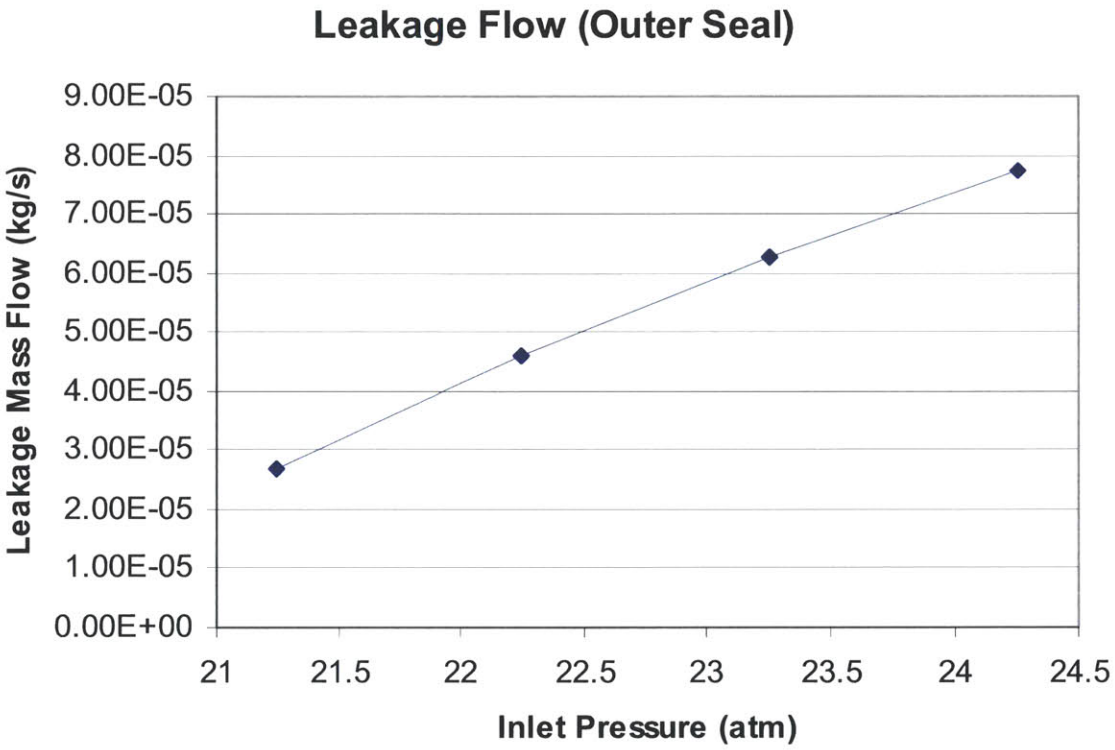

Figure C-1: Leakage flow for the outer seal.

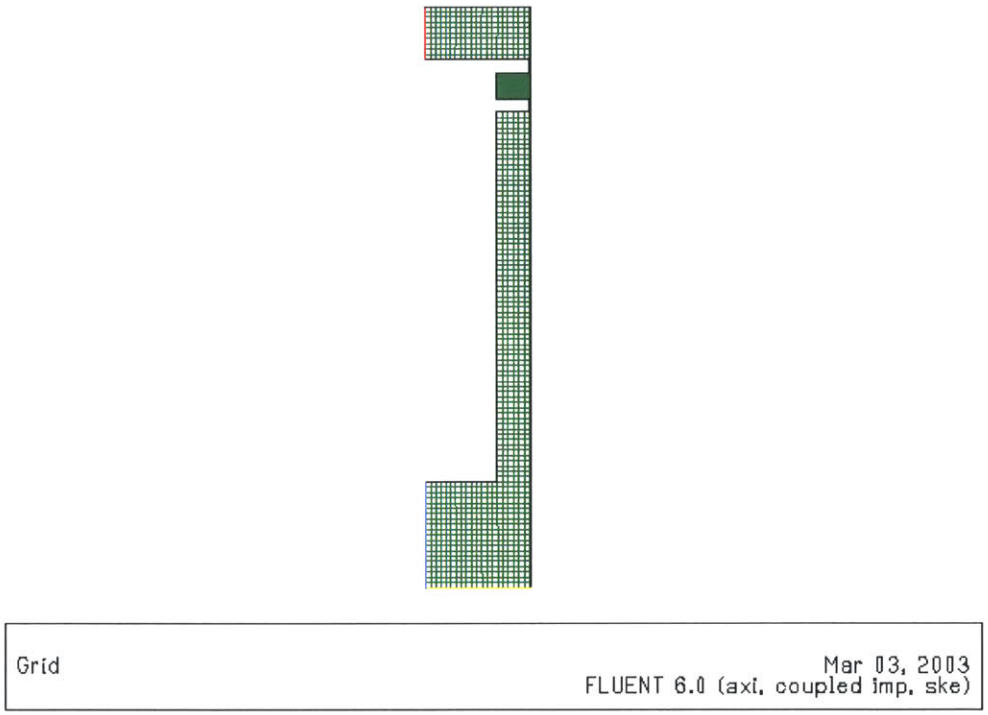

Figure C-2: Sketch of the grid used for the inner seal.

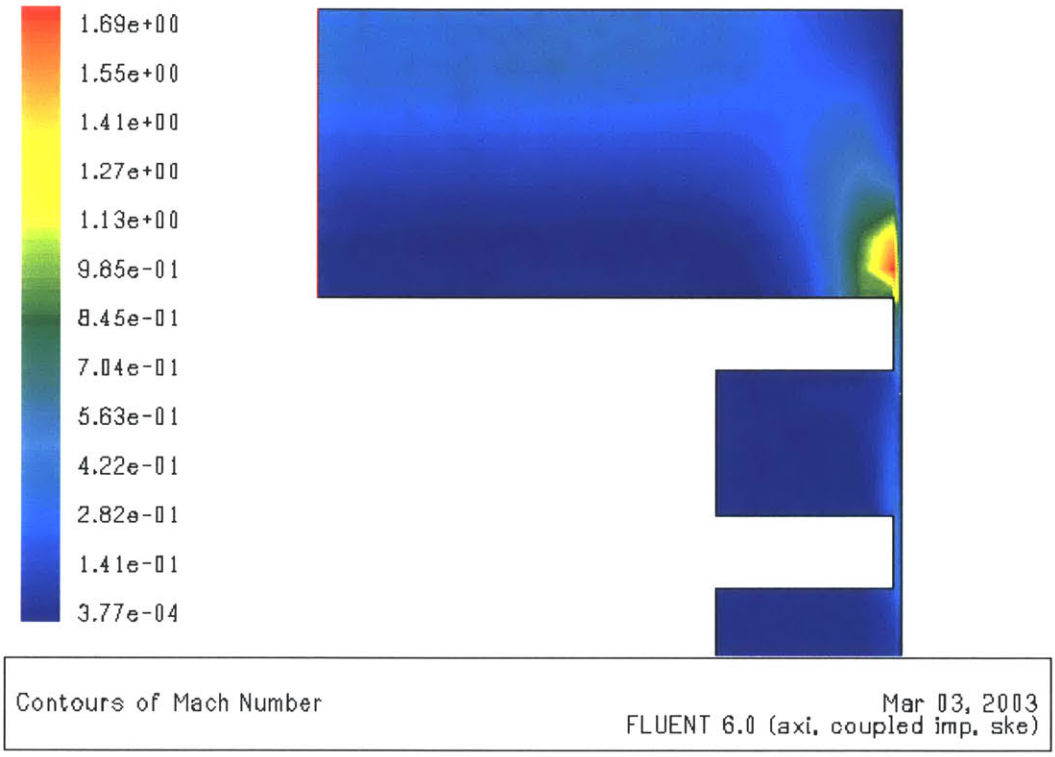

Figure C-3: Mach number for the inner seal.

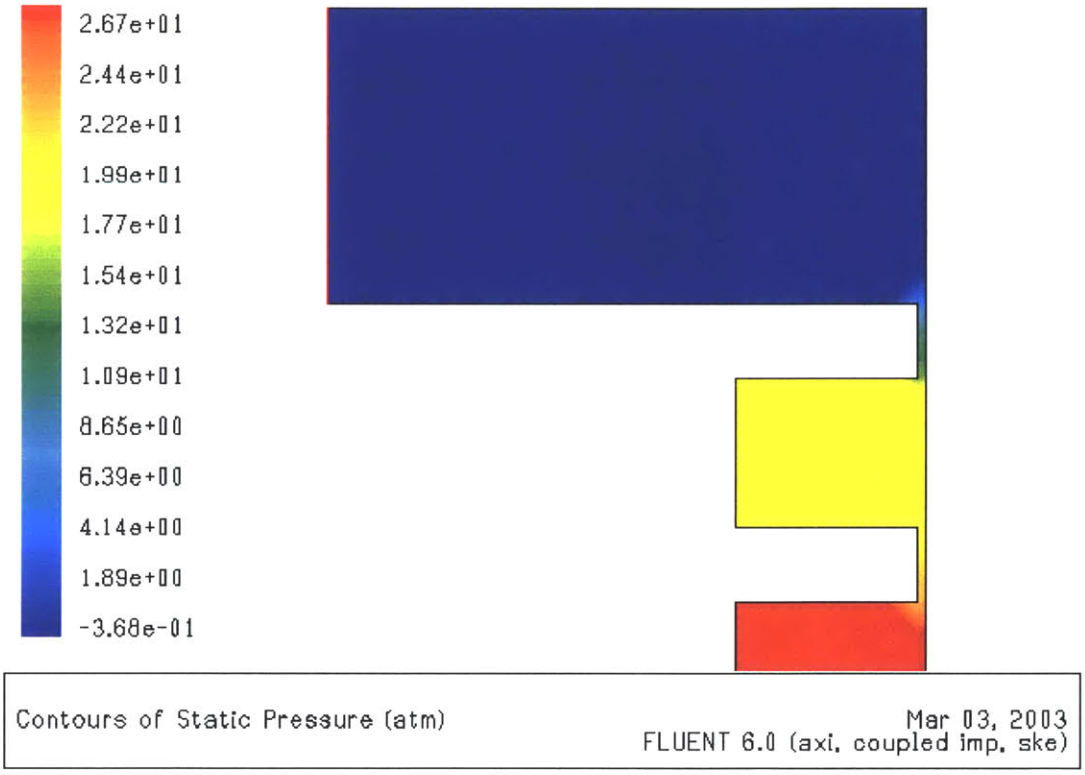

Figure C-4: Contours of static pressure for the inner seal.

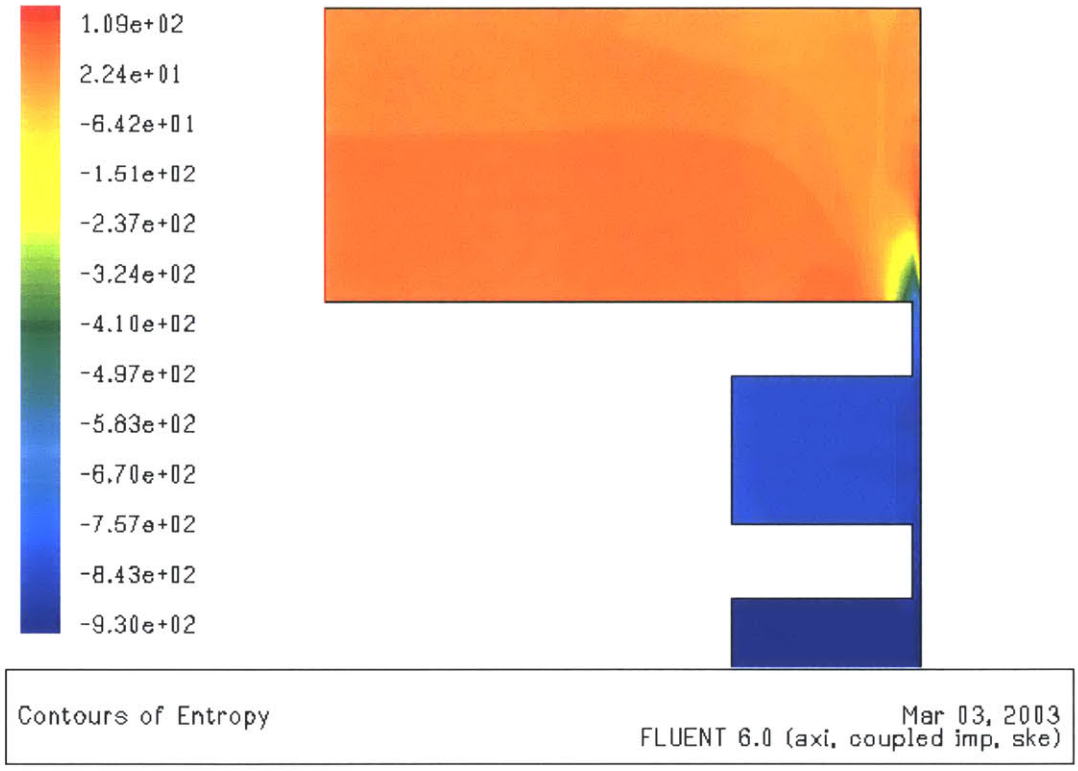

Figure C-5: Contours of entropy for the inner seal.

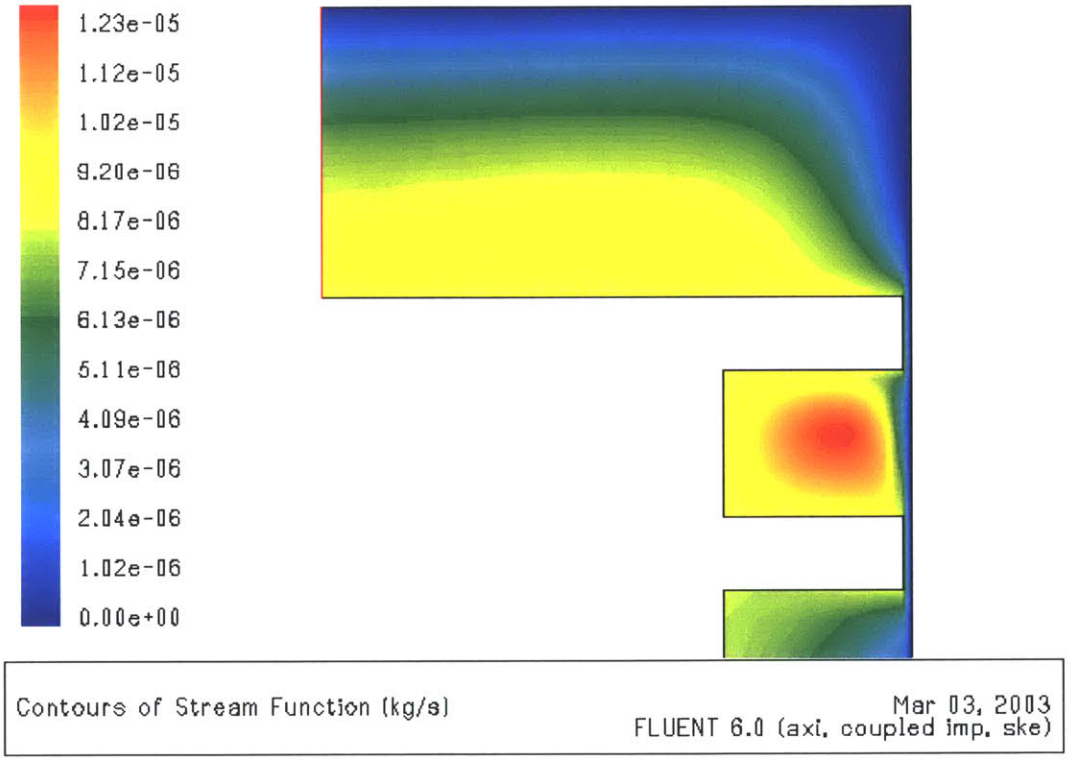

Figure C-6: Contours of stream function for the inner seal.

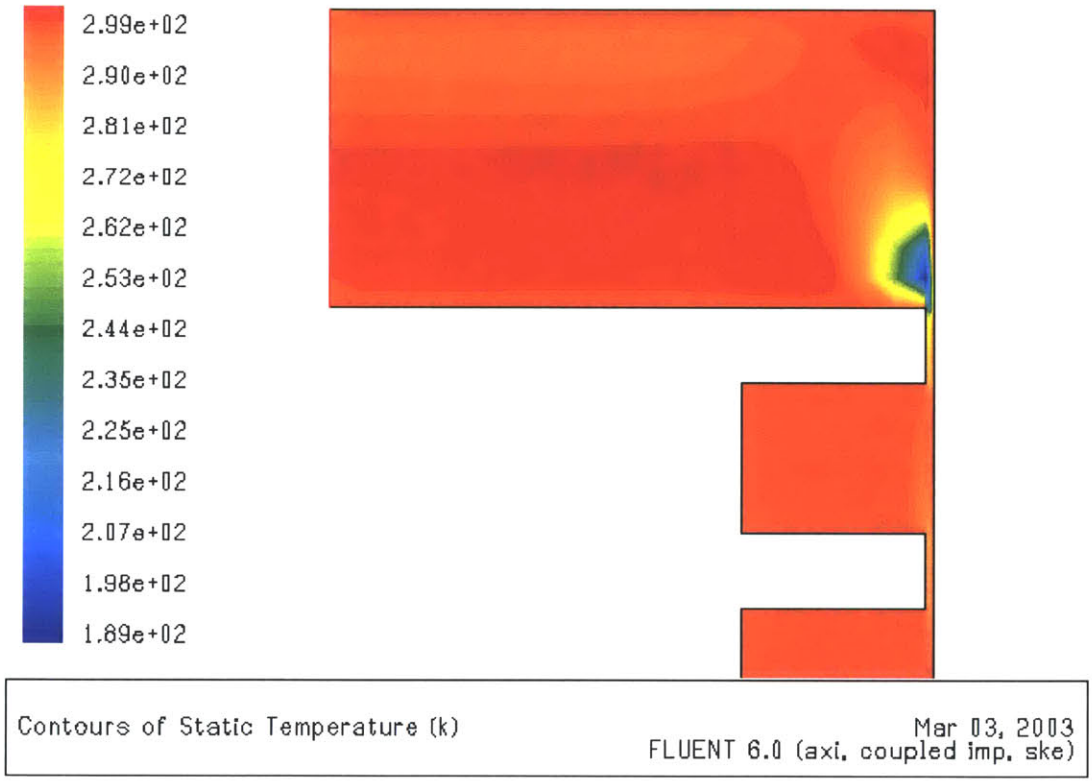

Figure C-7: Contours of static temperature for the inner seal.

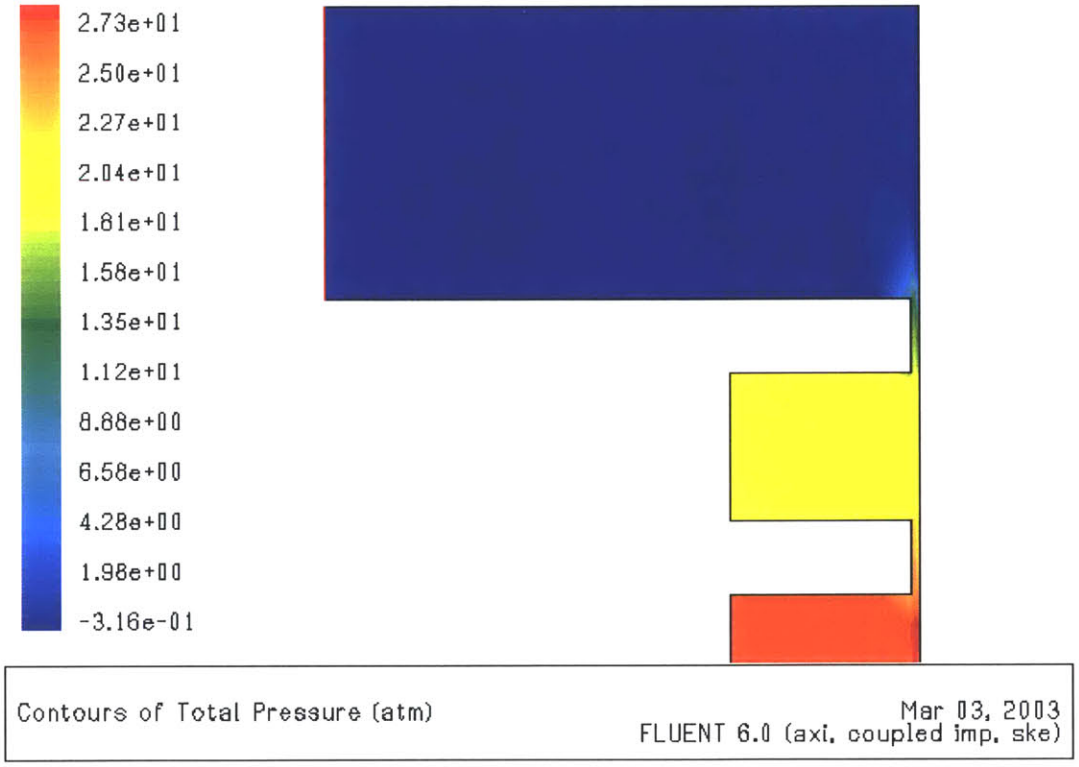

Figure C-8: Total pressure for the inner seal.

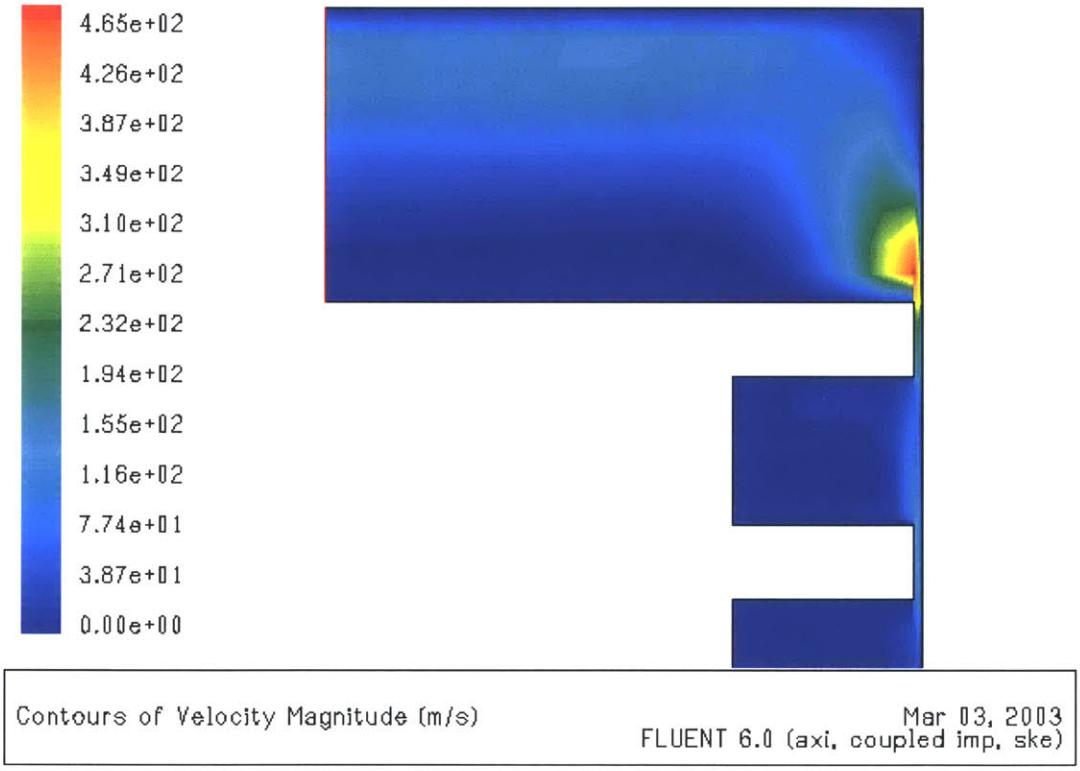

Figure C-9: Velocity magnitude for the inner seal.

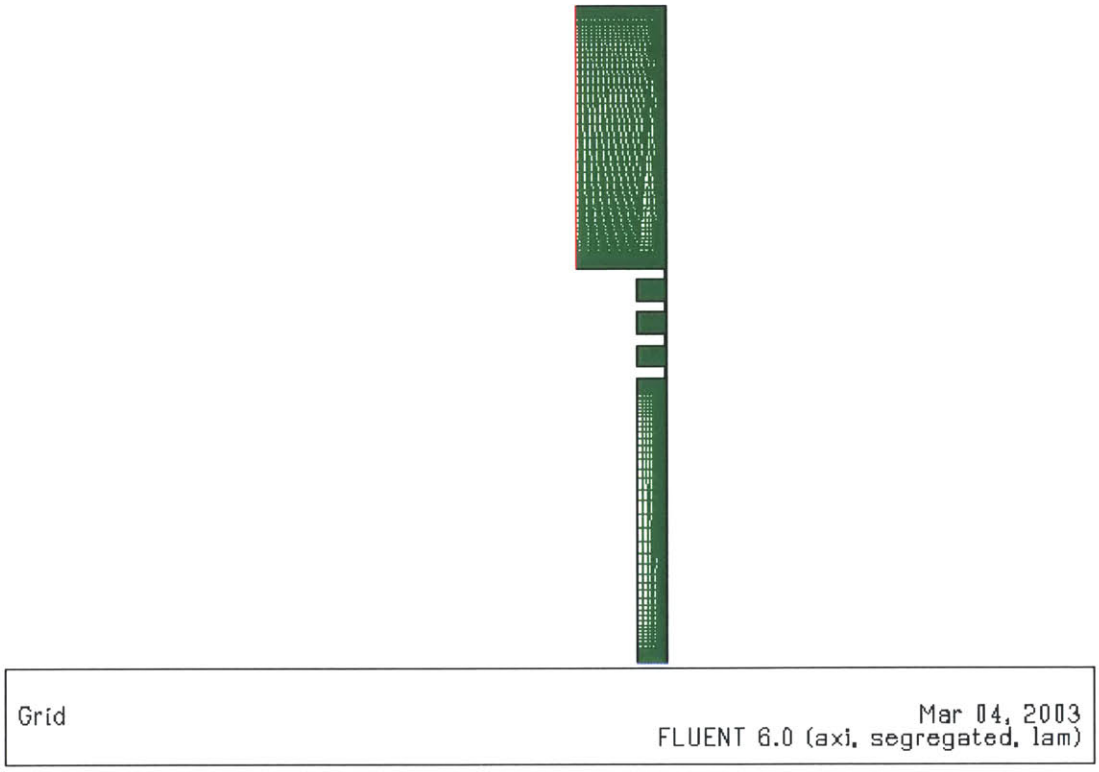

Figure C-10: Velocity magnitude for the outer seal.

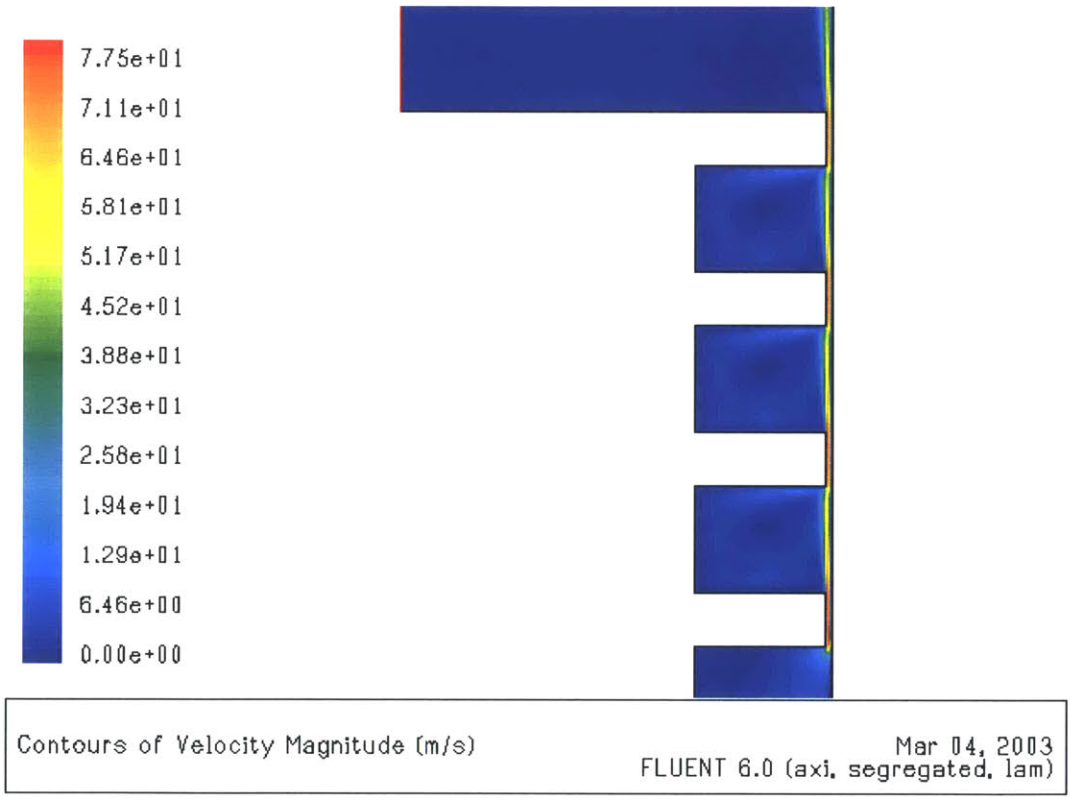

Figure C-11: Grid design for the outer seal.

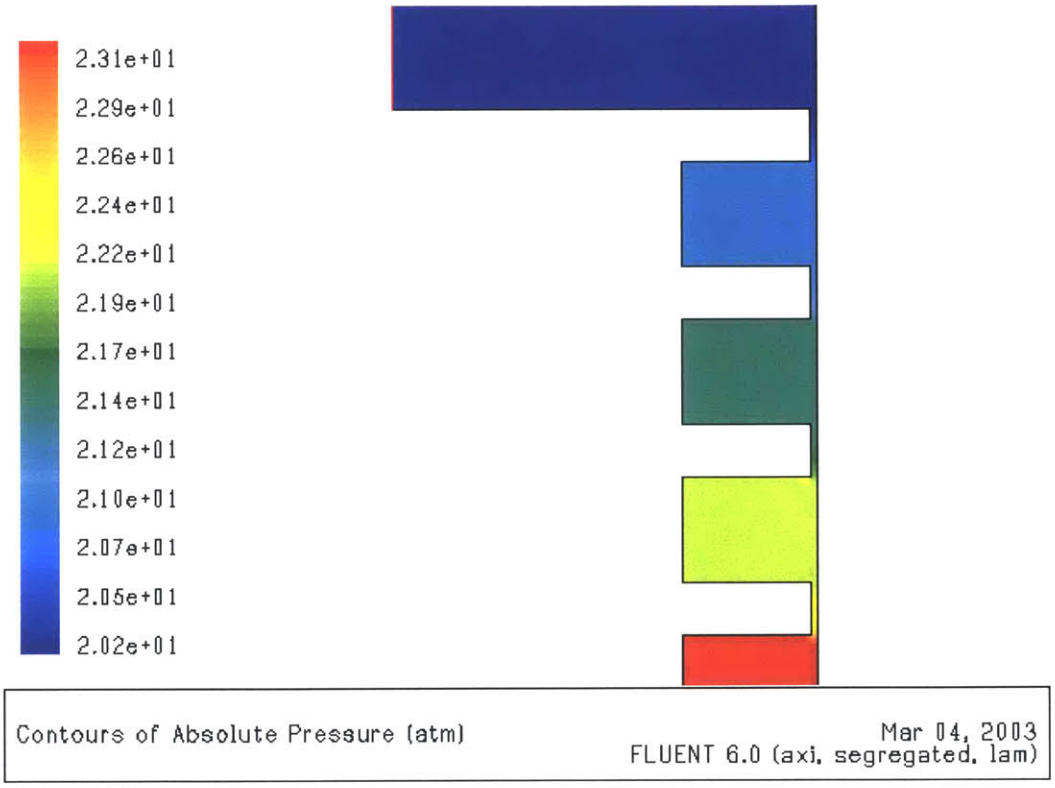

Figure C-12: Absolute pressure for the outer seal.

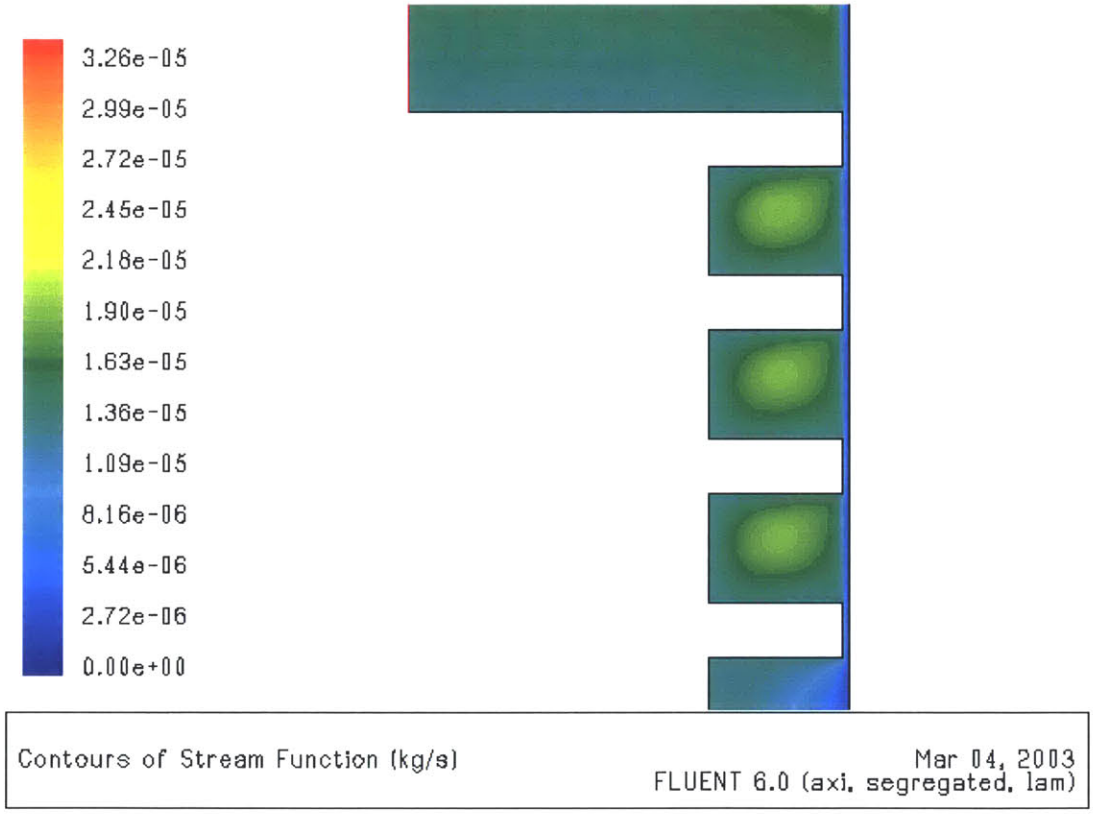

Figure C-13: Contours of stream function for the outer seal.

Appendix D

Pressure Transducer Calibration and Uncertainty Analysis

This appendix presents the recent calibrations performed on the demonstration micro turbopump rig and gives the methodology for determining the experimental error indicated throughout the data presented in this thesis.

D.1 Rig Calibration

The pressure transducers on the micro turbopump rig are calibrated by running the transducer in parallel to a precise sensor with a stated error of $\pm$ 0.2 psi. This measurement is then compared to the measurement given by the sensor to determine the accuracy of the sensor measurement. Due to the fact that all of the pressure transducers (regardless of range) are operating in the 0-100 psi range, the recent calibration was completed from 0-100 psi in order to capture the accuracy of the sensor in this region. The exception to this is the Sensotec differential pressure transducer which was calibrated from 0-25 psi because this is the range that this sensor operates in for the purposes of the micro turbopump.

The mass flow meters, both the Brooks Instruments thermistor meters as well as the Micro Motion Coreolis meters, are calibrated by the factory, therefore no experimental calibration data exists for them.

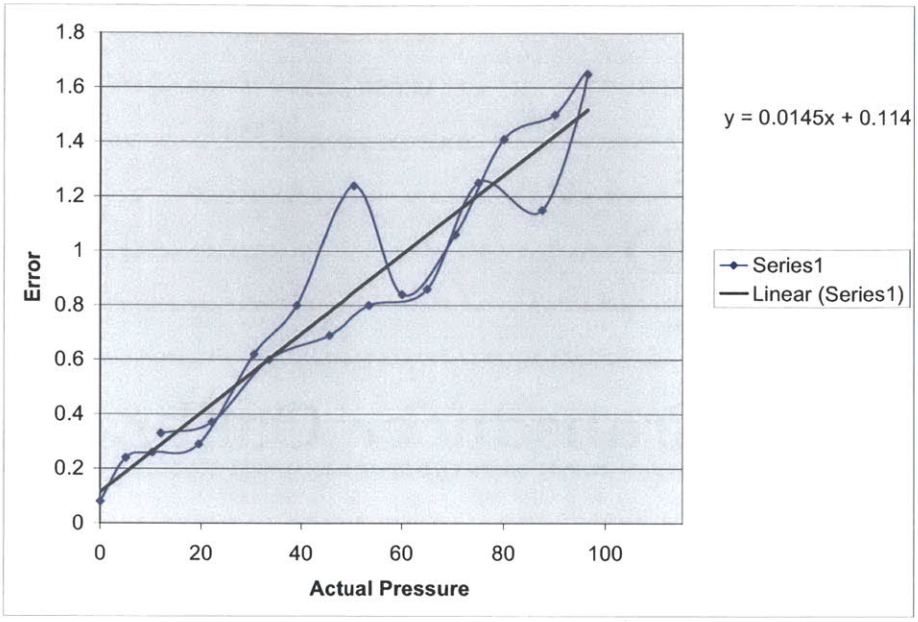

Figure D-1: Sample calibration plot. The important factors used in the uncertainty are the slope and intercept of the linear regression and the furthest distance from the linear regression.

The recent calibration of the micro turbopump rig produced graphs indicating the measured error of the the sensor. An example graph is shown in Figure D-1. The section on the pressure transducers will discuss how these graphs are used to determine the uncertainty for a given test.

D.2 Uncertainty Analysis

The uncertainty of any experimental data is an important factor to consider. The uncertainty that will be presented here is the fractional uncertainty defined as

$$S_x = \frac{\text{Uncertainty in value of x}}{\text{Indicated value of x}} = \frac{\delta}{\bar{x}} \tag{D.1}$$

The error will vary for each type of sensor as described below. Each measurement is zeroed by the DAQ system before each test [7].

Independent fractional errors can be added in a least squares sense, therefore, if

for a given sensor there are 3 sources of fractional error, the total fractional error would be given as

$$S_{overall} = \sqrt{S_1^2 + S_2^2 + S_3^2} \tag{D.2}$$

This will be used throughout the uncertainty analysis.

D.2.1 Acquisition Error

All data goes through the DAQ system before being processed. The signal is digitized at a 12-bit resolution. This creates an error that can be defined as

$$\frac{Range}{2^{12}} = \frac{Range}{4096} = \frac{1}{4096} = 0.025\% \tag{D.3}$$

In addition to this, the mass flow data Micro Motion mass flow meters produce data in the form of currents. These are converted to voltages using a resistor with a 5% error [7].

D.2.2 Flow Error

The flows through the turbine and pump are measured with Micro Motion CFM010 mass flow meters with a stated accuracy of [7]

$$S_{\dot{m}} = \pm 0.002 \pm \frac{0.0033 g/s}{\dot{m}} \tag{D.4}$$

They also have an acquisition error of

$$S_{Acq} = \pm 0.00025 \pm 0.05 = \pm 0.05025 \tag{D.5}$$

as discussed above. These two errors are added as described in Equation D.2.

The flows through the bearings and lower plenum are measured with Brooks Instrument 5860E thermistor mass flow meters. These have a stated accuracy of 1% of

the full range and a repeatability of 0.25%. This corresponds to a total error of

$$S_{\dot{m}} = \pm 0.0025 \pm \frac{0.01 * \dot{m}_{max} sccm}{\dot{m}} \tag{D.6}$$

where P_{max} is the maximum mass flow for the given sensor. The acquisition error is added as described in Equation D.2.

D.2.3 Pressure Error

The majority of the pressure transducers on the rig are Kulite pressure transducers which have been calibrated as discussed above. These sensors have a slope uncertainty, drift uncertainty, and linearity uncertainty. The slope uncertainty pertains to the drift in the error slope as shown in figure D-1. The drift uncertainty refers to the change in the zero point of the sensor from test to test. This is taken as the intercept of the slope shown in figure D-1 with the y axis. To get the fractional error, this number is divided by the current pressure. The linearity uncertainty refers to the uncertainty caused by the sensor error functioning in a nonlinear fashion. This fractional uncertainty is calculated by taking the largest drift from linearity and dividing this pressure error by the current pressure. In addition to these, there is a ±0.2psi variation in the accuracy of the gauge used to calibrate the sensors, and an acquisition error. These errors add according to Equation D.2 to give the total uncertainty in the pressure measurements as

$$S_p = \pm \sqrt{S_{Slope}^2 + \frac{P_{MaxVariation}}^2 + \frac{0.2psi}^2 + \frac{Drift}^2} \tag{D.7}$$

where$P_{MaxVariation}$, S_{Slope}, and Drift are the values given in Table D.1.

D.2.4 Speed Error

The speed acquisition sensor is calibrated by comparing the output reading of the DAQ to the direct signal measurement with an oscilloscope. The signal analyzer has a 0.035% error [7].

Table D.1: Pressure transducer uncertainties

Sensor Location	Slope	Drift (PSI)	Linearity (PSI)
Turbine In Rig	0.0116	0.0516	0.501
Turbine Out Rig	0.0145	0.114	0.39375
Forward Thrust Bearing	0.0043	1.2471	1.2848
Aft Thrust Bearing	0.0234	0.0038	0.4636
Lower Plenum	0.015	0.1445	1.1255
Pump Out Rig	0.0317	0.0187	0.38675
Pump In Rig	0.0288	0.123	0.621
Turbine In Die	0.0073	1.0932	1.0032
Journal Bearing	0.0278	0.0425	0.4322
Inter Row Tap	0.0298	0.0635	0.6258
Journal Differential	0.0626	0.0299	0.5499

D.2.5 Derived Quantities

In analyzing the data output from the tests, many derived quantities are used. The errors for each measurement contained in a derived quantity propagate depending on the operation used. The derived error for an addition or subtraction is defined as

$$E_{Sum} = \sqrt{E_1^2 + E_2^2} \tag{D.8}$$

The error from the multiplication of two quantities is defined as

$$E_{Product} = \pm AB\sqrt{\left(\frac{E_A}{A}\right)^2 + \left(\frac{E_B}{B}\right)^2} \tag{D.9}$$

The error from the division of two quantities is defined as

$$E_{Quotient} = \frac{A}{B}\sqrt{\left(\frac{E_A}{A}\right)^2 + \left(\frac{E_B}{B}\right)^2} \tag{D.10}$$

The error caused by raising a value with an error associated to a power is given by

$$E_{Power} = nA^{n-1}E_A \tag{D.11}$$

These expressions are used to calculate the derived errors throughout Chapters 4 and 5 [1].

Appendix E

Packaging Details

This appendix contains the detailed design drawings for the packaging pieces.

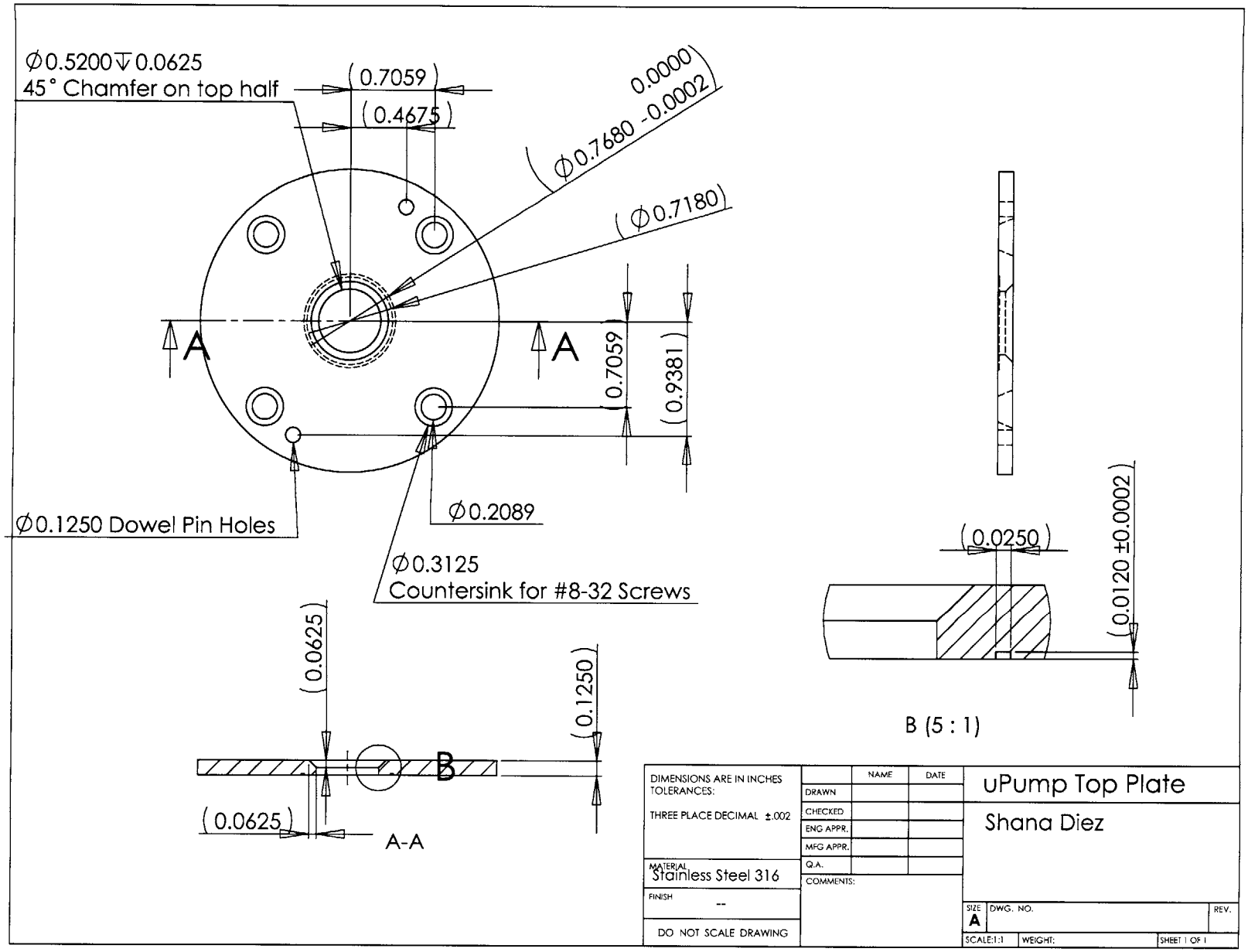
Ø0.5200↧0.0625
45° Chamfer on top half
(0.7059)
(0.4675)
(Ø0.7680 0.0000 -0.0002)
(Ø0.7180)
A
A
(0.7059)
(0.9381)
Ø0.1250 Dowel Pin Holes
Ø0.2089
Ø0.3125
Countersink for #8-32 Screws
(0.0625)
(0.1250)
B
(0.0625)
A-A
(0.0250)
(0.0120 ±0.0002)
B (5 : 1)
DIMENSIONS ARE IN INCHES
TOLERANCES:
THREE PLACE DECIMAL ±.002
MATERIAL Stainless Steel 316
FINISH --
DO NOT SCALE DRAWING
NAME
DATE
DRAWN
CHECKED
ENG APPR.
MFG APPR.
Q.A.
COMMENTS:
uPump Top Plate
Shana Diez
SIZE A
DWG. NO.
REV.
SCALE:1:1
WEIGHT:
SHEET 1 OF 1

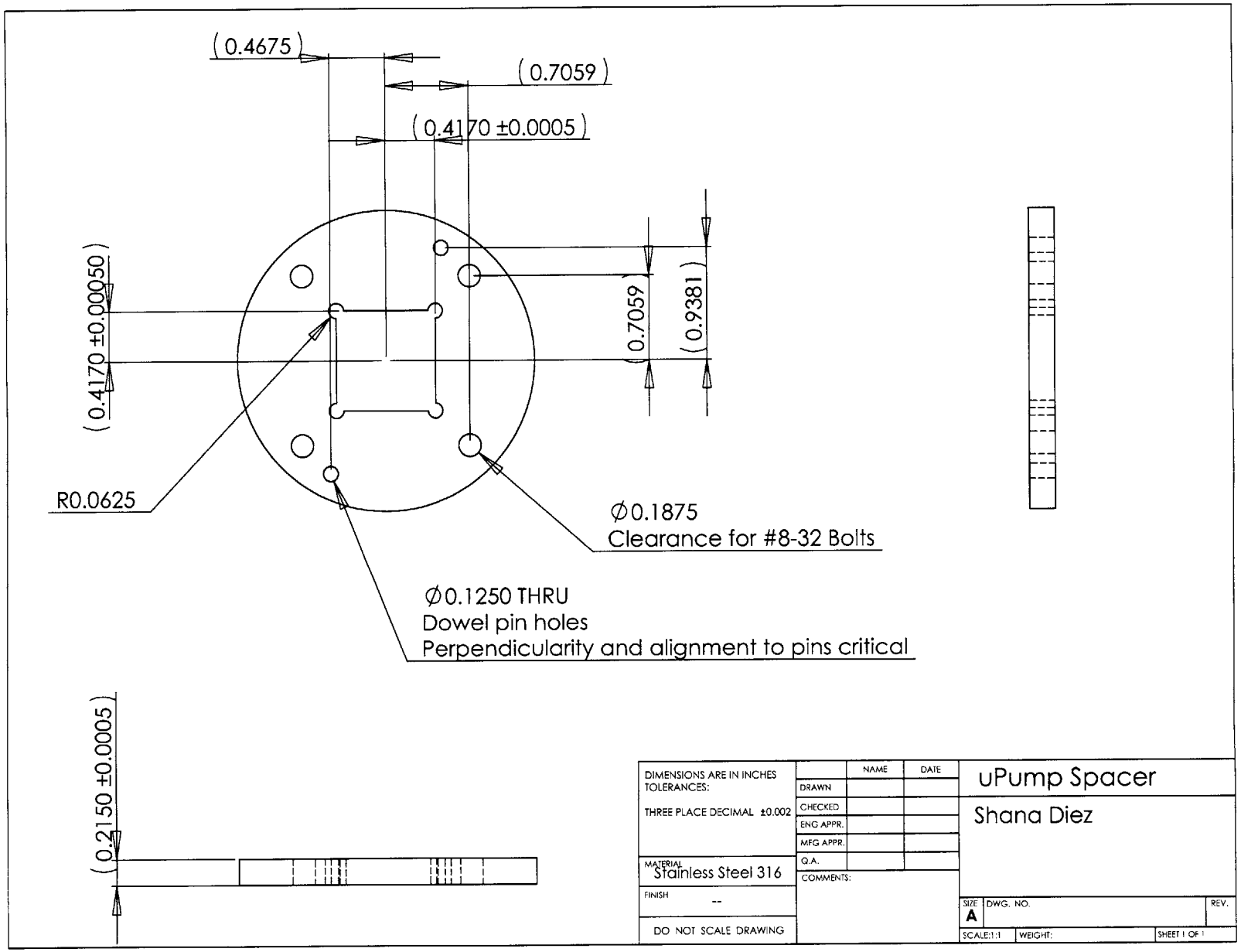
(0.4675)
(0.7059)
(0.4170 ±0.0005)
(0.4170 ±0.00050)
0.7059
(0.9381)
R0.0625
Ø0.1875
Clearance for #8-32 Bolts
Ø0.1250 THRU
Dowel pin holes
Perpendicularity and alignment to pins critical
(0.2150 ±0.0005)
DIMENSIONS ARE IN INCHES
TOLERANCES:
THREE PLACE DECIMAL ±0.002
MATERIAL
Stainless Steel 316
FINISH
--
DO NOT SCALE DRAWING
NAME
DATE
DRAWN
CHECKED
ENG APPR.
MFG APPR.
Q.A.
COMMENTS:
uPump Spacer
Shana Diez
SIZE
A
DWG. NO.
REV.
SCALE:1:1
WEIGHT:
SHEET 1 OF 1

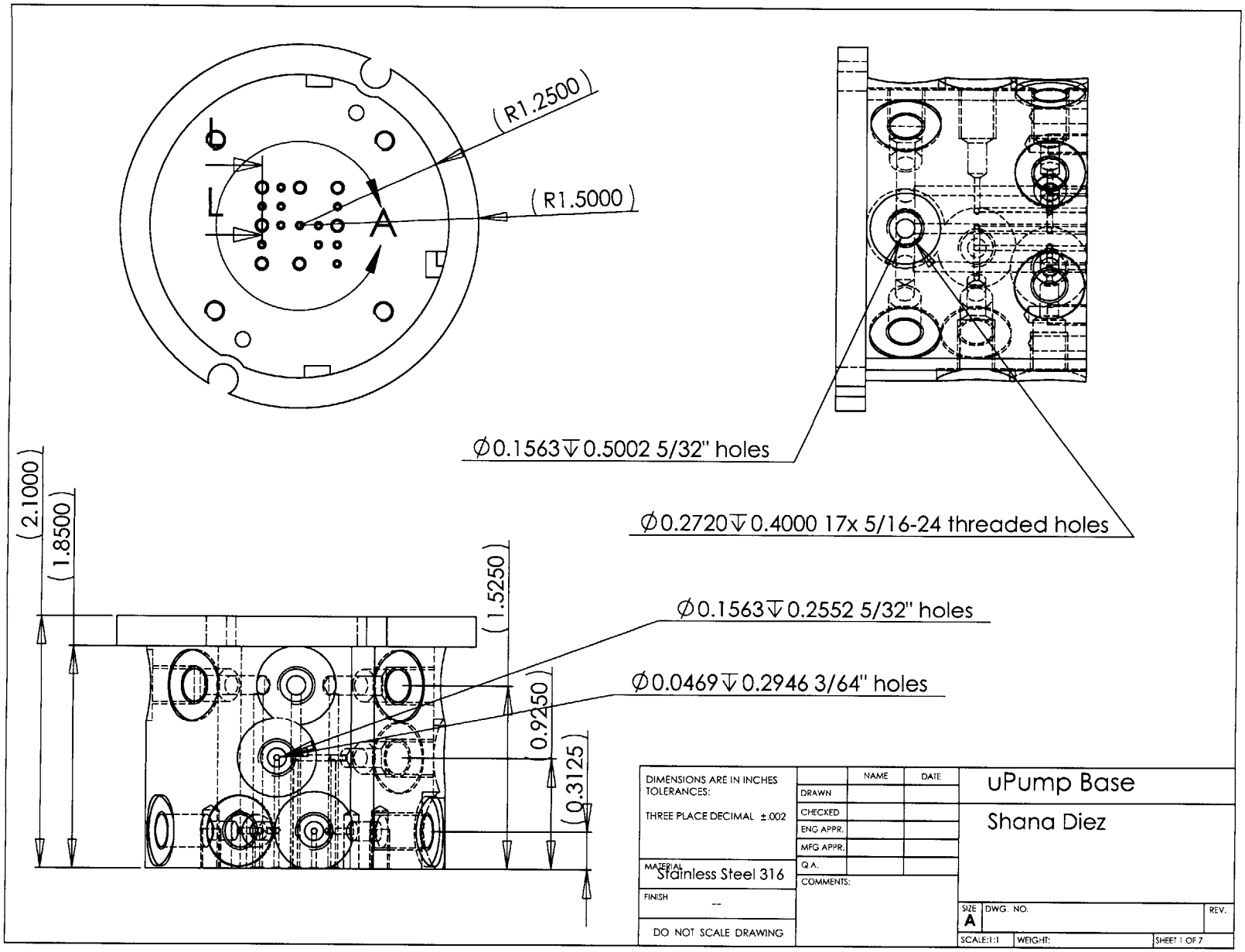

DIMENSIONS ARE IN INCHES TOLERANCES: THREE PLACE DECIMAL ±.002		NAME	DATE
	DRAWN		
	CHECKED		
	ENG APPR.		
	MFG APPR.		
	Q.A.		
MATERIAL Stainless Steel 316	COMMENTS:		
FINISH --			
DO NOT SCALE DRAWING			

uPump Base

Shana Diez

SIZE A	DWG. NO.	REV.
SCALE:1:1	WEIGHT:	SHEET 1 OF 7

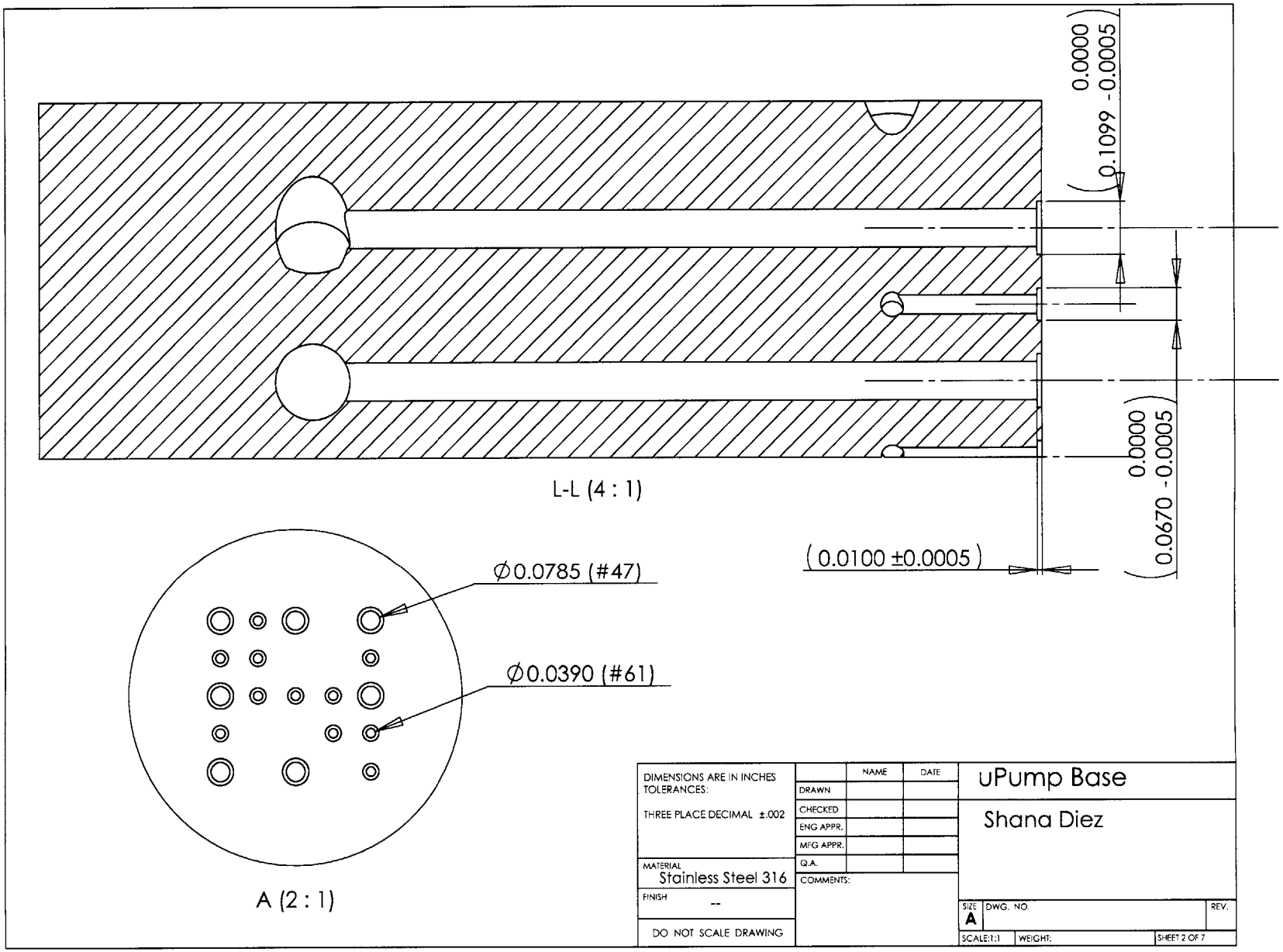
0.0000
0.1099 -0.0005
L-L (4 : 1)
0.0000
0.0670 -0.0005
(0.0100 ±0.0005)
Ø0.0785 (#47)
Ø0.0390 (#61)
A (2 : 1)
DIMENSIONS ARE IN INCHES
TOLERANCES:
THREE PLACE DECIMAL ±.002
MATERIAL
Stainless Steel 316
FINISH
--
DO NOT SCALE DRAWING
NAME
DATE
DRAWN
CHECKED
ENG APPR.
MFG APPR.
Q.A.
COMMENTS:
uPump Base
Shana Diez
SIZE
A
DWG. NO.
REV.
SCALE:1:1
WEIGHT:
SHEET 2 OF 7

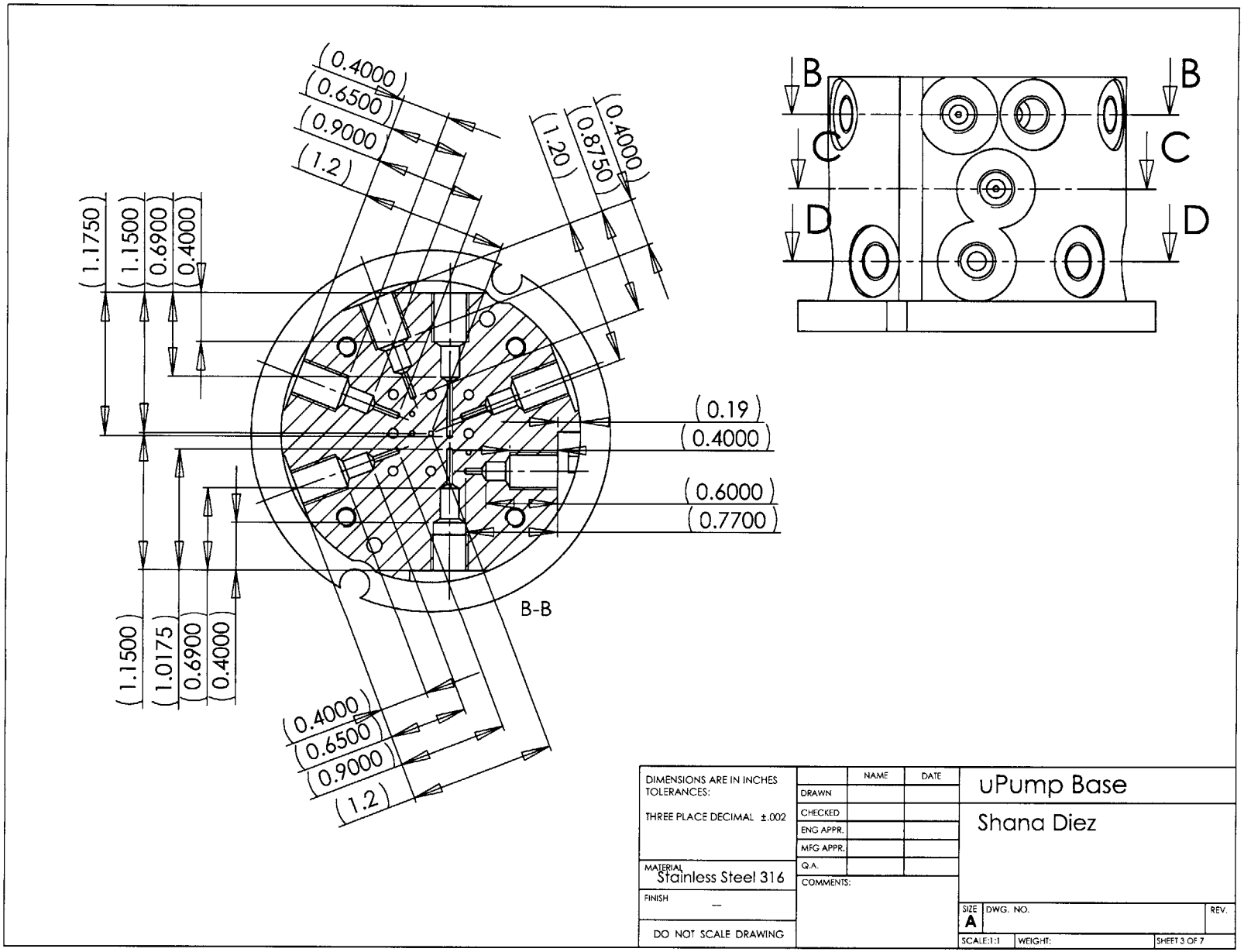

DIMENSIONS ARE IN INCHES TOLERANCES: THREE PLACE DECIMAL ±.002		NAME	DATE
	DRAWN		
	CHECKED		
	ENG APPR.		
	MFG APPR.		
	Q.A.		
	COMMENTS:		
MATERIAL Stainless Steel 316			
FINISH —			
DO NOT SCALE DRAWING			

uPump Base		
Shana Diez		
SIZE A	DWG. NO.	REV.
SCALE:1:1	WEIGHT:	SHEET 3 OF 7

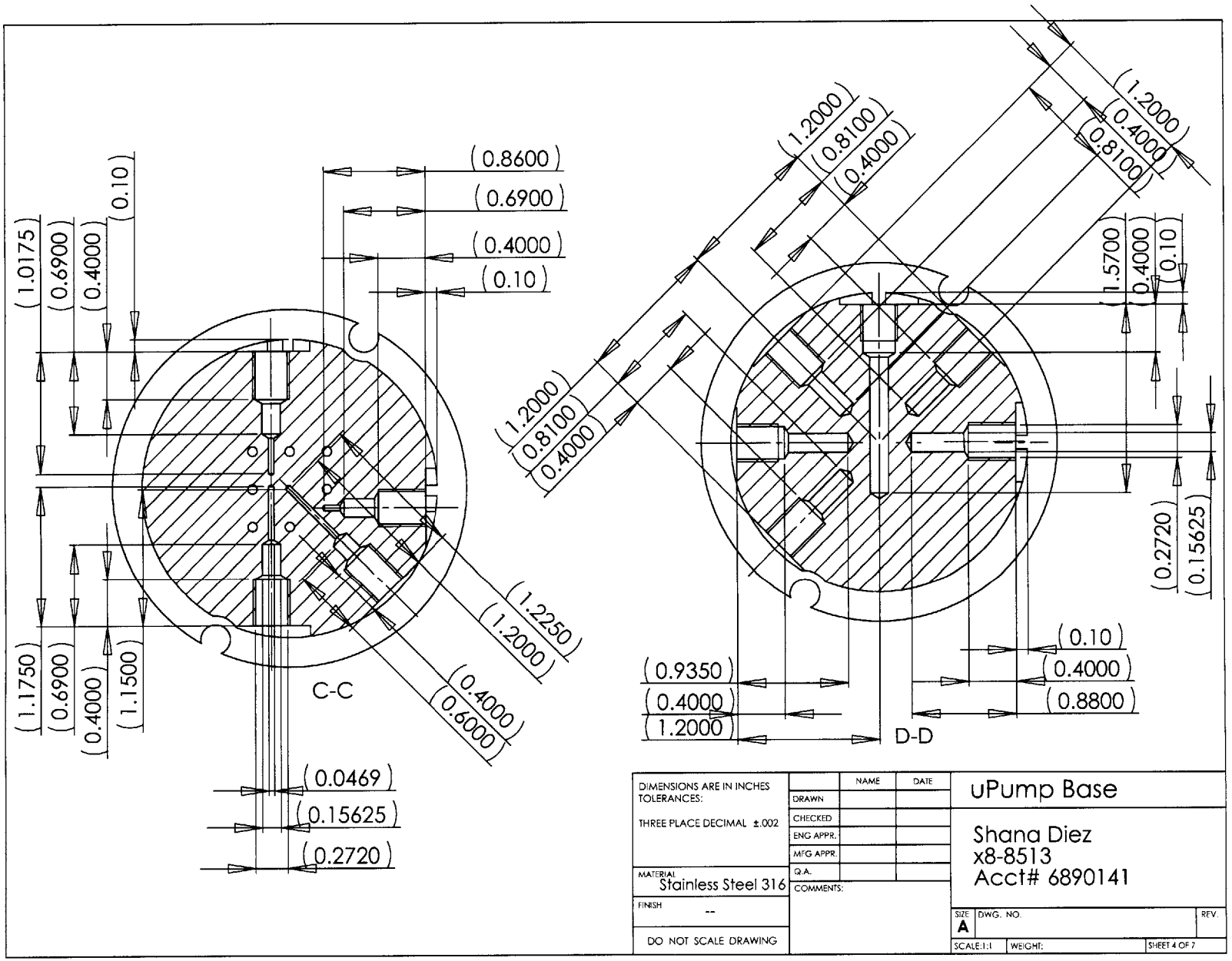
(0.8600)
(0.6900)
(0.4000)
(0.10)
(1.0175)
(0.6900)
(0.4000)
(0.10)
(1.2250)
(1.2000)
(0.4000)
(0.6000)
(1.1750)
(0.6900)
(0.4000)
(1.1500)
C-C
(0.0469)
(0.15625)
(0.2720)
(1.2000)
(0.8100)
(0.4000)
(1.2000)
(0.8100)
(0.4000)
(1.2000)
(0.4000)
(0.8100)
(1.5700)
(0.4000)
(0.10)
(0.2720)
(0.15625)
(0.9350)
(0.4000)
(1.2000)
D-D
(0.10)
(0.4000)
(0.8800)
DIMENSIONS ARE IN INCHES
TOLERANCES:
THREE PLACE DECIMAL ±.002
MATERIAL
Stainless Steel 316
FINISH
--
DO NOT SCALE DRAWING
NAME
DATE
DRAWN
CHECKED
ENG APPR.
MFG APPR.
Q.A.
COMMENTS:
uPump Base
Shana Diez
x8-8513
Acct# 6890141
SIZE
A
DWG. NO.
REV.
SCALE:1:1
WEIGHT:
SHEET 4 OF 7

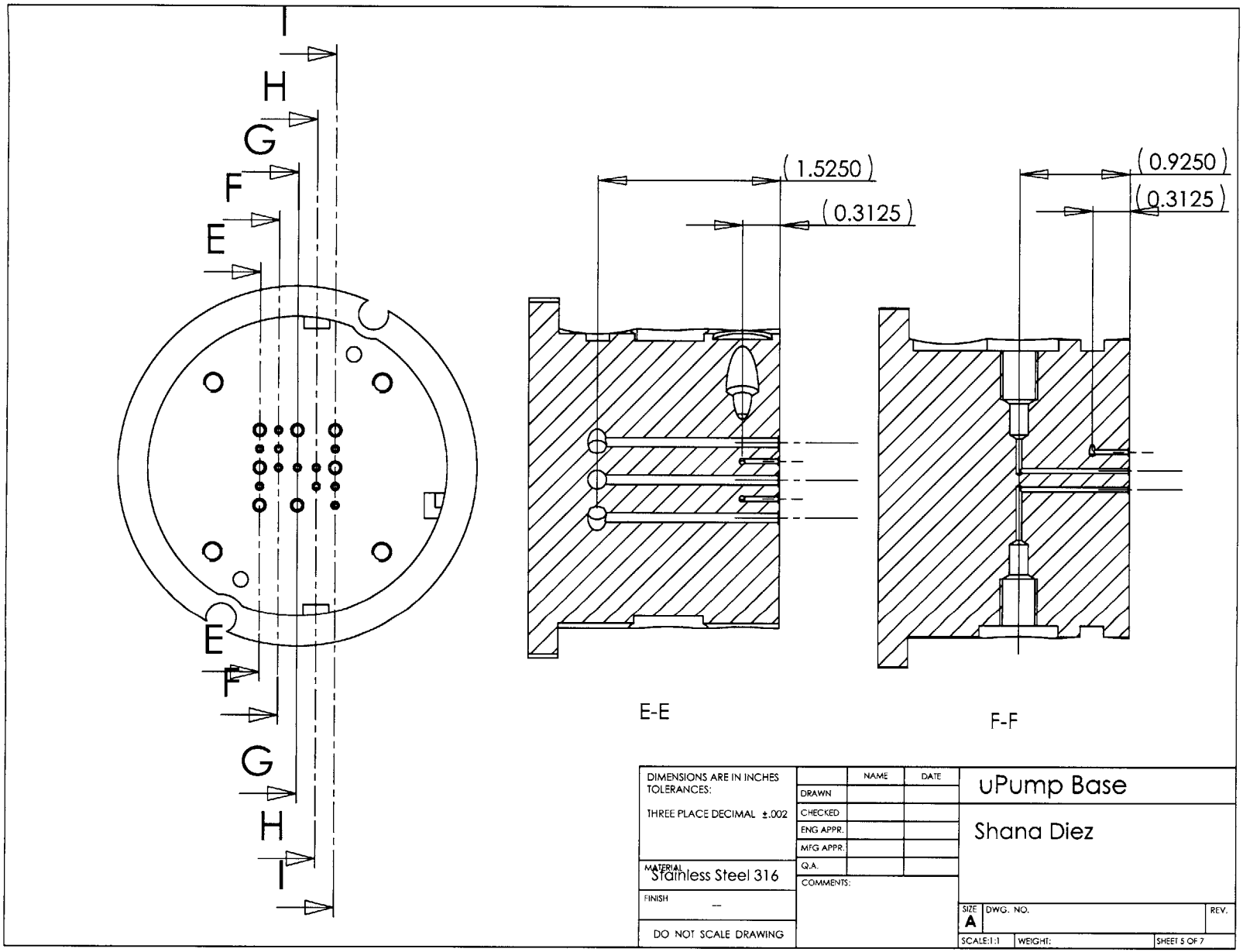

		NAME	DATE
DIMENSIONS ARE IN INCHES TOLERANCES: THREE PLACE DECIMAL ±.002	DRAWN		
	CHECKED		
	ENG APPR.		
	MFG APPR.		
	Q.A.		
MATERIAL Stainless Steel 316	COMMENTS:		
FINISH —			
DO NOT SCALE DRAWING			

uPump Base

Shana Diez

SIZE	DWG. NO.	REV.
A		
SCALE:1:1	WEIGHT:	SHEET 5 OF 7

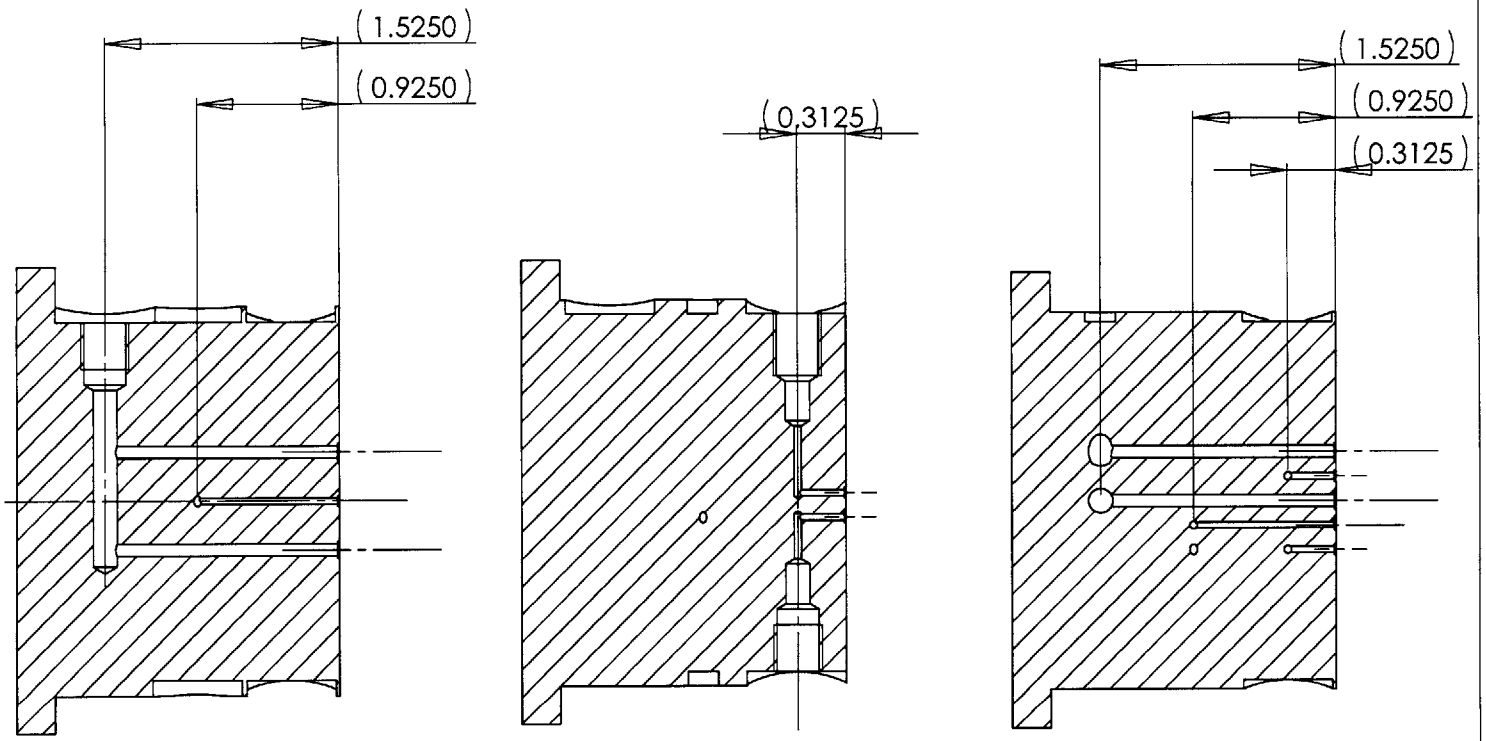

DIMENSIONS ARE IN INCHES TOLERANCES: THREE PLACE DECIMAL ±.002		NAME	DATE
	DRAWN		
	CHECKED		
	ENG APPR.		
	MFG APPR.		
	Q.A.		
	COMMENTS:		
MATERIAL Stainless Steel 316			
FINISH ---			
DO NOT SCALE DRAWING			

uPump Base		
Shana Diez		
SIZE A	DWG. NO.	REV.
SCALE:1:1	WEIGHT:	SHEET 6 OF 7

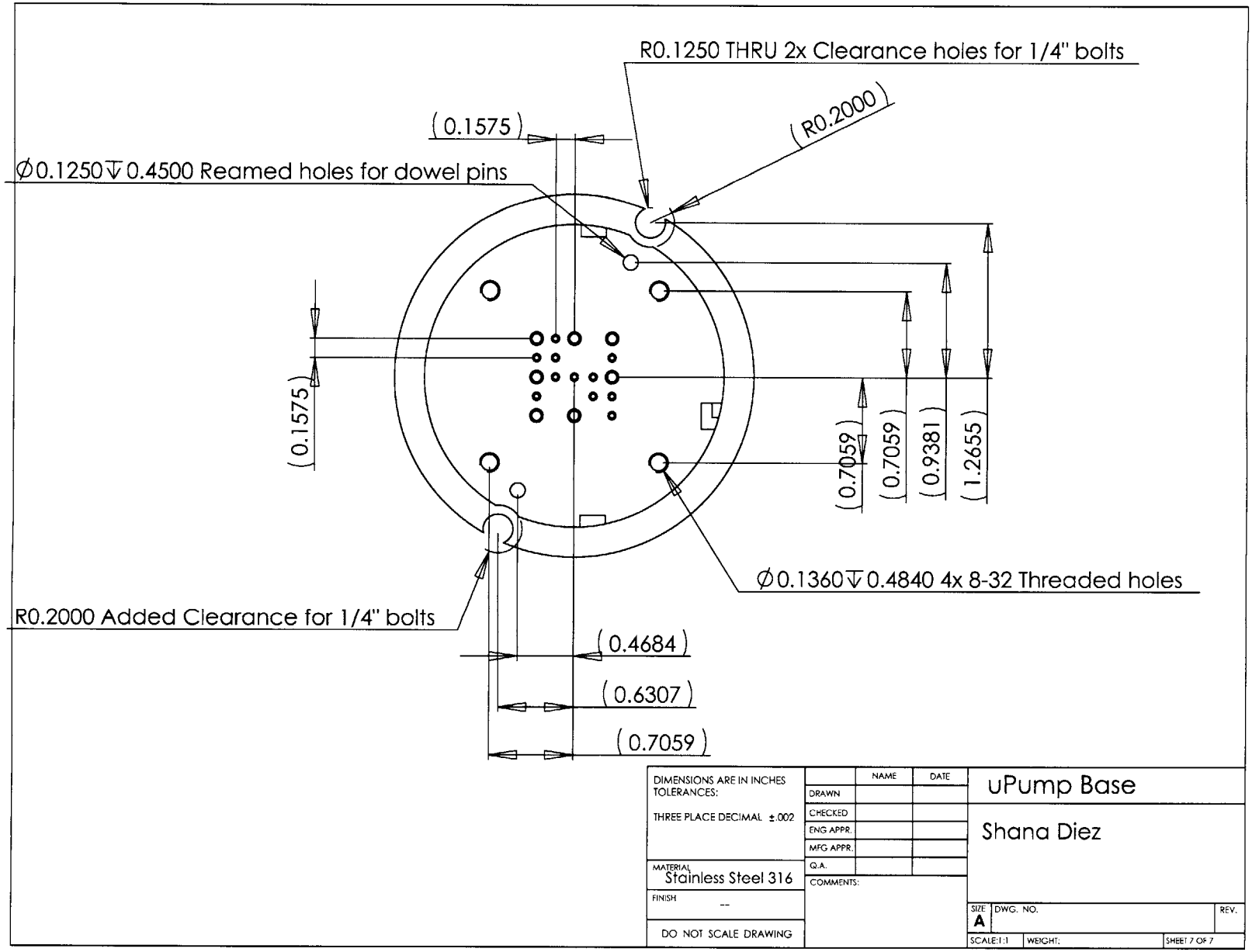
R0.1250 THRU 2x Clearance holes for 1/4" bolts
(0.1575)
(R0.2000)
Ø0.1250↧0.4500 Reamed holes for dowel pins
(0.1575)
(0.7059)
(0.7059)
(0.9381)
(1.2655)
Ø0.1360↧0.4840 4x 8-32 Threaded holes
R0.2000 Added Clearance for 1/4" bolts
(0.4684)
(0.6307)
(0.7059)
DIMENSIONS ARE IN INCHES
TOLERANCES:
THREE PLACE DECIMAL ±.002
MATERIAL
Stainless Steel 316
FINISH
--
DO NOT SCALE DRAWING
NAME
DATE
DRAWN
CHECKED
ENG APPR.
MFG APPR.
Q.A.
COMMENTS:
uPump Base
Shana Diez
SIZE
A
DWG. NO.
REV.
SCALE:1:1
WEIGHT:
SHEET 7 OF 7

Bibliography

[1] B. Austin Barry. *Errors in Practical Measurement in Science, Engineering, and Technology.* John Wiley and Sons, Inc., 1978.

[2] Antoine Deux. Design of a silicon microfabricated rocket engine turbopump. Master's thesis, Massachusetts Institute of Techonology, Department of Aeronautics and Astronautics, June 2001.

[3] Frederich Ehrich. Personal communication.

[4] A.H. Epstein, S.D. Senturia, O. Al-Midani, G. Anathasuresh, A Ayon, K. Breuer, K-S Chen, F. Ehrich, E. Esteve, L. Frechette, G. Gauba, R. Ghodssi, C. Groshenry, S. Jacobson, J. Kerrebrock, J. Lang, C-C Lin, A. London, J. Lopata, A. Mehra, J. Mur Miranda, S. Nagle, D.J. Orr, E. Piekos, M. Schmidt, G. Shirley, S. Spearing, C. Tan, Y-S. Tzeng, and I. Waitz. Micro-heat engines, gas turbines, and rocket engines - the mit microengine project. *presented at the 28th AIAA Fluid Dynamics Conference and the 4th AIAA Shear Flow Control Conference, Snowmass Village, CO No. 97-1773*, June 1997.

[5] Bernard J. Hamrock. *Fundamentals of fluid film lubrication.* fifth edition, McGraw-Hill Book Company, 1995.

[6] Stuart Jacobson. Personal communication.

[7] Laurent Jamonet. Testing of a microrocket engine turbopump. Master's thesis, Massachusetts Institute of Technology, Department of Aeronautics and Astronautics, 2002.

[8] Jack Kerrebrock. Personal communication.

[9] Jin Wook Lee. Personal communication.

[10] L. X. Liu, C. J. Teo, A. H. Epstein, and Z. S. Spakovszky. Hydrostatic gas journal bearings for micro-turbomachinery. *Proceedings of the ASME Design Engineering Technical Conferences and Computers and Information in Engineering Conference*, September 2003.

[11] Lixian Liu. Personal communication.

[12] Norihisa Miki. Personal communication.

[13] Sumita Pennathur. Micro-scale turbopump blade cavitation. Master's thesis, Massachusetts Institute of Techonology, Department of Aeronautics and Astronautics, June 2001.

[14] Christopher Protz. Systems analysis of a microfabricated storable bipropellant rocket engine. Master's thesis, Massachusetts Institute of Techonology, Department of Aeronautics and Astronautics, January 2000.

[15] Z. S. Spakovszky and L. X. Liu. Scaling laws for ultra-short hydrostatic gas journal bearings. *Proceedings of the ASME Design Engineering Technical Conferences and Computers and Information in Engineering Conference*, September 2003.

[16] Chiang Juay Teo. Personal communication.

[17] Harold Youngren. Personal communication.

S993-12